

ABSTRACT

Title of Document:

**TARGETING INTERCELLULAR
ADHESION MOLECULE-1 TO
ENHANCE DELIVERY OF
THERAPEUTIC ENZYMES FOR
TREATMENT OF LYSOSOMAL
STORAGE DISEASES**

Janet Hsu, Doctor of Philosophy, 2014

Directed By:

Associate Professor Silvia Muro,
Fischell Department of Bioengineering &
Institute for Bioscience and Biotechnology
Research

Lysosomal storage diseases (LSDs) are a group of more than 40 genetically inherited diseases that result from dysfunction of specific proteins, often an enzyme, located in lysosomes within cells which leads to abnormal lysosomal accumulation of specific macromolecules. As a result, cell malfunction occurs and escalates into multi-tissue and multi-organ failures, often resulting in premature death. For several early onset LSDs, the central nervous system (CNS) is also affected and manifests fatal neuropathic and/or neurodegenerative symptoms. Within the last two decades, treatment for selective LSDs has become clinically available. Specifically, enzyme replacement therapy (ERT) by intravenous injection of recombinant enzymes holds relevant promise. Yet current ERT results in suboptimal enzyme biodistribution to

many target organs, including the peripheral organs and also the CNS. Delivery to the CNS is particularly impeded due to the tight blood-brain barrier (BBB) that strictly regulates passage between the circulation system and the brain tissue. We explored the use of targeted drug delivery systems to address this issue. Specifically, we focused on targeting intercellular adhesion molecule-1 (ICAM-1), a cell surface glycoprotein that is upregulated under pathological conditions, including LSDs. In this dissertation, using *in vitro*, cell culture, and *in vivo* techniques, we examined whether ICAM-1-targeted polymer nanocarriers: (1) enhance binding, uptake, and lysosomal delivery of different enzymes in cells, (2) provide targeting and transport across endothelial and subendothelial cells of the BBB, and (3) improve accumulation of lysosomal enzymes to peripheral organs and the brain. Results suggest that after intravenous injection of enzyme coupled to ICAM-1-targeted nanocarriers, ICAM-1 targeting shift these enzymes from the circulation to tissues, enhancing enzyme accumulation over non-targeted counterparts both in peripheral organs and the brain. This could be modulated by varying parameters such as the density of targeting antibodies on the carrier coat or the carrier bulk concentration. Also, ICAM-1-targeted nanocarriers were transported across BBB models followed by uptake and lysosomal transport to neuron-like cells. ICAM-1-targeted nanocarriers preferentially bound to diseased cells and were internalized and trafficked to lysosomes, resulting in degradation of the accumulated substrate. Therefore, overall, ICAM-1-targeting shows promise in improving ERT for LSD treatment.

TARGETING INTERCELLULAR ADHESION MOLECULE-1 TO ENHANCE
DELIVERY OF THERAPEUTIC ENZYMES FOR TREATMENT OF
LYSOSOMAL STORAGE DISEASES

By

Janet Hsu

Dissertation submitted to the Faculty of the Graduate School of the
University of Maryland, College Park, in partial fulfillment
of the requirements for the degree of
Doctor of Philosophy
2014

Advisory Committee:

Professor Silvia Muro, Fischell Department of Bioengineering & Institute for Biosciences
and Biotechnology Research, University of Maryland, Chair
Professor Srinivasa Raghavan, Department of Chemical and Biomolecular Engineering,
University of Maryland, Dean's Representative
Professor William Bentley, Fischell Department of Bioengineering, University of
Maryland
Professor John Fisher, Fischell Department of Bioengineering, University of Maryland
Professor Steven Jay, Fischell Department of Bioengineering, University of Maryland
Professor Gustavo Maegawa, Department of Pediatrics, Johns Hopkins University School
of Medicine

© Copyright by
Janet Hsu
2014

Dedication

This thesis is dedicated to my dear grandfather, Yu Chi Ren

Acknowledgments

First, I would like to acknowledge my advisor, Dr. Silvia Muro. If it wasn't for her support, enthusiasm, and guidance, I would not have accomplished what I had during my time here at the University of Maryland. Thank you for your trust, advice, and encouragement, I have learned so much.

I would also like to thank all members of the Muro Lab, past and present, for their support, patience, and love: the postdocs, Dr. Carmen Garnacho, Dr. Tridib Bhowmick, Dr. Viraj Mane; the graduate students, Daniel Serrano, Dr. Iason Papademetriou, Rasa Ghaffarian, Rachel Manthe, Zois Tsinas; the undergraduate students, Maria Ansar, Jeff Rapaport (ex-minion). All your hard work, published or not, successful or not, does not go un-noticed. Thank you for all that you have taught me, and all the memories and experiences you have shared with me. I will never forget our time together inside and out of the Muro Lab in Plant Sciences Building (and all the candy, ice cream, farmer's market, and food runs in the name of sanity ;)).

To my friends in the Virginia, DC, and Maryland area, thank you. Special thanks to my UMD colleagues (incoming BIOE class of 2008: Dr. Jordan Betz, Dr. Eric Hoppmann, Dr. Laura Heinzke Hyland, Charles Yuan-Chia Kuo, Michael Lai, Dr. Carlos Luna, Dr. Kate Malinowski, Dr. Iason Papademetriou, Dr. Julianne Twomey, Rodica Tuduce, Dr. VeeMoon Yu; others: Adam Brown, Dr. Karen Carter, Dr. Justin Szu-Ting Chou, Dr. Amanda Rhode Galante, Dr. Alek Nacev, Dr. Chen-Yu Tsao,

Chelsea Virgile, Mark Liang-Jun Wang, Dr. Alvin Yew, Amin Zargar). You are all wonderful, thank you for everything. Cheers to good memories (especially at Varsity Grill, Thirsty Turtle, Town Hall, and Looney's, and of course "fat days" ;))! Especially Carlos and Veemoon, for being great partners in crime, foodies, and solid, great friends that I can trust to be there for me when I need them most. And, of course, Karen, thank you for checking in and for all the surprise jelly bellies, coloring templates, etc. Special thanks to Dr. Terry Yen and Tam Dang, for keeping me sane and keeping the kid spirit in me. You all have made my move to the "other" coast so much easier and fun than I could have imagined. I love you and will miss you all so much! And of course, my love, Dr. Jason Liu, thank you thank you thank you would not be enough to express the gratitude for all your patience, support, humor, and unwavering love, and not to mention food delivery, I'm such a lucky gal.

Of course, thanks to those on the other coast, in California, the girls who would never let me forget them and I would never forget, Erica, Edith, Jennifer, Jessica, Pamela, and Tammy. Thanks for the visits, calls, texts. And thank you to my ever-wandering best bud, Grant, thanks for all the reality checks and good laughs. I love you all, and I definitely could not do this without you all rooting for me.

Lastly, but not the least, I'd like to thank my dear family: Dad, Mom, Dr. Emily, Grace, Warren, John, and Lydia. Without you all, I would not be the person I am today and would not have been able to achieve what I had so far from my comfort zone. Thank you all for your love and support.

Table of Contents

DEDICATION.....	II
ACKNOWLEDGMENTS	III
TABLE OF CONTENTS	V
LIST OF ABBREVIATIONS	VIII
SECTION 1: INTRODUCTION AND OVERVIEW	1
1.1. PROBLEM DESCRIPTION AND MOTIVATION.....	1
1.2. OUR APPROACH	2
1.3. SIGNIFICANCE AND NOVELTY	5
SECTION 2: BACKGROUND	8
2.1. LYSOSOMAL STORAGE DISORDERS	8
2.2. TREATMENTS FOR LSDS AND THEIR CHALLENGES	10
2.3. ENZYME REPLACEMENT THERAPY FOR LSDS	14
2.4. DRUG DELIVERY SYSTEMS FOR TREATMENT OF LSDS	16
2.5. TARGETING STRATEGIES FOR TREATMENT OF LSDS.....	19
2.6. ENDOCYTOSIS AND SUBCELLULAR TRANSPORT OF DRUG DELIVERY SYSTEMS FOR LSD TREATMENT	22
2.7. ICAM-1-TARGETING STRATEGIES FOR LSD APPLICATIONS	25
SECTION 3: METHODS.....	29
3.1. ANTIBODIES AND REAGENTS	29
3.2. IODINATION OF PROTEINS	29
3.3. NANOCARRIER PREPARATION AND CHARACTERIZATION	30
3.4. CELL CULTURE.....	32
3.5. ICAM-1 EXPRESSION.....	34
3.6. BINDING OF ICAM-1-TARGETED NANOCARRIERS TO CELLS.....	34
3.7. ENDOCYTOSIS OF ICAM-1-TARGETED NANOCARRIERS INTO CELLS	35
3.8. LYSOSOMAL TRAFFICKING OF ICAM-1-TARGETED NANOCARRIERS IN CELLS	36
3.9. CELL CULTURE MODELS OF THE BLOOD-BRAIN BARRIER.....	37
3.10. TRANSCYTOSIS OF ICAM-1-TARGETED CARRIERS ACROSS BBB CELL MODELS	38

3.11. CELL CULTURE MODELS FOR DISEASE	39
3.12. SUBSTRATE DEGRADATION BY ICAM-1-TARGETED CARRIERS IN CELLS	40
3.13. VISUALIZATION OF ICAM-1-TARGETED CARRIERS IN MICE	41
3.14. IN VIVO CIRCULATION AND BIODISTRIBUTION OF ICAM-1-TARGETED CARRIERS IN MICE.....	42
3.15. IN VIVO DISTRIBUTION OF ICAM-1-TARGETED CARRIERS IN MOUSE BRAIN.....	43
3.16. STATISTICS.....	43
SECTION 4: RESULTS AND DISCUSSION.....	44
4.1. LYSOSOMAL ENZYME DELIVERY TO CELLS BY ICAM-1-TARGETED NANOCARRIERS	44
4.1.1. <i>Introduction</i>	44
4.1.2. <i>Coating of enzyme onto ICAM-1-targeted nanocarriers</i>	45
4.1.3. <i>Enzyme release from ICAM-1-targeted nanocarriers</i>	47
4.1.4. <i>Binding of anti-ICAM/enzyme nanocarriers to cells</i>	50
4.1.5. <i>Endocytosis of anti-ICAM/enzyme nanocarriers by cells</i>	54
4.1.6. <i>Mechanism of endocytosis of anti-ICAM/enzyme nanocarriers</i>	56
4.1.7. <i>Lysosomal trafficking of anti-ICAM/enzyme nanocarriers</i>	58
4.1.8. <i>Alleviation of excess lysosomal storage by anti-ICAM/enzyme nanocarriers</i>	60
4.1.9. <i>Conclusion</i>	62
4.2. TARGETING OF CELLS OF THE BLOOD-BRAIN BARRIER AND THE BRAIN BY ICAM- 1-TARGETED NANOCARRIERS.....	64
4.2.1. <i>Introduction</i>	64
4.2.2. <i>Expression of ICAM-1 on cells of the blood-brain barrier</i>	65
4.2.3. <i>Binding of ICAM-1-targeted nanocarriers to cells of the blood-brain barrier</i>	67
4.2.4. <i>Internalization of ICAM-1-targeted nanocarriers by cells of the blood-brain barrier</i>	70
4.2.5. <i>Mechanism of endocytosis of ICAM-1-targeted nanocarriers into cells of the blood-brain barrier</i>	72
4.2.6. <i>Lysosomal trafficking of ICAM-1-targeted nanocarriers in cells of the blood- brain barrier</i>	75
4.2.7. <i>Binding and transport of ICAM-1-targeted nanocarriers across blood-brain barrier endothelial monolayers</i>	77
4.2.8. <i>Mechanism of transport of ICAM-1-targeted nanocarriers across blood-brain barrier endothelial monolayers</i>	80
4.2.9. <i>Transport of ICAM-1-targeted nanocarriers across blood-brain barrier endothelial-subendothelial bi-layers</i>	81
4.2.10. <i>ICAM-1 expression on neuroblastoma derived neuron-like cells</i>	83
4.2.11. <i>Binding of ICAM-1-targeted nanocarriers to neuron-like cells</i>	85
4.2.12. <i>Endocytosis of ICAM-1-targeted nanocarriers into neuron-like cells</i>	88
4.2.13. <i>Mechanism of endocytosis of ICAM-1-targeted nanocarriers in neuron-like cells</i>	91
4.2.14. <i>Lysosomal trafficking of ICAM-1-targeted nanocarriers in neuron-like cells</i>	93
4.2.15. <i>Conclusion</i>	95

4.3. ENHANCED DELIVERY OF LYSOSOMAL ENZYME TO ORGANS IN MICE BY ICAM-1-TARGETING.....	97
4.3.1. <i>Introduction</i>	97
4.3.2. <i>Circulation of anti-ICAM/enzyme nanocarriers versus non-targeted enzyme in mice</i>	98
4.3.3. <i>Blood versus tissue distribution of anti-ICAM/enzyme nanocarriers in mice</i>	100
4.3.4. <i>Visualization of anti-ICAM nanocarriers in mice</i>	101
4.3.5. <i>Biodistribution pattern and specificity of anti-ICAM/enzyme nanocarriers in mice</i>	103
4.3.6. <i>Brain targeting of anti-ICAM/enzyme nanocarriers in mice</i>	108
4.3.7. <i>Visualization of anti-ICAM/enzyme nanocarriers in the brain of mice</i>	110
4.3.8. <i>Tissue retention of anti-ICAM/enzyme nanocarriers in mice tissue</i>	111
4.3.9. <i>Conclusion</i>	113
4.4. ENHANCEMENT OF ENZYME DELIVERY BY MODULATION OF ICAM-1-TARGETED NANOCARRIERS	115
4.4.1. <i>Introduction</i>	115
4.4.2. <i>Visualization of dose-dependent targeting of anti-ICAM nanocarriers in mice</i> .	116
4.4.3. <i>Comparative tissue versus blood re-distribution of anti-ICAM/enzyme nanocarriers</i>	116
4.4.4. <i>Effects of varying targeting surface-density or nanocarrier bulk-concentration on enzyme distribution in vivo</i>	120
4.4.5. <i>Specificity and absolute enzyme delivery by anti-ICAM nanocarriers</i>	123
4.4.6. <i>Conclusion</i>	127
SECTION 5. OVERALL CONCLUSIONS	128
5.1. SUMMARY	128
5.2. FUTURE DIRECTIONS.....	131
REFERENCES.....	136
PUBLICATIONS	150

List of Abbreviations

%ID	Percentage of injected dose
%ID/g	Percentage of injected dose per gram of tissue
α Gal	α -galactosidase
¹²⁵ I	125-Iodine
AC	Astrocyte
ANOVA	Analysis of variance
Anti-ICAM	Antibody targeted to intercellular adhesion molecule-1
ASM	Acid sphingomyelinase
BBB	Blood-brain barrier
BMT	Bone marrow transplant
BSA	Bovine serum albumin
CAM	Cell adhesion molecule
CNS	Central nervous system
EC	Endothelial cell
EIPA	5-(N-ethyl-N-isopropyl)amiloride
EET	Enzyme enhancement therapy
ERT	Enzyme replacement therapy
FD	Fabry disease
GAA	α -glucosidase
Gb3	Globotriaosylceramide
HBMEC	Human brain microvascular endothelial cell
HUVEC	Human umbilical vein endothelial cell
ICAM-1	Intercellular adhesion molecule-1
IgG	Immunoglobulin G
InsR	Insulin receptor
i.v.	Intravenous(ly)
LDL	low density lipoprotein
LR	Localization ratio
LSD	Lysosomal storage disease
M6P	Mannose-6-phosphate
M6PR	Mannose-6-phosphate receptor

MDC	Monodansylcadaverine
NBC	Neuroblastoma cell (non-differentiated)
NC	Nanocarrier
NLC	Neuron-like cell (differentiated NBC)
NPD	Niemann-Pick Disease
PAS	Periodic acid-Schiff
PBS	Phosphate-buffered saline
PC	Pericyte
PCT	Pharmacological chaperone therapy
PD	Pompe disease
PEG	Poly(ethylene glycol)
PLGA	Poly(lactide-co-glycolic acid)
RAP	Receptor-associated protein
RES	Reticuloendothelial system
SI	Specificity index
SMPD1	Sphingomyelin phosphodiesterase 1 (gene)
TCA	Trichloroacetic acid
TfR	Transferrin receptor

Section 1: Introduction and Overview

1.1. Problem Description and Motivation

Lysosomal storage disorders (LSDs) are a group of more than 40 inherited genetic diseases that affect as frequent as 1 in 2000 live births [1-9]. Each LSD is caused by a defect or deficiency of a particular functional lysosomal-associated protein, often a lysosomal enzyme, which leads to accrual of excess substrate in the lysosomes within cells, eventually results in cell death, tissue malfunction, and multi-organ failures, including both peripheral organs and the nervous system [1-8].

Currently there are only a few treatment options clinically available for LSDs [4, 10]. The most popular and among the most effective treatments is enzyme replacement therapy (ERT), in which a recombinant enzyme is intravenously (i.v.) injected into the patient in order to replace the missing activity, which requires the enzyme to bind, internalize and be trafficked to lysosomes within cells [4, 10]. This is possible because recombinant lysosomal enzymes have mannose-6-phosphate (M6P) residues that target the corresponding cell receptors, M6P receptor (M6PR), and lead to cell uptake with lysosomal trafficking [11, 12]. This costs an average of \$300,000 annually per patient [13-15]. However, ERT is still suboptimal since the majority of the injected enzyme accumulates in clearance organs (which are also disease targets) but not to other target tissues, such as the lungs, heart, muscle, etc. [4, 10].

Unfortunately, in addition to peripheral organ failures, often the central nervous system (CNS) is also affected in LSDs [16]. Drug delivery to the brain to treat the CNS is notoriously difficult due to the highly regulating blood-brain barrier (BBB). The BBB is composed of a tight monolayer of endothelial cells (the endothelial layer) in direct contact

with the blood circulation [17, 18]. Unlike vascular endothelial cells that line capillaries in some peripheral organs, the brain endothelium lacks fenestrations and has extremely tight cell-cell junctions [17, 18]. Additionally, the endothelial lining of the BBB is juxtaposed with subendothelial cells (the subendothelial layer) made up of mainly pericytes and astrocytes [19].

To treat brain symptoms in LSDs, several physicians have resorted to direct brain injections of the therapeutic or bone marrow transplant (BMT) [4, 8, 20]. Direct injection of bone marrow mesenchymal stem cells to the brain can stimulate growth of healthy neural networks [20, 21]. Unfortunately, aside from other side effects that may potentially occur with this method, such as graft versus host disease, direct brain injections (e.g. intracerebellar, intracerebroventricular, intraparenchymal, intrathecal, etc.) are rather invasive and carry risks of severe complications [4, 8, 21, 22]. Moreover, although this method can deliver treatment to the brain, the treatment does not reach peripheral organs that are also affected by LSDs. Therefore, LSD treatment options that include systemic delivery of lysosomal enzymes to both peripherally affected organs and the brain are still needed. A method to enhance targeting of ERT to all peripheral and CNS tissue, allowing uptake by cells and lysosomal transport throughout the body, may improve treatment efficacy and perhaps decrease the cost.

1.2. Our Approach

Targeted drug delivery systems have paved a path in the field to enhance the efficacy of several treatments [23-25]. Scientists have targeted cell markers, receptors, enzymes, etc. to guide delivery of drugs to affected cells [23-26]. Researchers have also looked to nature for clues for internalization, such as how viruses enter cells, how white blood cells are recruited

to sites of disease, or how lysosomal proteins are trafficked to lysosomes. Previous targeted drug delivery approaches to enhance distribution of therapeutic enzymes for LSDs have involved conjugation of recombinant enzymes to peptides, proteins, or antibody derivatives that target the insulin receptor (InsR), mannose-6-phosphate receptors (M6PR), receptor-associated protein (RAP), etc. receptors which are known to be associated to clathrin-coated pits, the pathway that is inherently used by endogenous lysosomal enzymes [11, 12, 24]. However, research has shown signs of impaired endocytosis by clathrin pathways in some LSDs [27-29]. To circumvent this, other strategies have focused on development of enzymes targeted by protein transduction domain peptides, which often render delivery inside the cell [30-33]. Nonetheless, although these strategies may enhance uptake into cells they still fail to improve passage from blood to tissue, particularly to the CNS [4, 8, 10, 34, 35].

In this dissertation, we focus on a strategy to target enzyme-loaded nanoparticles to intercellular adhesion molecule-1 (ICAM-1), a cell surface glycoprotein involved in adhesion and extravasation of leukocytes during inflammation [36-38]. ICAM-1 is expressed on most cell types and is upregulated under many pathologies, including LSDs [38, 39]. Hence, utilizing a drug delivery system with an affinity moiety specifically targeted to ICAM-1 can potentially enhance enzyme delivery to cells affected by LSDs. Due to the nature of LSDs, where the disease affects most cells and tissues, requiring systemic treatment, ICAM-1-targeted drug delivery systems could broadly enhance delivery of enzymes in the body. Additionally, previous work in our lab has shown that coating a nanoparticle with antibodies targeting ICAM-1 instigates a multivalent engagement of ICAM-1, which induces endocytosis of the nanoparticle through a non-classical route [40]. Therefore, this strategy holds potential to bypass disrupted clathrin-mediated endocytosis found in some LSDs [27-29]. Indeed, our lab has shown that ICAM-1-targeted nanocarriers enhance delivery of acid sphingomyelinase (ASM) to all peripheral organs in mice for treatment of type A and B

Niemann-Pick Disease (NPD) [41], along with enhanced degradation of the lysosomal substrate [42]. Whether this is applicable to other LSDs and whether the brain can also be targeted by this strategy remained to be tested.

In view of this, the global hypothesis for this dissertation is that ICAM-1-targeted nanocarriers can: a) generally enhance accumulation of lysosomal enzymes throughout the body, b) facilitate transport across the endothelial and subendothelial layer of the blood-brain barrier, and c) enable preferential binding to diseased cells with internalization, trafficking to lysosomes, and degradation of the accumulated substrate.

Investigation of the potential of ICAM-1-targeted nanocarriers for LSD treatment is assessed in cell culture and in vivo in mice. Cell culture systems enable studies to elicit distinct binding and resultant internalization, intracellular trafficking, and potential transport characteristics to selective cells and cell layers in a controlled environment. In vivo studies in mice, on the other hand, can then determine circulation time and accumulation at organ level, illustrating distribution patterns in a physiological system subjected to complex biological constraints (e.g. blood flow shear stress, presence of cell barriers, clearance from circulation, etc.) that are not present in an isolated cell culture models. Hence, both types of systems must be used to accurately learn the characteristics and potential efficacy of ICAM-1-targeted drug delivery system to deliver enzymes for LSD treatment.

The next section (Section 2) will provide background information on the several issues that ICAM-1-targeted nanocarriers aim to address. This includes LSD treatment options as well as current nanotechnology-based strategies and targeting approaches exploited to improve various disease treatments. The methods used to perform the work illustrated in this dissertation are described in Section 3, followed by the experimental results

and discussion in Section 4, and, finally, the overall conclusions of this work and potential future directions (Section 5).

1.3. Significance and Novelty

Previous work with ICAM-1-targeted delivery of ASM to NPD cellular and animal models showed promise [41, 42]. Additionally, ICAM-1-targeted platform has shown to be capable of transcellular transport across cell barriers, such as gastro-intestinal epithelial cells in culture [43]. Moreover, ICAM-1-targeting nanoparticle formulation and dose can be modified to modulate biodistribution pattern [44]. All in all, these studies suggest the potential for ICAM-1-targeted nanoparticles to improve enzyme delivery for LSD treatment. However, prior to the work described in this dissertation, whether enhanced lysosomal enzyme delivery by targeting ICAM-1 was unique to ASM or can be translated to improve delivery of other lysosomal enzymes had not been investigated; whether ICAM-1-targeting nanocarriers can traverse across other cell barriers such as that of the BBB remained unanswered; lastly, whether ICAM-1-targeted nanocarrier formulation with an enzyme load can be optimized without decreasing targeting specificity had also not been evaluated. Hence, this thesis aims to answer these questions.

The significance of the work presented in this thesis is the expanded knowledge on utilizing and modulating ICAM-1-targeting nanocarriers to enhance enzyme delivery for two other LSD treatments. Specifically, we studied delivery of α -galactosidase (α Gal) for treatment of Fabry disease (FD) [45] and α -glucosidase (GAA) for treatment of Pompe disease (PD) [46], expanding the application of ICAM-1-targeted delivery from previously studied ASM delivery for NPD [41, 42]. This was done by studying binding specificity to

cells (e.g. healthy versus diseased cells), internalization into cells, mechanism of internalization, lysosomal trafficking, and lysosomal substrate alleviation in disease cell models achieved by enzyme delivered by ICAM-1-targeted nanocarriers in cell culture (Section 4.1.). This is the first time the expansion of ICAM-1-targeting application has been thoroughly studied and compared amongst three different LSDs. Additionally, NPD and several other LSDs bear neuropathy manifestations and current ERT does not reach the brain due to tightly regulated brain cell barriers [4, 8, 10, 35]. Hence, the efficacy of ICAM-1-targeted nanoparticles to enhance enzyme delivery across the BBB with delivery to cells of the brain was demonstrated (Section 4.2.). This was done by thoroughly studying binding specificity to cells of the BBB and the brain (e.g. healthy versus diseased cells), internalization and/or transport efficiency into and across these cells, mechanism of internalization and/or transport, and intracellular trafficking to lysosomes in cells in culture. To our knowledge, this is the first time that transport of ICAM-1-targeted nanocarriers across brain cell barriers has been studied. Furthermore, in vivo work provided insight into circulation patterns, biodistribution to peripheral organs and, notably, the brain, and tissue specificity of enzyme delivered by ICAM-1-targeted nanocarriers compared to non-targeted enzymes, unique to the enzyme delivered (Section 4.3.). Lastly, we also describe for the first time that ICAM-1-targeted nanocarriers bearing enzyme cargo can be modulated to enhance enzyme delivery without negatively affecting targeting specificity by altering the formulation to shift the density ratio of enzyme cargo to targeting moiety and by increasing the concentration of the administered dose (Section 4.4.).

In summary, the results from this dissertation portray that the potential of enhancing delivery of therapeutic enzymes by ICAM-1-targeting strategies for LSD treatment is not unique to ASM. ICAM-1-targeting platform can be used to enhance delivery of at least two other lysosomal enzymes, α Gal and GAA for treatment of FD and PD, as shown in this work

[47, 48]. Additionally, we note that ICAM-1-targeting can assist in delivery across cell barriers to intractable tissue, a poignant challenge in current ERT treatment. In fact, ICAM-1-targeted nanocarriers were transported across the BBB [49] and targeted cells of the brain in cell culture, paralleling with accumulation of lysosomal enzyme in the brain of mice [47, 48, 50], important for treatment of neuropathic symptoms evident in several LSDs [16]. Furthermore, ICAM-1-targeting nanocarriers can be modulated to modify the amount of enzyme delivered to tissue. Interestingly, different formulations of ICAM-1-targeted nanocarriers carrying different enzyme cargo show differences in binding, internalization, lysosomal trafficking behavior and distinct in vivo biodistribution patterns, depicting a unique relationship between the particular enzyme cargo and ICAM-1-targeting system [47]. Hence, this emphasizes that cell culture and in vivo studies to investigate and optimize further applications of ICAM-1-targeting strategy for treatment of other LSDs must be carried through individually. Nonetheless, ICAM-1-targeting strategy is promising to improve current ERT for LSD treatment, especially as a systemic treatment that can target diseased tissue and deliver enzyme to the lysosome of cells via a non-classical route, bypassing M6PR-mediated uptake of these enzymes, which is impaired in some LSDs [27-29, 51].

SECTION 2: BACKGROUND

2.1. Lysosomal storage disorders

Lysosomal storage disorders (LSDs) are a group of rare inherited metabolic diseases comprised of more than 40 different diseases and have been reported to plague as many as 1 in 2000 newborns every year [1-9]. LSDs are individually classified based on the lysosomal-associated protein dysfunction that leads to complications [16]. Dysfunctional lysosomal-associated proteins leading to particular LSDs can include lysosomal enzymes, lysosomal enzyme activator proteins, proteins in ion pumps in the lysosomal membrane, proteins involved in intracellular vesicular trafficking, or other transport machinery [52].

Lysosomes are membrane-enclosed intracellular vesicular organelles that are dynamic and constitute ~5% of intracellular space in mammalian cells [53]. Lysosomes are crucial for the cell homeostasis and, therefore, tissue and organ structure and function [53, 54]. They function to maintain a cell's homeostasis by degrading different extracellular substrates that the cell accumulates through endocytosis or intracellular substrates through autophagy (e.g. lipids, nucleic acids, proteins, sugars). Lysosomes also play a role in assisting disposal of invasive pathogens and in repair of damaged plasmalemma lipids and proteins by removal of these lipids and/or proteins and/or supplying monomeric subunits to rebuild it [53-59]. To digest these substances and objects, lysosomes contain more than 50 acidic hydrolases that are active in an acidic environment, pH of 4.5 to 5.0, which is maintained in lysosomes by proton pumps and H⁺-ATPases [54, 55, 60, 61]. These hydrolases are not active in neutral environments (e.g. the cytoplasm with a pH of ~7.2), thereby restricting the enzymatic activity to only digest contents within the lysosome [54, 55, 60, 61]. LSDs can

result if any function related to the lysosome fails or is faulty, putting the cell homeostasis in jeopardy.

LSDs can result from genetic defects affecting any of the lysosomal components, most commonly enzymes, where mutations on the genes encoding these enzymes can affect their synthesis, folding, catalytic activity, functionality, etc [61]. Low levels of lysosomal enzyme activity affect all cells at varying degrees, leading to a build up of these macromolecular substrates in the lysosome that results in cellular injury, tissue dysfunction, and multi-organ failure leading to death. Approximately half, if not more, of LSDs affect the central nervous system (CNS), particular in LSDs that manifests soon after birth [16, 62]. Other complications include, but are not limited to, cardiac, hepatic, renal, and splenic failure, depending on the deficient enzyme and substrate accumulation. Organomegaly, defects on the connective-tissue, ocular pathology, and vasculopathy are also common symptoms of LSDs. Such is the case for diseases used as LSD examples in this study, including Fabry disease (FD) due to deficiency of acid α -galactosidase A (α Gal), Type A and B Niemann-Pick disease (NPD) due to deficiency of acid sphingomyelinase (ASM), and Pompe disease (PD) due to deficiency of acid α -glucosidase (GAA) [45, 46, 63].

FD is an X-linked LSD caused by mutations of the GLA gene that encodes for α Gal. This results in a deficiency in functional α Gal, which leads to inefficient hydrolysis of glycolipids as galabiosylceramide and, mainly, globotriaosylceramide (Gb3), a side product of catabolized glycosphingolipid globoside that is a structural part of the plasma membrane [64]. As a result, excess Gb3 accumulates in lysosomes, preferentially in glycolipid rich cells, such as endothelial, epithelial, smooth muscle cells, etc, leading to a progression of cardiac conditions, vasculopathic complications, cerebrovascular manifestations, and renal failure [45].

Type A and B NPD are LSDs caused by mutation in the sphingomyelin phosphodiesterase 1 (SMPD1) gene, which encodes for ASM, resulting in a deficiency of active ASM. This leads to an excess accumulation of lipids, mainly sphingomyelin, a sphingophospholipid structurally prominent in cell membranes and a key player in signaling pathways such as apoptosis. Both type A and B NPD manifest complications in the lungs, liver, and spleen. In addition, type A NPD also severely affects the brain, leading to neurodegeneration and often death by age 2 or 3 years. On the other hand, type B NPD minimally affects cells of the brain, but more severely affects the lungs [63].

PD is an autosomal recessive LSD caused by mutations in the gene encoding GAA. These mutations lead to a deficiency of active GAA, resulting in excess accumulation of glycogen in all cells, an important form of energy storage. This disease markedly affects glycogen rich tissue, such as the liver and striated muscle cells (cardiac, respiratory, and skeletal muscles), resulting in muscle weaknesses and cardiopulmonary failure. In addition to the heart, liver, and muscles, this disease affects the vasculature and, sometimes, the brain [46].

Since deficient enzymes affect all lysosomes and, hence, all cells in both peripheral organs and the nervous system (although at varying degrees), a systemic drug delivery approach to treat LSD is crucial.

2.2. Treatments for LSDs and their challenges

Before the past two decades, the only treatment available for LSD patients was focused on supportive and palliative care [65]. With more studies leading to a better understanding of these diseases, the LSD research community has creatively developed new treatment

approaches. Research has focused on: 1) reduction of accumulated substrate, 2) augmentation of enzyme activity in cases where patients have residual enzyme activity, or 3) replacement of the deficient lysosomal enzyme. Combination of these therapies has also been proposed.

As mentioned, the cause of most LSDs is a defective lysosomal enzyme, leading to excess lysosomal accumulation of a particular substrate. Some patients synthesize normal amounts of enzyme, but is poorly active due to protein misfolding or instability [8, 52]. Hence, these patients can benefit from the use of substrate reduction therapy (SRT). This is a method where small molecules are used to restrict the synthesis of the enzyme substrate, thereby slowing the rate to allow endogenous residual enzyme to degrade the substrate at a manageable pace with optimal outcome [66]. Miglustat (Zavesca®, Actelion Pharmaceuticals Ltd, Allschwil, SWT), the molecule used as SRT for type I Gaucher disease and NPD type C, has gained clinical approval [66, 67]. Although promising results have been seen, serious side effects and metabolic imbalances have also been reported, and this treatment is often combined with other modalities [8].

Another strategy researchers have developed to treat LSD patients with innate low enzyme activity levels is to enhance the activity of the endogenous enzyme (enzyme enhancement therapy, EET). This has been pursued using small molecules for pharmacological chaperone therapy (PCT). Some LSDs can manifest due to enzyme misfolding or unfolding, e.g. 80% of patients diagnosed with non-neuronopathic Gaucher disease which is caused by a deficiency of active β -glucosidase [67]. Misfolded or unfolded enzymes are often halted upstream in the protein synthesis route, i.e. in the endoplasmic reticulum, with the mutated protein never reaching the lysosome and degrading in the endoplasmic reticulum. Pharmaceutical drugs act as “chaperones” to restore endogenous misfolded proteins by at least partially assisting them to fold into a functional conformation such that the enzyme is stabilized and can traffic from the endoplasmic reticulum to the Golgi

apparatus and downstream to the lysosome [66, 67]. Hence, with the assistance of PCT the now active enzyme can possibly reach the lysosome to degrade the accumulated substrate. Although positive outcomes have been obtained, this approach is only helpful for LSDs caused by misfolded or unfolded enzyme, limiting PCT as a therapeutic option to only a few cases and necessitating identification of the precise mutations involved [66, 68].

Gene therapy is another strategy pursued in order to treat LSDs. Most gene therapy efforts focus on complete replacement of the gene that encodes the defective enzyme, opting for the potential of absolute correctness and a long-term effect. This treatment method may be a viable treatment option for patients with rare LSDs [65]. For decades, researchers have conjectured the potential of gene therapy to directly transfer the normal gene for enzyme synthesis into deficient cells, through *in vivo* (injection of recombinant cDNA) or *ex vivo* transfection of cells from the patient followed by implantation, using viral vectors (e.g. adenovirus, adeno-associated virus, lentivirus, retrovirus) or non-viral vectors (e.g. liposomes, particles, Lipofectin®-peptide complex, CMV promoter driven or TAT-tagged pDNA) [69, 70]. Optimistically, initial successes were seen in mouse models; however, safety concerns of this approach have not been thoroughly addressed yet, mainly because the risks are still unknown [65]. Some clinical trials have showed leukemia-like disease developing in human patients treated with gene therapy, seemingly a result of insertional mutagenesis presented by the implanted transfected cells [70]. Regardless, more research is currently being conducted to optimize this approach.

Stem cell transplantation has also been tested, such as bone marrow transplantation (BMT). Bone marrow mesenchymal stem cells provide a clean slate of cells that can be differentiated into several healthy cell types based on their environment. Similar to other methods previously discussed, BMT has provided relief in peripheral organs affected by the LSD [71]. BMT has also shown promise in preventing deterioration of the nervous system in

a few LSDs, although results remain fairly unpredictable depending on timing of treatment [72, 73]. Yet, for more severe neuropathic LSDs delivery of treatment to the CNS is still difficult due to the BBB. To mediate this, mesenchymal stem cells extracted from the bone marrow can be directly injected into the brain to form functioning neuronal networks [20, 74]. However, this is highly invasive and risky. Serious complications and side effects have been seen in human trials, including issues with graft versus host disease [21, 22]. Another stem cell transplantation approach is extracting hematopoietic stem cells from umbilical cord blood. Previous work in immune deficient mouse models showed these cells to cross the BBB and differentiate into healthy cells that produce the wild-type protein in the brain [75, 76]. However, similar to BMT, graft versus host disease is a concern [76].

Lastly, the most common and clinically available treatment method for LSDs is enzyme replacement therapy (ERT). ERT consists of systemic injections of recombinant lysosomal enzymes in hopes that this reaches the diseased tissue and enters cells to traffic to the subcellular target organelle, the lysosome (Figure 1). This method was first proposed by Dr. DuVe in the 1960s [10].

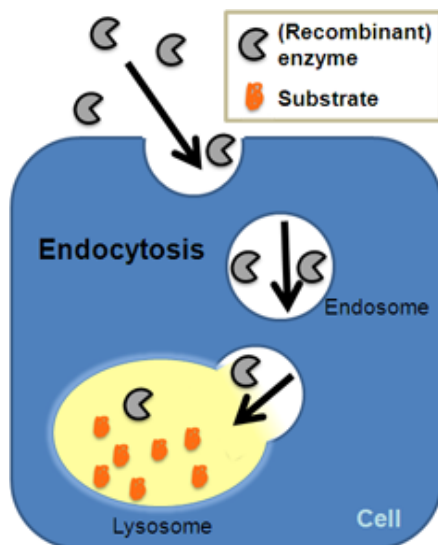


Figure 1. Enzyme replacement therapy (ERT) for lysosomal storage diseases (LSDs). Lysosomal enzymes (isolated from tissue or organism, or recombinant) are intravenously (i.v.) administered and anticipated to be endocytosed, and intracellularly trafficked to the lysosome.

2.3. Enzyme replacement therapy for LSDs

In the 1960s, the first LSD was classified as such and within that same decade ERT was first tested. Unaltered GAA extracted from *Aspergillus niger* fungus or human placenta were intramuscularly and i.v. injected into infants with Pompe disease. This resulted in little effect, however moderate reduction of glycogen in the liver showed the potential of using this method [52, 77, 78]. This strategy was improved upon by observing the natural mechanism by which endogenous lysosomal enzymes are synthesized and targeted. Endogenous lysosomal enzymes are post-translationally modified in the Golgi apparatus to incorporate mannose-6-phosphate (M6P) residues which bind to M6P receptors (M6PR) and are then trafficked from the Golgi apparatus directly to lysosomes via clathrin coated vesicles [79-81]. Also, a fraction of these enzymes are secreted to the extracellular milieu. There, M6P containing enzymes bind to M6PRs present on the plasma membrane, resulting in clathrin-mediated endocytosis and traffic to lysosomes [79-81]. Understanding how endogenous lysosomal enzymes could be trafficked to lysosomes from the extracellular milieu facilitated scientists to design ERT strategies. The recombinant enzymes used in ERT must contain M6P to target M6PR on the cell surface [82, 83]. Current technology to scale up production of recombinant enzymes and our ability to study proof-of-concept ERT in existing animal models have led to the development, testing, and clinical implementation of ERT.

Currently, ERT is approved for only six out of more than 40 LSDs. Type A and B NPD does not have a clinically available ERT option yet. On the other hand, ERT for FD and PD are available, albeit suboptimal, as discussed below. Fabrazyme® (Genzyme Corporation, Cambridge, MA) or Replagal® (Shire Human Genetic Therapies, Wayne, PA) are available for FD treatment, while Myozyme® and Lumizyme® (Genzyme Corporation, Cambridge, MA) are used to treat PD [10]. Fabrazyme, Replagal, Myozyme, and Lumizyme are examples

of ERT products largely successful in ameliorating LSD symptoms, especially in peripheral organs such as the liver and kidneys [35, 84, 85].

Despite ERT's effectiveness at alleviating symptoms in some peripheral organs, several tissues remain minimally treated, such as the brain, heart, and vasculature [34, 86-88]. Hence, even with ERT, LSD may still cause multiple organ complications and failures [34, 86-89]. This could be due to the fact that although M6PR exists on most mammalian cells, expression is not uniform in all cells [80, 90]. In fact M6PR expression in organs shifts with age [91, 92], with expression of cation-independent M6PR becoming more prevalent in reticuloendothelial system (RES) organs with age, such as the liver [92]. Also, M6PR expression does not correlate to the homeostasis state of the cell, hence, targeting enzymes to M6PR does not predominately target enzymes to cells that are pathologically affected. Naturally occurring filtration by kidneys and clearance by RES may explain the preferential distribution of ERT to these organs. Even though some RES organs are targets for intervention, all tissues are affected and require treatment [93, 94]. Such is the case for ERT for FD and PD, and ERT for NPD that was under trial [10]. Additionally, the circulating recombinant enzymes ($t_{1/2}$ ~10 to 20 minutes [10]) tend to be attacked by the immune system, including uptake by macrophages and anti-enzyme antibodies [95-100]. Some benefit does arise from delivering recombinant enzymes to diseased macrophages, such as in the case of treatment for Gaucher disease [100], but this also rapidly prevents enzymes from reaching other affected cells. Also, antibody against the injected enzyme develops, leading to resistance, as seen in ERT for FD and PD [95-101]. In addition, targeting M6PR may be viable for only some LSDs. Cellular uptake dependent on M6PR is reliant on clathrin-mediated endocytosis, which has been observed to be disrupted in several LSDs [27-29, 51]. A method to deliver lysosomal enzymes via bypassing clathrin-mediated endocytosis may be a more viable option.

Therefore, although ERT is promising and shows improvements in certain organs, it still proves to be suboptimal, lacking predominant targeting of diseased cells and capitalizing on defunct endocytosis routes for therapeutic uptake.

2.4. Drug delivery systems for treatment of LSDs

ERT improvement could perhaps be achieved by using drug delivery systems. For instance, the development of nanotechnology has enabled drug delivery through the development of nanoscale drug carriers (nanocarriers, Figure 2).

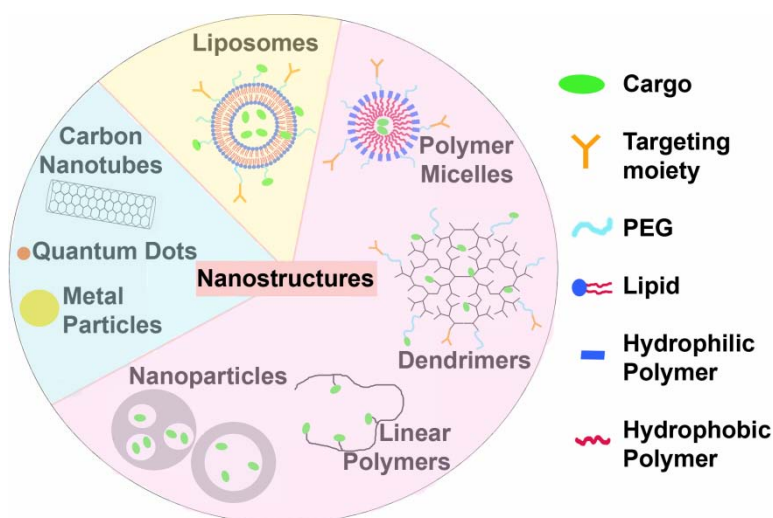


Figure 2. Examples of compositions and architecture of carriers and other assemblies used for drug delivery. The group shaded in blue corresponds to inorganic nanocarrier formulations, the groups shaded in yellow or pink are examples of biomolecule or polymer based nanocarrier formulations, respectively. (Figure reproduced from [102]).

Nanocarriers are macromolecular assemblies that improve the delivery of therapeutic and/or imaging agents by enhancing and/or controlling solubility, bioavailability, circulation time, biodistribution, and cargo release rate [102]. Nanocarrier material can be derived from biomolecules (lipids, DNA, protein) or can be synthetics (inorganic, organic), or hybrid. Depending on the particular composition, these systems can assist in drug stability,

biodegradability, biocompatibility, tissue targeting, etc. In addition to the material of nanocarriers that make them unique, the structure of nanocarriers also plays a role in its function. Nanocarriers can take shape in linear form (linear polymers), spherical solid particles (quantum dots, metal particles), porous particles (carbon nanotubes), hollow or porous capsules (micelles, liposomes), or highly branched, tree-like structures (dendrimers), among many others.

Biomolecule-based nanocarriers are attractive compared to all inorganic structures since risks are still relatively unknown and necessitate research to better understand toxicity. As an example, recent studies found that multiwall carbon nanotubes can induce cell permeability and risk increasing inflammation markers [103]. Biomolecule-based nanocarriers can be constructed of lipids, proteins, organelles, etc, which are deemed relatively biocompatible. The oldest examples studied are lipid-based formulations. Liposomes are lipid-based nanocarriers (50 nm to several μm in diameter) that form a shell with a bi-layer of phospholipids such that the lumen is an aqueous space that can hold hydrophilic macromolecules. The lipids forming the bi-layer are similar to a cell membrane, which is the distinct factor that makes liposomes highly biocompatible [104]. Lipid-micelles have also been attractive. They are constructed with a single layer of lipids, forming a hydrophilic shell with a hydrophobic core that can be loaded with hydrophobic molecules [105]. Nanocarriers can also be constructed with biocompatible proteins, which are low in cytotoxicity and can be formulated and structurally fabricated to bind well with the drug cargo [106]. Interestingly, to avoid immune rejection and ensure biocompatibility, natural cellular organelles have been extracted and loaded as nanocarriers for drug or gene delivery, such as exosomes [107]. Also, as an example of micrometer size carriers, whole cells have been extracted and loaded, such as erythrocyte ghosts [107].

Nonetheless, for decades, polymer nanocarriers fabricated with synthetic, natural, or a hybrid of synthetic and natural materials have been the most popular and widely used drug delivery systems due to good control of charge, size, shape, and structure (hydrophobic versus hydrophilic, hollow versus solid versus porous, linear versus particle versus dendrimeric) [102]. Some examples include polymersomes, similar to liposomes but constructed with block copolymers as opposed to lipids, polymeric micelles, and polymer dendrimers [102]. Some examples of synthetic polymers are polyanhydrides, polycaprolactone, poly(ethylene glycol) (PEG), poly(ethylenimine) (PEI), polylactides, polyglycolides, poly(lactide-co-glycolide) (PLGA), polyorthoesters, and poly(vinyl alcohol), most of which are minimally toxic and therefore regarded as biocompatible [102]. PLGA is commonly proposed in drug delivery since it is a material that has been previously used in FDA-approved devices (e.g. sutures, grafts, and prosthetics) and has been repeatedly proven to be biocompatible [108]. Moreover, PLGA's degradability can be controlled, which is advantageous for monitoring drug release, and its size and structure modified by shifting the lactic to glycolic acid ratio [109]. In fact, several PLGA-based drug delivery systems are already approved for clinical use and several more are currently investigated [110, 111]. Degradation of some polymers can be controlled by calculating the biodegradation rate of the formulation, deeming it effective for controlling the release of a loaded cargo. Some polymers can mask the cargo from immune recognition, thereby prolonging circulation time and potentially improving tissue delivery, e.g. PEG [109, 112, 113]. Additionally, some polymer nanocarriers can protect active enzymes from proteolysis [114].

Drug delivery systems have been widely applied to several therapies, including those aimed at LSDs. In fact, one of the first applications of liposomes studied in the 1970s was the encapsulation of enzymes for LSD treatment [115]. One major setback to currently available ERT is the development of antibody against the drug after long-time use in patients [95-99,

101]. Encapsulation could mitigate this by shielding the enzyme until delivered to lysosomes within cells. Efficiency of enzyme delivery to cells was improved by liposomes, but release of the enzyme cargo into the cytosol or other non-lysosomal compartments was observed [115]. Yet, altering liposome formulations (e.g. by coating liposomes with PEG) showed to prolong circulation and therapy activity by days [116]. PEG can also add ‘stealth’ properties [54, 117-119] and can be used to directly modify enzymes, e.g. PEG-modified dextranase encapsulated in liposomes prolonged circulation time without immune-recognition [117]. Calcium alginate microspheres have also been studied as a potential drug delivery vehicle that encapsulates therapeutic enzymes for a prolonged release [120]. However, this method can only be used for localized release, requiring implantation [120]. In addition, the use of drug delivery systems also applies to delivery of gene therapies, such as exploiting solid lipid nanoparticles to deliver plasmid that codes for α Gal, which has shown great potential of inducing production of functional α Gal in cells [121]). This could be also used, hypothetically, in SRT. Yet, the use of drug delivery systems for LSD treatment remains largely unexplored [62].

2.5. Targeting strategies for treatment of LSDs

Lysosomal ERTs available today are i.v. administered by injecting the therapeutic enzyme into the vasculature to target cells that express M6PR for intracellular lysosomal delivery via clathrin-mediated endocytosis [82, 83]. However, M6PR expression is not uniform through tissues, does not differentiate healthy from diseased affected tissue, and the associated clathrin pathway is affected in some LSDs [27-29]. Hence, targeting M6PR may contribute to suboptimal effect observed [27-29]. Additionally, M6PR-based ERT does not cross cellular barriers (e.g. brain) to deliver therapeutic enzyme to certain tissues [27-29, 122]. Suboptimal

accumulation in affected organs, lack of delivery across cell barriers to intractable tissues, and limited intracellular delivery of ERT should be improved. This could be achieved by utilizing a targeted drug delivery system, which has the potential to shield the therapeutic enzyme from immune recognition and exploit a different targeting strategy to improve enzyme transport across cell barriers, distribution to main target organs, selectivity toward diseased cells, and internalization and lysosomal delivery in cells through an M6PR-/clathrin-independent pathway.

Targeting a therapeutic in a physiological system means to mediate an interaction between the therapeutic with the system. This interaction can be mediated for delivery of therapeutics with the assistance of the material of the drug delivery system (e.g. shape, size, material properties, etc.), but the most common way of active targeting is ligand-mediated. In fact, ligand-mediated binding occurs frequently in normal physiology functions (e.g. neurotransmitters bind to receptors on neurons for uptake into the cell [123]), even in pathophysiological circumstances (e.g. virus infection [124]). To achieve this targeting strategy targeting moieties are often exploited, especially in an effort to address select sites by promptly binding to specific molecules. Targeting moieties can include a vast variety of molecules, such as proteins, peptides, nucleotides, sugars, small molecules, etc [24]. Mainly antibodies are used due to their high affinity and specificity towards their targets. Antibodies can be conjugated directly to therapeutics or to drug delivery vehicles carrying said therapeutics. Additionally, due to immune response concerns with using antibodies, fragments of antibodies, specifically the variable binding domains, have been developed to conserve antibodies' high affinity and specificity to distinct targets without the recognizable Fc region that results in clearance and/or immunorecognition [125-127]. Natural ligands to cell receptors are also widely used as they inherently bind to respective cell receptors without necessitating modification, e.g. hormones, low density lipoproteins (LDL), transferrin, etc

[24]. Similarly, small molecules such as vitamins (e.g. folate, vitamin B12) and sugars (e.g. monosaccharide mannose) are exploited to bind to their respective cell surface receptors with minimal modification necessary [24].

Combining targeting strategies to drug delivery vehicles can enhance delivery of therapeutics by increasing biocompatibility of the loaded therapeutic, promoting stealth-like properties, selective binding and transport, and control release of the carried cargo, thereby improving bioavailability of the carried therapeutic. Currently, fast clearance and lack of protection of ERT yields enzyme degradation (e.g. by proteases) in circulation. By loading the enzyme on a drug delivery vehicle, the enzyme circulation half-life may improve and these molecules can be shielded from immune recognition. In combination with a rapid targeting, clearance could be minimized with more enzyme being available to distribute to other organs.

Methods to use targeted drug delivery vehicles to improve ERT have been studied. Exploiting liposomes to deliver enzymes for LSDs was introduced in the early 1960s. However, much of the work noted that liposomes may protect enzyme during circulation and even extend enzyme activity to days (versus hours of non-encapsulated enzyme) but does not avoid clearance, ~70% of the dose still accumulated into the liver [116]. This may be beneficial for LSD that exhibit storage in the liver, but the lack of enzyme distribution to other organs suggests that other affected tissue would not be efficiently treated. Hence, by the 1970s, Finkelstein and Weissmann suggested to improve and refine delivery of liposome-encapsulated enzyme to certain cell types by incorporating ligands recognizable by cell surface receptors into liposomes or coated onto liposomes [115]. Yet this idea was only tested to improve liver delivery [24]. Today, researchers focus on other targeting strategies. For instance, fusion proteins provide a glycosylation-independent mechanism of enzyme targeting. LSD enzyme β -glucuronidase (Mucopolysaccharidosis VII) was targeted to a

different domain on M6PR by fusion with a 67-amino acid peptide fragment from insulin-like growth factor II (IGF-II) that interacts with the binding site IGF-II/M6PR, which improved delivery of enzyme to the heart, kidney, lungs, versus that of non-targeted counterpart [11, 62, 128]. Also, when GAA was fused with IGF-II peptide fragment to treat Pompe disease mice, delivery to target tissues (heart and skeletal muscle) was improved compared to currently available GAA ERT, yet, the liver (which is not a Pompe disease target) still accumulated more enzyme [129]. Alternative to targeting M6PR, targeting of other receptors have also been studied. Specifically, GAA (Pompe disease), and α -L-iduronidase (Hurler syndrome) were fused with receptor-associated protein (RAP) to target LDL receptor, transferrin to target transferrin receptor (TfR), or a peptide from an antibody specifically targeted to the insulin receptor (InsR) [12, 24, 62]. Interestingly, preparing fusion proteins may not be necessary: e.g. simply mixing recombinant enzyme with a targeting peptide consisting of tripeptidyl peptidase I with a 36-amino acid peptide composed of an apoE peptide and polylysine to treat Neuronal ceroid lipofuscinosis, prior to injection, was sufficient to improve targeting to the brain [130]. These methods demonstrate that targeting alternative to M6PR is valuable in improving enzyme biodistribution. Yet, the combination of targeting strategy and drug delivery system is still poorly explored.

2.6. Endocytosis and subcellular transport of drug delivery systems for LSD treatment

Transport across cellular barriers is necessary when therapeutic agents (such as lysosomal ERT) are aimed to treat tissue beyond the vasculature. In this case, targeting strategies can be directed to either enhance the paracellular transport between cells or the transcellular transport through cells (Figure 3). Depending on the treatment, the paracellular route of

transport by opening all junctions may be relatively unsafe unless very transient [26, 105, 131-133]. To achieve transcellular transport, the therapeutic must first be endocytosed into the cell from its apical membrane, then trafficked through the cell body via vesicular transport, and then exocytosed from the basolateral membrane of the cell. One method to achieve uptake is targeting cell markers that induce trafficking to distinct subcellular organelles, such as those exploited by the shiga and cholera toxins that target molecules of the cell surface and induce uptake and trafficking to the Golgi and endoplasmic reticulum [24, 134, 135]. Another method is to initiate transcellular routes by targeting pathways that inherently exist, such as folate, insulin, LDL, or transferrin receptors with corresponding ligands. Often, these targets uptake bound material and transport them via classical endocytosis/transcytosis routes, clathrin- or caveolae-mediated pathway [24].

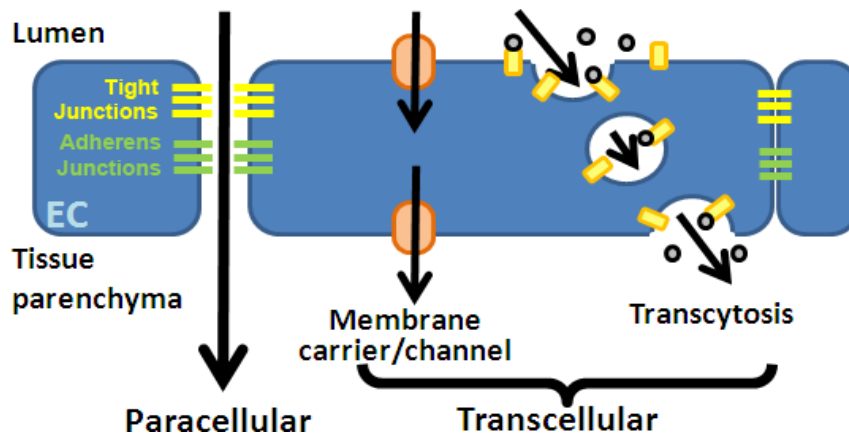


Figure 3. Paracellular versus transcellular transport across a cell barrier. Delivery of therapeutics to tissue often requires transport across cell barriers. Transport across cell barriers occurs via one of two key pathways of transport: paracellular (between cells) and transcellular (across cells). The latter route is mediated by either membrane transporters or channels or vesicular transcytosis.

Vesicular transport similar to that emphasized for transcytosis can be used to achieve lysosomal transport. This can be achieved by inducing engulfment as a result of immune recognition or by using specific targeting agents. If macrophages and or phagocytic cells are the target, as is the case for Gaucher disease and some other LSDs, then inherent enzyme engulfment by these cells would situate the enzyme in lysosomes of the target cells [100]. However, if these cells are not the intended targets, other strategies must be used. As discussed above, fusion proteins are a promising targeting strategy for delivering lysosomal enzymes for treatment of LSDs (Section 2.5.). In fact, a major setback for currently available ERT to treat LSDs is its ineffectiveness to deliver therapeutics to treat difficult to reach tissue, specifically target tissue that require therapeutics to cross cell barriers (e.g. brain). Fusion proteins can potentially mitigate this impediment. Studies showed that fusion of α -L-iduronidase with peptide binding fragment from apolipoprotein E (apoE) to target LDL receptor, from antibody targeted to InsR, or from antibody targeted to TfR helped deliver enzymes across the BBB to the brain [136-138]. Interestingly, one study showed that treating mothers with fusion proteins of β -glucuronidase with Fc domain of IgG targeting neonatal Fc receptors delivered the enzyme to the Mucopolysaccharidosis VII model mouse fetuses, crossing the placenta. However, all the above targeting strategies discussed (targeting InsR, LDL receptor, M6PR, TfR) capitalize on clathrin-mediated endocytosis for uptake of enzyme into the cell and trafficking to lysosomes, which does not address the issue of clathrin-impairment present in some LSDs [27-29]. Therefore, an alternative pathway must be targeted to traffic therapeutic enzymes to the lysosomes.

2.7. ICAM-1-Targeting strategies for LSD applications

Targeting and transport strategies often observe and take advantage of ligand-receptor binding examples that occur naturally. One target molecule of interest is intercellular adhesion molecule-1 (ICAM-1), a transmembrane glycoprotein that's expression is naturally upregulated on cells under stress, such as in pathology. Its role is to allow leukocyte adhesion to inflamed tissue [139]. ICAM-1 is expressed on most cell types, including epithelial cells, fibroblasts, macrophages, neurons, tumor cells, but most prominently expressed on endothelial cells that line the vasculature [39]. Hence, its placement on endothelial cells of the vasculature is convenient to assist transportation of leukocytes from circulation and to inflamed tissue.

ICAM-1 has an extracellular region with 5 domains, one single transmembrane-spanning domain, and an intracellular cytosolic tail [39]. Binding of extracellular domains triggers intracellular signaling mediated by the cytosolic domain. The signaling cascades triggered by binding of ICAM-1 vary amongst cell types and triggering ligands [39]. Some activated signaling cascades can involve cell survival and apoptosis [140] and some involve stress response and apoptosis [141].

Due to its role in inflammation, ICAM-1 expression can mark sites affected by disease. In fact, diagnostic methods have been developed to visually monitor disease progression by tracing ICAM-1 [142, 143]. Beyond diagnostic purposes, targeting ICAM-1 can enhance drug delivery. If ICAM-1 is bound by anti-ICAM or anti-ICAM decorated nanocarriers (anti-ICAM NCs), it potentially creates steric hindrance by physically blocking leukocytes from binding to ICAM-1, theoretically acting as an anti-inflammatory agent [144, 145]. Additionally, the expression profile of ICAM-1 and its enhancement in diseased-tissue is attractive for drug delivery requiring systemic assistance and targeting for more precise

delivery of drugs to specific locations [144, 146-156]. Indeed, our previous work confirmed that anti-ICAM NCs bound significantly more to diseased cell models (endothelial cells treated with TNF α to mimic pathological conditions) than to non-treated healthy cells [157].

To control targeting and endocytic rate without affecting endocytic route, the size and shape of anti-ICAM drug delivery systems can be adjusted, e.g. 100 nm to 5 μ m carrier diameter, spherical- versus disk-shaped [158, 159]. Small spherical carriers bind and are endocytosed faster than larger and/or non-spherical shaped anti-ICAM NCs. Hence, to study enzyme delivery treatment for LSDs, 100-nm diameter spherical NCs coated with anti-ICAM and cargo to optimize coating density and bulk delivery for quick binding and uptake into cells seemed appropriate. Another method to control endocytic rate of anti-ICAM nanocarriers is to engineer the system to distinctly target specific or combinations of various epitopes of ICAM-1 [160]. Or, delivery of ICAM-1-target vehicles can be additionally loaded with biologics that can trigger more rapid signaling pathways to enhance delivery [161]. Another method to minimize size of anti-ICAM NCs is to replace whole antibody molecules with anti-ICAM targeting fragment, peptides, or ligands, which has shown to still efficiently achieve ICAM-1-targeting [125]. Additionally, this method may help anti-ICAM NCs evade immune recognition. Indeed, using monomolecular anti-ICAM approach would minimize size and eliminate the large size of nanoparticles. However, binding as a result of monomolecular anti-ICAM potentially induces different response and distribution profile than multivalent anti-ICAM drug delivery system [152, 162]. Although little is known of monomolecular anti-ICAM conjugated drug delivery, the distribution pattern of delivered cargo (e.g. enzyme therapeutic) can be expected to be different compared to the drug delivery pattern of its multivalent anti-ICAM drug delivery system counterpart.

Bound multivalent anti-ICAM drug delivery systems trigger vesicular endocytosis [40]. The resultant endocytic mechanism of ICAM-1-targeted drug delivery systems is via

cellular adhesion molecule (CAM)- mediated endocytosis, independent of the classical caveolae- or clathrin-mediated endocytosis pathways and different from phagocytosis and macropinocytosis [40]. This pathway involves signaling cascades commonly observed when ICAM-1 is bound by its natural ligand, leukocytes [39]. This novel endocytic pathway route is advantageous for diseases requiring an alternative treatment delivery pathway to the classical endocytosis routes, such as LSDs [27-29, 51]. In fact, anti-ICAM NCs transport across gastrointestinal epithelial cell monolayer is also mainly through CAM-mediated transport [43]. This parallels well with known occurrences of micron size leukocyte extravasation from circulation to tissues, without opening endothelial cell junctions [38, 39], and is promising for therapies requiring endocytosis and transport via an alternative to classical pathway.

In this thesis we focus on improving delivery of lysosomal enzymes for LSD treatment using ICAM-1-targeted NCs (anti-ICAM/enzyme NCs). We note that the previous discussed issues with ERT can be addressed and/or avoided using anti-ICAM NCs. Specifically, in Section 4.1. we discuss our findings of enzyme loaded anti-ICAM NCs (anti-ICAM/enzyme NCs) internalized into LSD-model cells via CAM-mediated endocytosis in culture, and delivered enzyme efficiently to lysosomes to degrade accumulated substrate [42, 47, 48]. This bypasses the impaired clathrin-mediated route current ERT utilizes [27-29, 51]. Granted, our previous work with anti-ICAM/ASM NCs showed promise for improving ERT for Type A and B NPD [42]. However, for the first time, we show in this thesis that anti-ICAM NCs can be used as a generic platform with the potential to improve ERT delivery for Fabry disease and Pompe disease [47, 48]. Moreover, current ERT is unable to deliver therapeutic enzyme to the brain [4, 8, 10, 35]. In Section 4.2., we discuss for the first time how anti-ICAM/enzyme NCs can cross BBB cell models to target cells of the brain. Furthermore, in Section 4.3., we show that anti-ICAM NCs enhanced enzyme delivery to all

organs analyzed in vivo by several folds as compared to non-targeted enzymes, which includes intractable tissues, such as the brain and previously noted tissues that ERT was incapable to sufficiently treat, such as the heart, skeletal muscles, and vascular-rich lungs [4, 8, 10, 34, 35, 41, 42, 47, 48, 86-88]. Since LSD is a systemic pathology, affecting all cell types at varying degrees of severity, it is beneficial to deliver treatment to all tissue. Lastly, in Section 4.4., we discuss the potential of optimizing enzyme delivery, without negatively affecting enzyme biodistribution, by modulating anti-ICAM/enzyme NC formulation.

Section 3: Methods

3.1. Antibodies and reagents

Monoclonal antibodies to ICAM-1, R6.5 (mouse anti-human) [139] and YN1 (rat anti-mouse) [163], were purified from hybridomas and obtained from ATCC (Manassas, VA). Non-specific mouse or rat IgG, as well as fluorescently labeled secondary antibodies, were purchased from Jackson ImmunoResearch (West Grove, PA). Neutral α -galactosidase (α Gal; ~32.25 kDa) from *Escherichia coli* or green coffee beans were purchased from Calbiochem (San Diego, CA) and Sigma-Aldrich (St. Louis, MO). Recombinant neutral α -glucosidase (GAA; ~68.5 kDa) from *Saccharomyces cerevisiae* was also from Sigma-Aldrich (St. Louis, MO). Recombinant human acid sphingomyelinase (ASM; ~75 kDa) was kindly provided by Dr. Edward Schuchmann (Mount Sinai School of Medicine; New York, NY). Fluoresbrite® polystyrene latex particles of 100-nm diameter size were from Polysciences (Warrington, PA). Radioisotope labeling with 125 Iodine was done using Na^{125}I from PerkinElmer (Waltham, MA) and Iodogen pre-coated tubes from Thermo Fisher Scientific (Waltham, MA). Unless stated otherwise, all cell culture media and related supplements were from Cellgro (Manassas, VA) and all other reagents were from Sigma-Aldrich (St. Louis, MO).

3.2. Iodination of proteins

Radioisotope labeling of antibodies or enzymes with 125 Iodine was done by incubating ~20 μCi of Na^{125}I from PerkinElmer (Waltham, MA) and Iodogen beads or Iodogen pre-coated tubes from Thermo Fisher Scientific (Waltham, MA) with 100 μL of 1 $\mu\text{g}/\mu\text{L}$ protein for 5 minutes over ice. Free ^{125}I not bound to the protein was removed from the iodinated

protein mixture through centrifugation (1000g for 4 minutes) in a 6 kDa cutoff gel size exclusion column (Biorad, Hercules, CA), which eluted only the iodinated protein. Prior to filtering the iodinated protein, the column was inverted several times to thoroughly homogenize the gel, then washed with 2 mL of phosphate-buffered saline (PBS), and packed by centrifugation (1000g for 1 minute). The concentration of the eluted iodinated protein was determined with a Bradford assay compared to known bovine serum albumin (BSA) concentrations. The amount of free ^{125}I still remaining in the eluted iodinated sample was estimated by performing trichloroacetic acid (TCA) precipitation assay by mixing 2 μL of iodinated protein to 1 mL of 3% BSA-PBS (PBS supplemented with 3% BSA) and 0.2 mL of 100% TCA to precipitate the iodinated protein. After a 15 minute incubation period at room temperature, TCA samples were centrifuged (2755g for 5 min) and the supernatant was measured for ^{125}I content using a gamma counter (2470 Wizard2; PerkinElmer; Waltham, MA). From this, the percent of free ^{125}I was determined and subtracted to estimate the specific activity of the iodinated protein (CPM/ μg).

3.3. Nanocarrier preparation and characterization

Model polymer nanocarriers (NCs) were prepared as described [47, 48], by adsorbing (hydrophobic interactions) either enzyme (ASM, αGal , or GAA), control non-specific IgG, a mix of anti-ICAM and IgG (95:5 or 40:60 mass ratio), or a mix of anti-ICAM and enzyme (95:5 or 50:50 antibody-to-enzyme mass ratio) on the surface of 100-nm diameter, FITC-analog labeled polystyrene particles (enzyme NCs, IgG NCs, anti-ICAM NCs, anti-ICAM/enzyme NCs). Non-coated counterparts were separated by removing the supernatant after centrifugation (13.8g for 3 minutes), and coated nanocarriers were resuspended at the indicated concentration in 0.3% BSA-PBS for in vivo experiments or with 1.0% BSA-PBS

for in vitro cell culture experiments, followed by gentle sonication to prevent aggregation (~25 pulses for 5 seconds at ~22.5 μm amplitude, using a sonicator with a set output frequency of 22.5 kHz; Microson™ XL2000; Qsonica, LLC; Newtown, CT). A resultant final concentration of $\sim 6.8 \times 10^{11}$ NCs/mL and ~ 50 μg of protein/mL of prepared nanocarriers was obtained, and was then further diluted by 10-folds in complete medium supplemented with 1% BSA for cell culture experiments. Concentration of nanocarriers used in mice experiments varied (as indicated below) between $\sim 1.8 \times 10^{13}$ to $\sim 8.2 \times 10^{13}$ NCs/kg mice, which equated to $\sim 1.3 \times 10^3$ to $\sim 6.0 \times 10^3$ μg of protein/kg mice. Where specified, the targeting antibody or enzyme cargo was labeled with ^{125}I for radioactive tracing or NIR fluorophore (Alexa Fluor 750; Invitrogen; Carlsbad, CA) for fluorescence tracing.

The number of antibody and/or enzyme molecules per nanocarrier was determined by using ^{125}I -labeled antibodies or enzymes to coat nanocarriers, as stated above. The total ^{125}I -count remaining in the nanocarrier preparation was divided by the total number of nanocarriers coated to calculate total CPM/NC. This value was then multiplied by the known specific activity of the iodinated protein (CPM/ μg) to determine the total mass of protein coated per NC, which could then be converted to molecules or protein per nanocarrier by Avogadro's constant and the protein's molecular weight. The nanocarrier surface was estimated to become fully covered with antibody and/or enzyme, with no BSA found on the coat ($\leq 0.5\%$ of total coat molecules). The diameter and zeta potential of coated nanocarriers were measured via dynamic and phase analysis light scattering (Zetasizer nano-ZS90; Malvern Instruments; Westborough, MA).

The release of ^{125}I -enzyme from anti-ICAM/ ^{125}I -enzyme NCs was determined as described [47, 48] at 30 min, 1, 5, 8, 24, 48, and 72 hours after particle preparation by centrifugation to separate free enzyme from particle bound fraction and measured with a gamma counter. Release was assessed after 2 rounds of centrifugation at 13.8 g, resuspension

by pipetting, and sonication. Enzyme release was also tested during incubation in storage buffer (1% BSA-PBS), complete cell medium (described below), or fetal bovine serum (FBS), at 4 °C or 37 °C, pH 7.4 or pH 4.5, and in the absence or presence of α Gal substrate analog 2- μ g/ml N-Dodecanoyl-NBD-ceramide trihexoside (NBD-Gb3; Matreya, LLC, Pleasant Gap, PA) to mimic Fabry disease or GAA substrate 50 mg/mL glycogen to mimic Pompe disease.

3.4. Cell culture

Human primary cell lines were used for all cell culture experiments: human umbilical vein endothelial cells (HUVECs; Clonetics, San Diego, CA), human brain microvascular endothelial cells (HBMECs; Applied Cell Biology Research Institute, Kirkland, WA), human NHA astrocyte cells (ACs; Lonza Walkersville Inc., Walkersville, MD), and human brain vascular pericyte cells (PCs; Sciencell Research Laboratory, Carlsbad, CA). Human neuroblastoma subclone SH-SY5Y cells (NBCs; American Type Culture Collection, Manassas, VA) were cultured and differentiated into neuron-like cells for cell culture experiments. All cells were cultured in 37°C, 5% CO₂, and 95% humidity environment in respective supplemented medium. For microscopy experiments, mono-cultures of cells between passage 4 to 10 were seeded onto glass coverslips and cultured with 100 U/mL penicillin and 100 μ g/mL streptomycin in the following media: **HUVECs** were seeded onto 1% gelatin coated glass coverslips at a density of 7.5×10^4 cells/cm² and grown in M-199 basal medium supplemented with 15% FBS, 2 mM L-glutamine, 15 μ g/mL endothelial cell growth supplement, and 100 μ g/mL heparin; **HBMECs** were seeded onto 1% gelatin coated glass coverslips at a density of 7.5×10^4 cells/cm² and cultured in RPMI-1640 basal medium supplemented with 20% FBS, 2 mM L-glutamine, 30 μ g/mL endothelial cell growth

supplement, and 100 $\mu\text{g}/\text{mL}$ heparin; **ACs** were seeded onto 1% gelatin coated glass coverslips at a density of 5.0×10^4 cells/ cm^2 and cultured in DMEM basal medium supplemented with 15% fetal bovine serum (FBS), 50 $\mu\text{g}/\text{mL}$ gentamicin, and 2 mM L-glutamine; **PCs** were seeded onto poly-L-lysine coated glass coverslips at a density of 2.5×10^4 cells/ cm^2 and cultured in Pericyte media (ScienCell Research Laboratories, Carlsbad, CA) supplemented with 20% FBS and 15 $\mu\text{g}/\text{mL}$ pericyte growth factor; **NBCs** were first propagated then differentiated into neuron-like cells (**NLCs**). NBCs were seeded on 1% Matrigel (BD Biosciences, Franklin Lakes, NJ) coated flasks at a density of 5.0×10^3 cells/ cm^2 and propagated in RPMI-1640 basal medium supplemented with 10% FBS, 2 mM L-glutamine, and 1 mM sodium pyruvate. NBCs were passaged when cultures grew to be 60% confluent, no more than 10 times prior to differentiation. To differentiate NBCs into NLCs, NBCs were seeded onto 1% matrigel coated coverslips at a density of 7.5×10^3 cells/ cm^2 and cultured in DMEM supplemented with 5% FBS and 10 μM retinoic acid (without penicillin and streptomycin) for 5 days, then cultured in Neurobasal medium supplemented with B-27, 50 $\mu\text{g}/\text{mL}$ gentamicin, 2 mM GlutaMaxI, 2 mM dibutyryl-cyclic AMP, 20 mM potassium chloride, 50 ng/mL recombinant human brain-derived neurotrophic factor, 100 U/mL penicillin, and 100 $\mu\text{g}/\text{mL}$ streptomycin, as instructed [164, 165].

Skeletal muscle cells were isolated from C57BL/6 mouse gastrocnemius and quadriceps by digestion with 0.2 mg/mL collagenase in culture medium (described below) for 24 hours at 37°C. Muscle cells were then washed with DMEM, seeded on Matrigel coated glass coverslip, and cultured in DMEM supplemented with 2 mM L-glutamine, 100 U/mL penicillin, 100 $\mu\text{g}/\text{mL}$ streptomycin, and 10% FBS.

3.5. ICAM-1 expression

ICAM-1 expression on all cell types listed above was assessed by fluorescence microscopy. Cells seeded onto glass coverslips as aforementioned were treated with or without 10 ng/mL TNF α overnight, and then fixed with cold 2% paraformaldehyde for 15 minutes at room temperature. Fixed cells were then washed three times with 1 mL of PBS and then incubated with 55.5 pM anti-ICAM, or non-specific IgG as a control, in 1% BSA-PBS for 1 hour at room temperature, followed by incubation with 26.7 pM FITC- or Texas Red-labeled secondary goat-anti-mouse antibody for 30 minutes at room temperature. The nucleus was stained with 14.3 μ M blue 4',6-diamidino-2-phenylindole (DAPI). Fluorescence images were captured with SlideBook 4.2 software (Intelligent Imaging Innovations, Denver, CO) using Olympus IX81 microscope (Olympus, Inc., Center Valley, PA), ORCA-ER camera (Hamamatsu, Bridgewater, NJ), and a 40x objective (Olympus Uplan F LN; Olympus, Inc., Center Valley, PA) with a DAPI, FITC, and/or Texas Red filter (1160A-OMF, 3540B-OMF, 4040B-OMF; Semrock, Inc., Rochester, NY). Sum fluorescence intensity (A.U.) per cell and fluorescence intensity per area of each cell was analyzed in with the Image Pro 6.3 software (Media Cybernetics, Inc., Bethesda, MD) and normalized to the background fluorescence. Phase-contrast was used to delimit the cell borders.

3.6. Binding of ICAM-1-targeted nanocarriers to cells

Healthy or diseased (TNF α , TNF α and DGJ, or TNF α and turanose treated, as indicated below) cells were incubated with green Fluoresbrite IgG NCs, anti-ICAM NCs, or anti-ICAM/enzyme NCs (50:50 antibody to enzyme mass ratio; 6.8×10^{10} NCs/mL) at 37°C for 1, 3, or 5 hours. Cells were washed to remove unbound NCs, then fixed and the nucleus was

stained with 14.3 μM DAPI. Fluorescence microscopy was used to capture micrographs as described above with a 40x or 60x objective to estimate the total number of green fluorescent NCs associated per cell. This was achieved using a macro that normalizes the area of specific fluorescence (over a threshold background) to the number of pixels that theoretically correspond to the size of a single particle, viewed under the magnification used to image.

3.7. Endocytosis of ICAM-1-targeted nanocarriers into cells

Healthy or diseased cells were incubated with green Fluoresbrite labeled anti-ICAM NCs or anti-ICAM/enzyme NCs (50:50 antibody to enzyme mass ratio; 6.8×10^{10} NCs/mL) for 1, 3, or 5 hours continuously at 37°C, or for 30 minutes pulse then washed to remove unbound NCs followed by replacement of fresh medium for a total incubation time of 1 hour at 37°C. Cells were then washed to remove any unbound NCs, then fixed with paraformaldehyde. Surface bound NCs were counter stained with 26.7 pM Texas Red goat-anti-mouse secondary antibody. Since fixed cells were not permeabilized, the secondary antibody can only bind to anti-ICAM coat on nanocarriers located on cell surface and can not reach NCs that are endocytosed into the cell [40]. Nuclei were stained with 14.3 μM DAPI. Fluorescence microscopy was used to visualize cell samples and collect micrographs. In merged micrographs, green fluorescence alone revealed endocytosed NCs, yellow fluorescence (green + red) revealed surface bound NCs, and blue fluorescence (DAPI) located nuclei. From this, the total number of NCs endocytosed per cell could be estimated and compared to the total number of NCs associated per cell to extrapolate internalization efficiency as percent internalization.

The mechanism by which cells endocytose anti-ICAM NCs or anti-ICAM/enzyme NCs was studied by performing similar experiments in the presence of one of the following pharmacological inhibitors of endocytic transport: 3 mM amiloride (which inhibits CAM-pathway), 1 $\mu\text{g}/\text{mL}$ filipin (which inhibits caveolae-mediated pathways), or 50 μM monodansylcadaverine (MDC; which inhibits clathrin-mediated pathways) [40]. The effects of these inhibitors on the uptake of NCs was evaluated similarly as stated above, using fluorescence microscopy to calculate the internalization efficiency in each condition and compared to that of the control, incubation in absence of an inhibitor.

3.8. Lysosomal trafficking of ICAM-1-targeted nanocarriers in cells

Lysosomes were labeled by incubating cells with 100 μM Texas Red dextran (10 kDa) for 45 minutes at 37°C to allow for cellular uptake followed by removal of the medium containing this marker. Incubation was then continued with medium without this marker for a total of 1.5 hours at 37°C to ensure trafficking of internalized dextran to lysosome [166]. Since dextran is a polysaccharide that cannot be enzymatically degraded in mammalian cells, it therefore stably accumulates in lysosomes to permit their visualization [157]. Cells were then incubated with green Fluoresbrite anti-ICAM NCs or anti-ICAM/enzyme NCs (50:50 antibody to enzyme mass ratio; 6.8×10^{10} NCs/mL) for 1 hour at 37°C to allow for binding. Medium was then washed to remove unbound NCs, followed by replacement with fresh medium and additional incubation for 0, 2, or 4 hours at 37°C (total incubation time of 1, 3, or 5 hours) to synchronize transport of pre-bound NCs. Cells were then fixed and the nucleus stained with DAPI. The number of NCs that colocalized with Texas Red dextran-labeled lysosomes was semi-quantitatively measured using fluorescence microscopy. Green fluorescence alone revealed cell associated NCs that did not co-localize with lysosomes, red fluorescence alone

revealed lysosomes without NCs, and yellow fluorescence (green + red) revealed NCs localized to labeled lysosomes. From this the total number of NCs co-localized with lysosomes could be estimated for each cell and compared to the total number of NCs associated per cell in order to extrapolate lysosomal trafficking efficiency as percent NC co-localization in lysosomes.

3.9. Cell culture models of the blood-brain barrier

For experiments studying transport across the BBB, a monolayer of HBMECs was seeded at a density of 1.25×10^5 cells/cm² on 1 μ m porous membrane Transwell inserts (BD Falcon, Franklin Lakes, NJ) and grown for 7 days, exchanging medium every 2 days, to achieve confluence as recommended [167, 168]. To confirm integrity of the confluent monolayer, trans-endothelial electrical resistance (TEER) values were measured across the monolayer in initial experiments showing values consistent with published work, ~ 45 Ohms \cdot cm² on day 7, confirming our model [167, 168]. For co-culture BBB models, first ACs or PCs were seeded at a density of 5.0×10^3 cells/cm² on the basolateral side of the transwell membrane insert (inverted) for 3 hour at 37°C in respective culture media to develop the subendothelial BBB layer. Excess, unbound cells were then removed by aspirating remaining media and the transwell membrane inserts were flipped upright into 24-well plates. Then, HBMECs were seeded on top of the transwell membrane insert (apical side) to develop the endothelial BBB layer, while keeping the subendothelial BBB layer attached by addition of culture media in both apical and basolateral chambers [167]. These bi-layer BBB models were grown in HBMEC complete medium for 7 days, replacing the medium every 2 days. For experiments requiring diseased BBB models, cells were incubated with 10 ng/mL TNF α -supplemented complete medium overnight on day 6 for experimentation on day 7.

3.10. Transcytosis of ICAM-1-targeted carriers across BBB cell models

Endothelial (HBMECs) monolayers were cultured on transwell inserts with or without 10 ng/mL TNF α . 125 I-anti-ICAM NCs or non-specific 125 I-IgG NCs (6.8×10^{10} NCs/mL) were added to the apical chamber over HBMEC monolayers for 30 minutes at 37°C. Both apical and basolateral chambers were then washed to remove unbound NCs as well as NCs that may have leaked to the basolateral chamber. NCs that remained bound continued to be incubated for a total of 1 or 5 hours at 37°C to allow for potential transport. Incubations were conducted in control medium or in medium containing either 222 pM anti-ICAM to competitively bind ICAM-1 or 20 μ M 5-(N-ethyl-N-isopropyl)amiloride (EIPA; an amiloride derivative) to inhibit CAM-mediated transport. The endothelial layer on the transwell insert was collected to measure 125 I-anti-ICAM NC or 125 I-IgG NC content in the cell fraction, and the medium in the basolateral chamber was collected to estimate transported 125 I-anti-ICAM NC or 125 I-IgG NC fraction were quantified with a gamma counter. Free 125 I in each fraction was measured by TCA precipitation assay and subtracted from results to eliminate potential errors contributed by presence of free 125 I, which may result from degradation during binding, endocytosis, and/or transcellular transport. The total number of anti-ICAM NCs or IgG NCs associated to cells and transported across cells per area of the transwell membrane was estimated.

To study transport across bi-layered endothelial (HBMEC) and subendothelial (ACs or PCs) BBB cell models, cells were cultured with 10 ng/mL TNF α and incubated with 125 I-anti-ICAM NCs (6.8×10^{10} NCs/mL) for 1, 5, or 24 hours at 37°C. The endothelial and subendothelial layers were separately scraped and collected to measure 125 I-anti-ICAM NC content and estimate number of NCs in the cell fractions. The medium in the basolateral

chamber was also collected to estimate the transported ^{125}I -anti-ICAM NC fraction. As aforementioned, free ^{125}I was accounted for by TCA precipitation and subtracted from results. Similarly, the total number anti-ICAM NCs associated to cells and transported across cells per area of the transwell membrane was estimated. Additionally, visual confirmation of anti-ICAM NCs associated to the endothelial and subendothelial layers was performed using confocal fluorescence microscopy. Cells were fixed, nuclei stained with DAPI, and transwell membranes excised and mounted on microscopy slides. Green fluorescence showed presence of anti-ICAM NCs and blue fluorescence (DAPI) located nuclei.

3.11. Cell culture models for disease

To develop diseased cells mimicking pathological environments, cells were cultured with respective complete media supplemented with a cytokine that stimulates enhanced ICAM-1 expression, similar to pathological conditions. Specifically, cells were incubated with 10 ng/mL tumor necrosis factor α (TNF α) for 16 to 20 hours (overnight) at 37°C prior to experimentation.

To mimic deficiency in αGal encountered in Fabry disease (FD), HUVECs were incubated with 10 ng/mL TNF α , to mimic pathological stimulation, and also 500 μM deoxygalactonojirimycin hydrochloride (DGJ), to inhibit endogenous αGal , for 16 hours at 37°C. To visually verify intracellular globotriaosylceramide (Gb3), a substrate of αGal , cells were also incubated with a fluorescent analog for 16 hours: 2–10 $\mu\text{g}/\text{mL}$ NBD-Gb3. Gb3 accumulation was semi-quantitatively measured by microscopy by tracking the fluorescence intensity. Fluorescence images were captured with SlideBook 4.2 software (Intelligent Imaging Innovations, Denver, CO) using Olympus IX81 microscope (Olympus, Inc., Center

Valley, PA), ORCA-ER camera (Hamamatsu, Bridgewater, NJ) and a 40x objective (Olympus Uplan F LN; Olympus, Inc., Center Valley, PA) with a FITC filter (3540B-OMF; Semrock, Inc., Rochester, NY). Fluorescence intensity (A.U.) corresponding to stained Gb3 substrate in cells was analyzed in captured images with the Image Pro 6.3 software (Media Cybernetics, Inc., Bethesda, MD).

To model Pompe disease (PD) due to GAA deficiency, HUVECs were concurrently incubated with 10 ng/mL TNF α and a competitive inhibitor of GAA, 300 or 600 μ M D-(+)-turanose, overnight. Accumulation of the substrate of this enzyme, glycogen, was confirmed by staining fixed cells with periodic acid-Schiff (PAS) [169]. Glycogen accumulation was semi-quantitatively measured using microscopy by capturing bright-field micrographs with SlideBook 4.2 software using the Olympus microscope with a 40x objective and ORCA-ER camera stated above, with blue, green, and red filters (1160A-OMF, 3540B-OMF, 4040B-OMF; Semrock, Inc., Rochester, NY), composing colored pictures. The red stained glycogen was analyzed from these images with the Image-Pro 6.3 software.

3.12. Substrate degradation by ICAM-1-targeted carriers in cells

FD-model HUVECs loaded with green fluorescent NBD-Gb3 or PD-model HUVECs were incubated at 37°C for 5 hours with 6.8×10^{10} NCs/mL of respective anti-ICAM/enzyme NCs (50:50 antibody to enzyme mass ratio) or respective equivalent non-targeted enzyme (2.5 μ g/mL enzyme), in the presence of 300 μ M chloroquine. Chloroquine was used since removal of DGJ in FD-model cells or turanose in PD-model cells (required to avoid inhibition of the delivered α Gal or GAA) may render the endogenous enzyme active. Chloroquine neutralizes the pH in lysosomes and inhibits endogenous lysosomal enzymes,

which have acidic pKa values, without affecting the exogenous neutral α Gal or GAA. After incubation with enzyme or NCs, cells were fixed. Fluorescence microscopy was used to assess degradation of NBD-Gb3 in FD-model cells. For PD-model cells, fixed samples were stained with PAS, and analyzed by microscopy to quantify glycogen degradation. Micrographs were imaged to semi-quantitatively estimate substrate degradation as follows:

$$\% \text{ Substrate degradation} = 100 \times \left\{ 1 - \frac{(\text{substrate in disease model cells after treatment} - \text{substrate in control cells})}{(\text{substrate in disease model cells without treatment} - \text{substrate in control cells})} \right\}$$

3.13. Visualization of ICAM-1-targeted carriers in mice

Visualization of anti-ICAM/IgG or IgG NCs in vivo was assessed by evaluating the biodistribution of NC versus NC coat in mice through optical imaging. To trace NCs, green Fluoresbrite labeled NCs were used. To trace cargo coated onto NCs, IgG molecules were labeled with Near Infra-Red (NIR-IgG). Female NIH Swiss mice (Harlan; Indianapolis, IN) were anesthetized with isoflurane inhalant (2 to 2.5% in O₂) and intravenously (i.v.) injected with either non-specific IgG/NIR-IgG green Fluoresbrite-NCs or targeted anti-ICAM/NIR-IgG green Fluoresbrite-NCs. After 30 minutes, mice were euthanized and the abdominal and chest cavities opened for full body imaging using a Xenogen IVIS-200 system (Caliper Life Sciences; Hopkinton, MA). Additionally, organs (brain, heart, kidneys, liver, lungs, and spleen) were collected and separately imaged for semi-quantitative fluorescence intensity measurements to estimate the relative NC versus NC coat accumulation in each organ. Protocols used for these experiments followed IACUC humane care guidelines approved by University of Maryland Baltimore. Experiments were conducted in collaboration with Dr.

Scott Burks and Dr. Joseph Kao of the Department of Physiology and Center for Biomedical Engineering and Technology at University of Maryland Baltimore.

3.14. In vivo circulation and biodistribution of ICAM-1-targeted carriers in mice

NC circulation and biodistribution patterns in vivo were studied. C57BL/6 mice (Jackson Laboratory; Bar Harbor, ME) were anesthetized with an intraperitoneal injection (using a 28G hypodermic needle) of a 100 mg ketamine/10 mg xylazine/kg body weight buffered in 250 μ L PBS. Anesthetized mice were then injected with 1.6×10^{13} or 2.4×10^{13} NCs/ kg mice bodyweight of anti-ICAM/ 125 I-enzyme NCs (95:5 or 50:50 antibody to enzyme mass ratio) or equivalent 125 I-enzyme dose (1.7, 16.7, or 25 μ g/mice buffered with 0.3% BSA-PBS). Blood samples (100 μ L) were collected by retro-orbital bleeds at 1, 15, and 30 minutes post-injection. After 30 minutes or 24 hours, mice were euthanized by cervical dislocation under anesthesia and tissues (brain, heart, kidneys liver, lungs, spleen, left gastrocnemius muscle and quadriceps muscle) were collected either with or without previous perfusion with 50 mL of PBS to eliminate blood and circulating NC fraction. Tissues were weighed and measured for 125 I content using a gamma counter. The weight and 125 I content of each organ and blood sample were used to calculate the following parameters: the percentage of injected dose (%ID), the percentage of injected dose per gram of tissue to compare among organs of different size (%ID/g), the localization ratio to compare tissue-to-blood distribution (LR; %ID/g organ : %ID/g in blood), and the specificity index to compare targeted-to-non-targeted counterparts (SI; LR of anti-ICAM/enzyme NCs : LR of enzyme).

In addition, organs were crudely sectioned and imaged by confocal microscope Leica TCS SP5 X, using Leica Lite 2.0.2 Software (Leica Microsystems, Wetzlar, Germany) to calculate green Fluorescebrite NC retention. For all mice experiments performed at

University of Maryland College Park, IACUC protocols defining humane care guidelines were approved and strictly followed.

3.15. In vivo distribution of ICAM-1-targeted carriers in mouse brain

C57Bl/6 mice were i.v. injected with anti-ICAM/¹²⁵I-enzyme green Fluoresbrite NCs (50:50 antibody to enzyme mass ratio; 2.4×10^{13} NCs/kg mice bodyweight) and euthanized after 30 minutes. The brain was collected and crudely sectioned into 8 coronal slices. The weight and ¹²⁵I content of each section were measured in a gamma counter to estimate the comparative content of ¹²⁵I-enzyme present. Additionally, these sections were also imaged using Xenogen, and the fluorescence intensity measured to reveal the localization of accumulated NCs, as described in Section 3.13.

3.16. Statistics

In vitro enzyme release experiments were performed in triplicates per condition and with at least 2 repeats. In vitro cell culture experiments were performed in duplicates, with a sample size of ≥ 20 cells, and with at least 2 repeats (total $n \geq 54$ cells). In vivo experiments were performed with ≥ 3 mice per experiments. Data were calculated as mean \pm standard error of the mean (SEM). Statistical significance between two samples of equal variance was determined by Student's unpaired t-tests in which $p < 0.05$. Analysis of variance (ANOVA) with $\alpha = 0.05$ was used to determine statistical difference among three or more samples. If results showed statistical difference ($F > F_{\text{crit}}$), then student's unpaired t-tests were then performed between all possible sample comparisons.

SECTION 4: RESULTS AND DISCUSSION

4.1. Lysosomal enzyme delivery to cells by ICAM-1-targeted nanocarriers

4.1.1. Introduction

Fabry disease (FD) caused by deficient α -galactosidase A (α Gal) and Pompe disease (PD) caused by deficient α -glucosidase (GAA) are examples of LSDs for which ERT treatment is available. ERT for FD and PD involves i.v. administration of recombinant α Gal and GAA, respectively. These recombinant enzymes have M6P residues and can target M6PR on cells, rendering clathrin-mediated endocytosis and lysosomal trafficking [79-83]. However, M6PR is not overexpressed in disease sites and does not provide preferential enzyme delivery to these areas, leading to ineffective targeting to most affected cells, tissues, and organs [27-29, 34, 35, 84, 85]. Moreover, clathrin-mediated endocytosis associated to M6PR has been shown to be impaired in some LSDs, and therefore, cellular uptake of these recombinant enzymes results in suboptimal intracellular (lysosomal) delivery [27-29]. The lack of cellular targeting and effective endocytosis reduce the effectiveness of the therapy and render ERT suboptimal. Therefore, research for more optimal methods to deliver LSD treatment is still on-going.

In this thesis we investigate the potential to improve delivery of enzymes for LSDs by targeting them to ICAM-1 since this molecule is expressed on most cells and tissues that targets for intervention in these diseases, particularly those most severely altered by pathological conditions [39]. Targeting ICAM-1 triggers endocytosis via the non-clathrin non-caveolae CAM-mediated pathway [40], bypassing limited function of clathrin-mediated pathways in some LSDs [27-29]. The Muro lab had previously shown that ICAM-1-targeting nanocarriers carrying ASM (anti-ICAM/ASM NCs), for treatment of NPD, effectively bound to cells, and were endocytosed and trafficked to lysosomes, where excess lysosomal substrate

was attenuated as a result of the delivered enzyme [41, 42]. In vivo work showed that anti-ICAM/ASM NCs rapidly targeted and accumulated to organs with high ICAM-1 expression, specifically the lungs and liver [41, 42]. These results demonstrated that this strategy can be useful to treat NPD. However, whether these outcomes are unique to anti-ICAM/ASM NCs or whether this anti-ICAM NC platform can be translated to other LSDs was unknown. Since different LSDs pose different challenges and the corresponding lysosomal enzymes have different properties, the combination of anti-ICAM/enzyme NCs may yield varying results and each application must be separately tested. Hence, in this thesis, we evaluated the efficacy of using anti-ICAM NCs to deliver α Gal and GAA necessary for treatment of FD and PD, respectively, as an example of other ERTs.

4.1.2. Coating of enzyme onto ICAM-1-targeted nanocarriers

As a proof-of-concept, model ICAM-1-targeted nanocarriers were prepared by coating 100-nm diameter polystyrene nanocarriers via surface adsorption with both ICAM-1-targeting antibodies (anti-ICAM) and enzyme (either α Gal or GAA; 50:50 antibody to enzyme mass ratio). Placing anti-ICAM and enzyme on the surface allows binding of anti-ICAM to ICAM-1 and interaction of the lysosomal enzyme with its lysosomal substrate once internalized by cells, modeling a “pro-drug” formulation. Polystyrene nanocarriers were used as model nanocarriers (not intended for clinical use) since this polymer is non-degradable and particles can be traced while avoiding confounding results of degradation. In cell culture and laboratory animals, these ICAM-1-targeted polystyrene particles display similar targeting and intracellular transport mechanisms than biocompatible poly(lactic-co-glycolic acid) nanocarriers [41, 42], a material approved by the Food and Drug Administration for use in several devices [108], validating our model.

To validate presence of enzyme coat onto model anti-ICAM NCs, enzymes were labeled with ^{125}I (anti-ICAM/ ^{125}I - αGal NCs or anti-ICAM/ ^{125}I -GAA NCs). As shown in Table 1, at a 50:50 anti-ICAM to enzyme coating ratio, anti-ICAM/ αGal NC had a size of 223.2 ± 2.6 nm in diameter, with a PDI of 0.128 ± 0.008 , carrying ~ 138 anti-ICAM molecules/NC and ~ 530 αGal molecules/NC. Similarly, anti-ICAM/GAA NCs were 180.1 ± 0.9 nm in diameter, with a PDI of 0.232 ± 0.000 , carrying ~ 123 anti-ICAM molecules/NC and ~ 278 GAA molecules/NC. The number of total αGal molecules coated onto a NC is almost 2-folds greater than that of GAA (Table 1). This is most likely due to the size difference between the two enzymes (MW of αGal is ~ 32.3 kDa versus GAA is ~ 68.5 kDa). Interestingly, both nanocarrier preparations showed similar coating of anti-ICAM molecules per NCs (~ 130 molecules/NC), which is in agreement with that reported for anti-ICAM/ASM NCs prepared with the same method (~ 135 anti-ICAM molecules/NC) [41, 42, 47]. This is approximately half the amount of anti-ICAM molecules coated on NCs which contained only anti-ICAM (~ 220 molecules/NC; Table 1) [41, 42, 47]. This suggests that all three enzymes, regardless of size, presented similar steric hindrances that reduced the coating of the targeting moiety onto the nanocarrier comparably. This is in agreement with the fact that all three formulations were prepared with similar anti-ICAM to enzyme mass ratio. Hence, it is expected that NCs bearing these three different enzymes would bind similarly to cells (Table 1).

Table 1. Characterization of ICAM-1-targeted nanocarriers coated with lysosomal enzymes. (Table adapted from [47])

	Non-loaded	ASM	α Gal	GAA
Enzyme coating efficiency (%)	N/A	80	77	94
Enzyme molecule per NC (50:50 mass)	N/A	230	530	278
Anti-ICAM molecule per NC (50:50 mass)	222*	135	138	123
Size (nm in diameter)	283*		223	180
Polydispersity index (PDI)	0.18*		0.13	0.23
<hr/>				
Binding (NCs per cell)	165	160	70	80
% Internalization (1 hour)	80	70	67	80
% Lysosomal transport (3 hours)	75	70	70	65
% Lysosomal storage degradation (5 hours)	N/A	98	70	75
Enhanced degradation (anti-ICAM/enzyme NCs : free enzyme)	N/A	2	2.5	3

N/A = not applicable. * Non-loaded anti-ICAM NCs was coated 100% with anti-ICAM only. Data are mean values from [41, 42, 47, 48].

4.1.3. Enzyme release from ICAM-1-targeted nanocarriers

Since the model formulations carry both the targeting moiety and the enzyme cargo on the surface of nanocarriers, the stability of enzyme coating the formulation was first tested, which was assessed in various in vitro conditions. First, the enzyme coat was found to be stable under various physical stresses, including centrifugation, resuspension by pipetting, and sonication ($\leq 11.6 \pm 0.3\%$ enzyme release). Then, to mimic storage conditions, anti-ICAM/ ^{125}I - α Gal NCs were incubated in storage buffer (1% BSA-PBS) up to several days, periodically collecting samples to measure ^{125}I content to calculate enzyme release from the nanocarrier. ^{125}I - α Gal was stably retained on anti-ICAM NCs for up to 3 days when stored in this solution at 4°C ($2.4 \pm 4.8\%$ enzyme release at day 3; Figure 4a). In addition, storage at 37°C did not cause a significant release from nanocarriers by day 3 ($11.8 \pm 0.9\%$; Figure 4a).

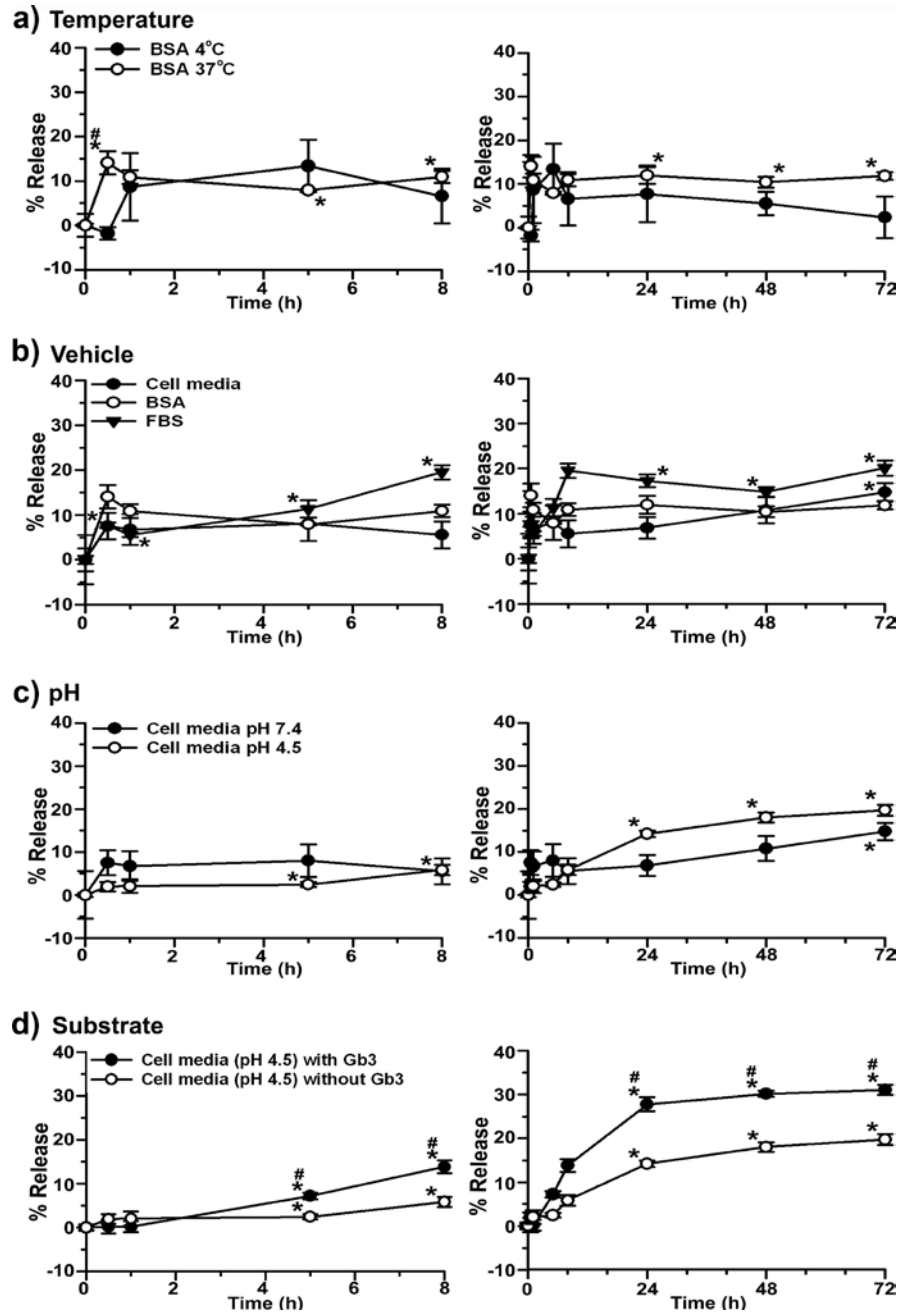


Figure 4. Release of α Gal from anti-ICAM/ α Gal nanocarriers. 125 I- α Gal released from anti-ICAM/ 125 I- α Gal NCs was separated from the particle-bound fraction by centrifugation after incubation for varying periods of time in (a) 1% BSA in PBS buffer at 4°C or 37°C; (b) 1% BSA in PBS, HUVEC medium, or FBS at 37°C and pH 7.4; (c) HUVEC medium at 37°C and either pH 7.4 or pH 4.5; and (d) HUVEC medium at 37°C and pH 4.5 in the absence or presence of NBD-Gb3. Data are mean \pm SEM, $n \geq 3$. * $p < 0.05$, compares each time point to time 0 within the same condition. # $p < 0.05$, compares (for each time point): (a) 4°C to 37°C, (b) HUVEC medium and FBS to BSA, (c) pH 4.5 to pH 7.4, and (d) Gb3 to non-Gb3; by Student's t-test. Statistical significance for time 0-8 hours is shown only in the left panel and time 0 to 72 hours only in the right panel. (Figure reproduced from [48])

Next, to evaluate enzyme release under physiological conditions, anti-ICAM/¹²⁵I- α Gal NCs were incubated at physiological temperature (37°C) with either complete cell medium, serum, acidic cell medium (mimicking lysosomal pH), or acid cell medium with substrate (mimicking lysosomal storage condition in LSD) for 3 days. Incubation of anti-ICAM/¹²⁵I- α Gal NCs in complete cell medium or serum (which mimic physiological fluids) still showed a marked retention of ¹²⁵I- α Gal on nanocarriers, with only 6.7 \pm 3.4% and 5.6 \pm 0.5% ¹²⁵I- α Gal release at 1 hour, and 8.0 \pm 3.8% and 11.3 \pm 1.9% release at 5 hour (Figure 4b). Enzyme release was significant after 3 days of incubation in cell medium (14.8 \pm 2.0%) and a comparable release was seen after 8 hours incubation in serum (19.5 \pm 1.6%). This suggests that although coating is relatively stable, α Gal can be released from nanocarriers after delivery in cell culture or animal models. Supporting this, release at 37°C of ¹²⁵I- α Gal from anti-ICAM NCs in cell medium was accelerated at pH 4.5, which mimics lysosomal pH (Figure 4c). At acidic pH, enzyme release was significant after only 5 hours incubation (2.5 \pm 0.5%) versus 3 days incubation at neutral pH (Figure 4c). The presence of substrate Gb3, which mimics the lysosomal environment in this disease, further enhanced ¹²⁵I- α Gal release (Figure 4d). Under this condition, release at 5 hours tripled that in the absence of substrate (7.2 \pm 0.7%) and reached a plateau (27.8 \pm 1.6%) by day 1 (Figure 4d).

In addition, anti-ICAM/¹²⁵I-GAA NCs showed similar characteristics (Figure 5). The enzyme coat was stable during storage at 4°C in saline buffer (0.0 \pm 0.1% to 6.1 \pm 0.5% enzyme release within 3 days; Figure 5a). Incubation of anti-ICAM/¹²⁵I-GAA NCs at 37°C and neutral pH in complete cell medium also showed marked enzyme retention: 3.8 \pm 0.2% release at 3 hours and 11.9 \pm 0.3% release at 72 hours (Figure 5a). Enzyme release was notably enhanced under conditions mimicking the lysosomal storage environment, pH 4.5 and presence of the enzyme substrate, glycogen: 3.1-, 7.9-, and 11.5-fold increased compared to neutral pH at 30 minutes, 3 hours, and 8 hours, respectively (Figure 5b).

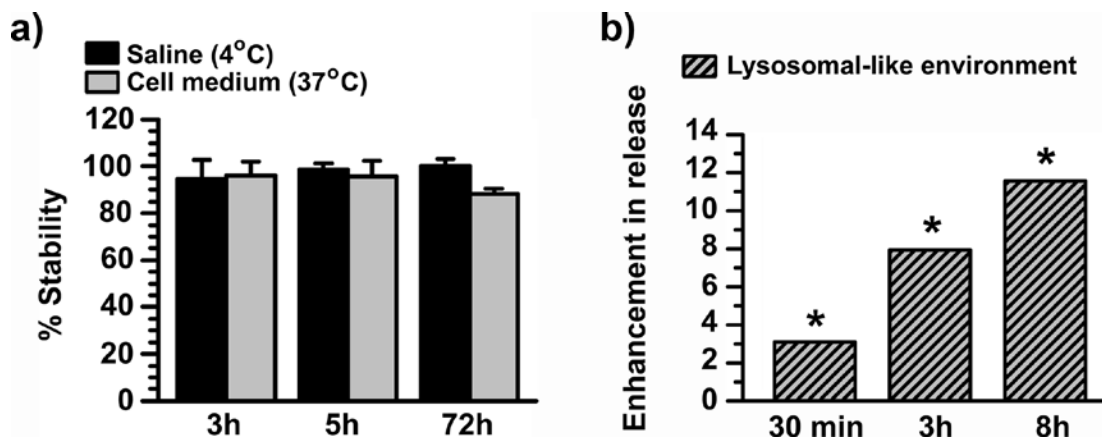


Figure 5. Release of GAA from anti-ICAM/GAA nanocarriers. (a) Anti-ICAM/¹²⁵I-GAA NCs were incubated in either storage buffer (1% BSA-PBS, pH 7.4) at 4°C or in a physiological-like fluid (cell medium supplemented with serum, pH 7.4) at 37°C. Samples were collected at the indicated time points to determine the release of ¹²⁵I-GAA from carrier particles after separation from ¹²⁵I-GAA stably bound to the nanocarrier coat by centrifugation. (b) Release of ¹²⁵I-GAA from anti-ICAM/¹²⁵I-GAA NCs at 37°C in a lysosomal-like environment (e.g., serum-supplemented cell medium, pH 4.5, presence of glycogen) was compared to that of similar counterparts incubated at neutral pH and in the absence of the enzyme substrate (fold increase is represented). Data are mean±SEM, n=6. *p<0.01, by Student's t-test (GAA release in lysosomal-like environment compared to GAA release in saline). (Figure reproduced from [47])

All in all, these results suggest that lysosomal enzymes can remain stably coated on nanocarrier particles under storage and exposure to physiological conditions. Additionally, the enzymes were conditionally released from the nanocarrier surface when in a lysosomal-like environment with the presence of their substrates (Figures 4 and 5).

4.1.4. Binding of anti-ICAM/enzyme nanocarriers to cells

Intravenously (i.v.) injected material will first encounter endothelial cells (ECs) of the vasculature as the first layer of cells that must be targeted in order to penetrate through and reach tissue in the parenchyma. Also, in many cases, including FD, targeting dysfunctional

ECs in the vacuature is a main goal of lysosomal ERT. Hence, in the following experiments, ECs were used to test the efficacy of anti-ICAM/enzyme NCs.

First, the binding efficiency of anti-ICAM NCs was tested using HUVECs pre-exposed to $TNF\alpha$, to mimic ICAM-1 expression in pathological-like conditions, or to control cells. After 30 minute incubation of anti-ICAM NCs with cells, fluorescence microscopy showed a 3.3-fold increase in binding of anti-ICAM NCs to ICAM-1 on $TNF\alpha$ treated cells (Figure 6a). This is in agreement with enhanced ICAM-1 expression induced by $TNF\alpha$

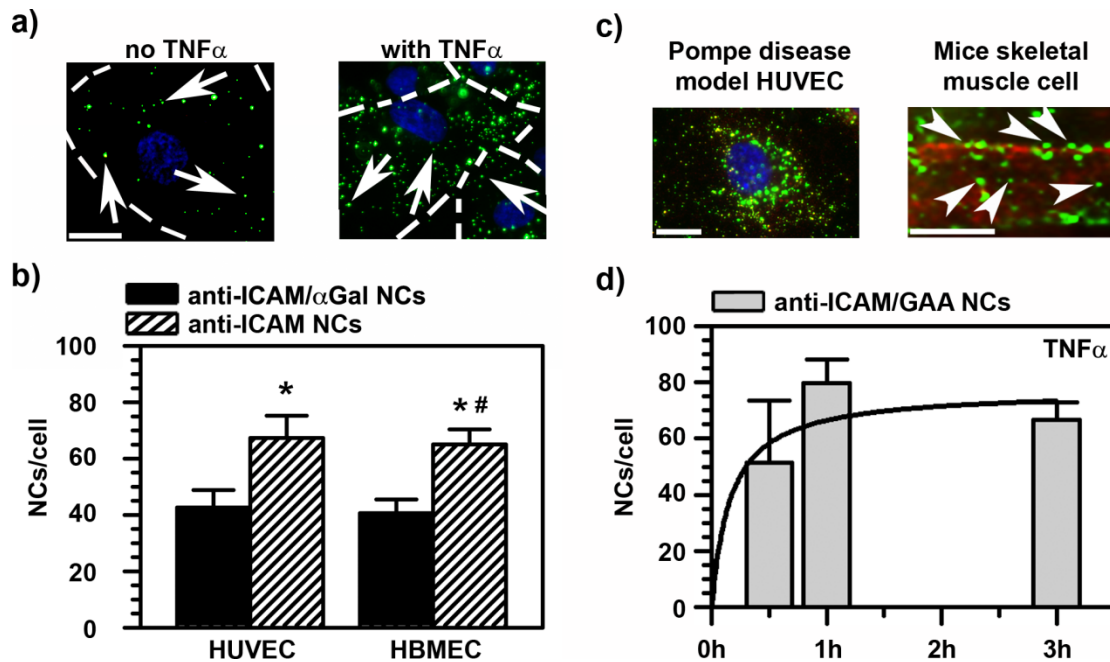


Figure 6. Binding of ICAM-1-targeting systems to endothelial cell models. (a) To confirm ICAM-1 expression on endothelial cell model, HUVECs were treated with or without $TNF\alpha$ and incubated with green fluorescent anti-ICAM NCs for 30 minutes at $4^{\circ}C$ to test binding. Scale bar = $10\ \mu m$. (b) To study the effects of loading an enzyme onto anti-ICAM NCs on binding, $TNF\alpha$ -treated macrovascular (HUVECs) and microvascular (HBMECs) models were incubated with either green fluorescent anti-ICAM NCs or anti-ICAM/ αGal NCs for 1 hour. (c) PD-model HUVECs and excised skeletal muscle from mice (see Section 3.4.) were incubated with green fluorescent anti-ICAM/GAA NCs. Arrowheads indicate NCs aligned along cytoskeletal fiber (pseudocolored red). Scale bar = $10\ \mu m$ for PD-model HUVEC; scale bar = $\sim 2\ \mu m$ for skeletal muscle cell. (d) Binding kinetics of green fluorescent anti-ICAM/GAA NCs to PD-model HUVECs at $37^{\circ}C$. Data are mean \pm SEM. * $p < 0.05$ comparing anti-ICAM/enzyme NCs to anti-ICAM NCs; # $p < 0.05$ comparing HUVEC to HBMEC. (Figure adapted from [47, 48])

activation, as expected. Then, in addition to evaluating ICAM-1 targeting on HUVECs, which models macrovascular ECs, HBMECs modeling microvascular ECs was assessed (Figure 6b), since both ECs are targets for FD. Similar to HUVECs, fluorescence microscopy showed that binding of anti-ICAM NCs increased 3.4-folds in TNF α stimulated HBMECs compared to control HBMECs, also indicative of enhanced ICAM-1 expression under this condition (data not shown). Even though statistical difference was detected, anti-ICAM NC binding profile to microvascular ECs was comparable to that of macrovascular ECs ($96.5 \pm 5.1\%$; Figure 6b) [48]. Therefore, in subsequent experiments, we used HUVECs as a representative model for evaluating EC response to incubation with anti-ICAM NC systems. Historical work with anti-ICAM/ASM NCs was performed using HUVECs, allowing comparative analysis between previous and subsequent studies on anti-ICAM/enzyme NCs.

As previously shown (Section 4.1.2.), the addition of these enzyme displaced the total number of anti-ICAM molecules on the surface of the NCs (Table 1), thereby potentially affecting the binding efficiency of anti-ICAM/enzyme NCs. This was confirmed experimentally: in both macrovascular and microvascular ECs, the addition of α Gal to anti-ICAM NCs did slightly alter binding efficiency, e.g. $63.3 \pm 9.1\%$ and $62.5 \pm 7.4\%$ of anti-ICAM NCs (Figure 6b). Yet, historical work using anti-ICAM/ASM NCs had showed that binding was not decreased as a result of replacing 50% of the targeting moiety on the NC surface with ASM (160 anti-ICAM/ASM NCs bound per cell versus 165 anti-ICAM NCs bound per cell; Table 1). Perhaps, ASM has affinity towards the membrane of cells, assisting in targeting, while α Gal did not. ASM hydrolyzes sphingomyelin, a sphingolipid present on the cell membrane, into phosphocholine head group and ceramide [170-173], which is found to be abundant at sites of ICAM-1-engagement on the cell membrane [174]. This could explain the lack of a decreased binding of anti-ICAM/ASM NCs to cells (Table 1). On the other hand, no relationship has been drawn, to our knowledge, between α Gal and ICAM-1-

engagement sites, even though globotriaosylceramide (Gb3), the substrate that α Gal hydrolyzes, is also found on the cell membrane [175]. Another reason for this difference could simply be due to different preparations and batches of antibody used, as well as different equipment used (microscope and camera).

Nonetheless, significant amount of anti-ICAM/enzyme NCs did bind to stimulated ECs, and compared to non-loaded anti-ICAM NCs, which was enhanced in TNF α vs control ECs: 40.7 ± 4.8 anti-ICAM/ α Gal NCs/cell in TNF α versus 19.2 ± 3.2 anti-ICAM NCs/cell in control HBMEC, a 2.1-fold difference. Moreover, binding of anti-ICAM/ α Gal NCs to FD-model HUVECs which exhibit excess Gb3 storage (see Methods, Section 3.11.) as compared to only TNF α stimulated HUVECs increased binding even more (76.7 ± 7.5 NCs/cell versus 42.7 ± 6.1 NCs/cell, respectively), suggesting that ICAM-1 expression heightens on cells under conditions of lysosomal storage, and, thus, this targeting strategy is valuable for such an application.

With regard to anti-ICAM/GAA NCs, these NCs bound to PD-model HUVECs which exhibit excess glycogen storage (see Methods, Section 3.11.) also with good efficacy: 51.3 ± 22.0 anti-ICAM/GAA NCs bound per cell after 30 minutes, comparable to anti-ICAM/ α Gal NC binding within the same time frame (42.7 ± 6.1 NCs/cell, Figure 6d). Binding of anti-ICAM/GAA NCs increased with time and quickly saturated (79.8 ± 8.3 NCs/cell by 1 hour and 66.5 ± 6.4 NCs/cell by 3 hours), with a $t_{1/2}$ of 9.7 minutes and a B_{max} of ~ 77 NCs/cell (Figure 6d). Similarly, by 1 h, 76.7 ± 7.5 anti-ICAM/ α Gal NCs bound per FD-model HUVEC (data not shown). Also, as a proof-of-model experiment, anti-ICAM/GAA NCs was capable of binding to excised muscle fibers extracted from mice gastrocnemius and quadriceps (Figure 6c). This set of results suggests that anti-ICAM/enzyme NCs can carry different enzymes and still achieve significant binding to different types of cells and under different

disease conditions, yet the binding efficiency may slightly differ depending on the precise anti-ICAM/enzyme NC formulation, which emphasizes the need to study each application separately.

4.1.5. Endocytosis of anti-ICAM/enzyme nanocarriers by cells

We next examined endocytosis of anti-ICAM NCs, which is a requirement for lysosomal transport of these enzymes. Using fluorescence microscopy, we studied the internalization efficiency of anti-ICAM/enzyme NCs into control, TNF α -stimulated, and LSD-disease model HUVECs (Figure 7). Cells were incubated with green fluorescent anti-ICAM/enzyme NCs for 30 minutes, 1, 3, or 5 hours, non-bound NCs were removed and cells were then fixed. To distinguish surface bound versus internalized NCs, surface bound NCs were counter-stained with TexasRed secondary IgG to bind to anti-ICAM on the NC coat (green + red = yellow). Since the cells were not permeabilized prior to staining, internalized NCs are only visualized in the green channel [40].

Since FD particularly affects vascular ECs (among others), we first compared internalization efficiency in microvascular ECs (HBMECs) versus macrovascular ECs (HUVECs). Internalization of anti-ICAM NCs after 30 minutes was 76.4 \pm 2.8% into HBMECs versus 88.1 \pm 1.7% in HUVECs (Figure 7a), demonstrating a similar uptake efficiency in both cell types. Then, since addition of enzyme cargo to anti-ICAM NCs displaces 50% of the targeting moiety on NC surface, we evaluated whether internalization would be affected in anti-ICAM/enzyme NCs. Contrary to the decreased binding efficiency observed in Figure 6b, the addition of an enzyme (α Gal) on the anti-ICAM NC did not affect the internalization efficiency into either macrovascular or microvascular ECs: e.g. 74.6.1 \pm 3.4% versus 84.4 \pm 2.5%, respectively (Figure 7a). This suggests that binding

efficiency does not affect internalization efficiency. Internalization of every individual carrier is an independent event, which has been previously observed for this system [40].

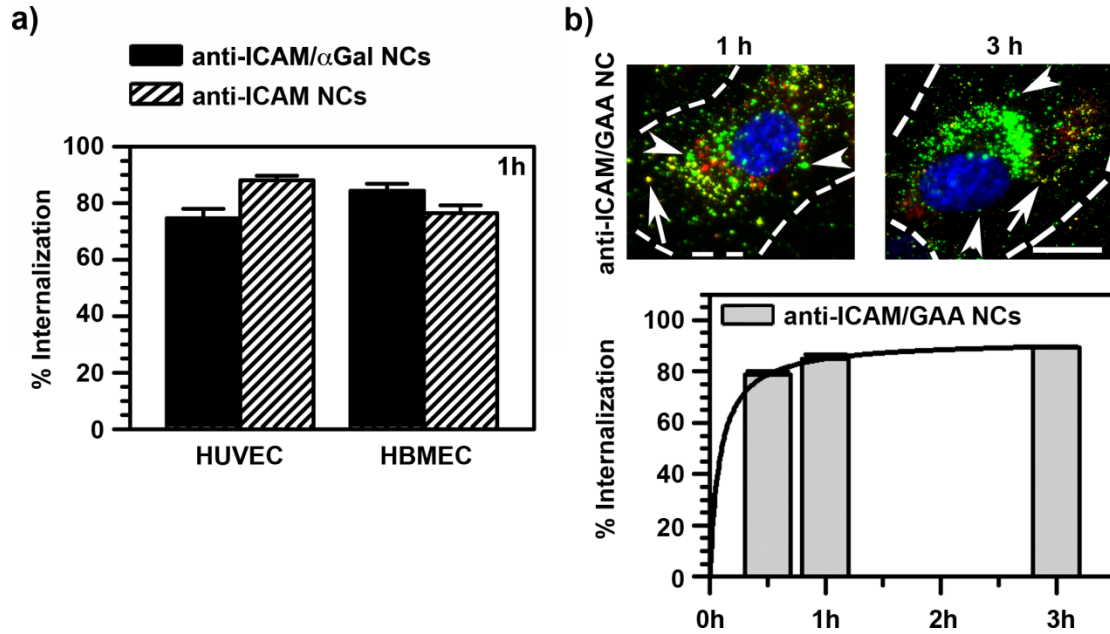


Figure 7. Uptake of anti-ICAM/enzyme nanocarriers by cells. (a) Green fluorescent anti-ICAM NCs or anti-ICAM/ α Gal NCs were incubated with TNF α -treated HUVECs or HBMECs for 1 hour at 37°C, to study whether internalization efficiency is affected by enzyme addition onto anti-ICAM NCs or whether this uptake differs in these 2 cell types. (b) Green fluorescent anti-ICAM/GAA NCs were incubated at 37°C with PD-model HUVECs for 30 min, 1 hour, or 3 hours to study the rate of internalization. Surface bound NCs were counterstained with Texas-Red secondary antibody (green + red = yellow). Arrowheads point to internalized NCs (green); arrows point to surface bound NCs (yellow). Percent internalization was calculated based on fluorescence microscopy results. Scale bar = 10 μ m. Data are mean \pm SEM. (Figure adapted from [47, 48])

Furthermore, internalization of anti-ICAM/ α Gal NCs was comparable to that of anti-ICAM/GAA NC (Figure 7). After 30 minutes, 74.6 \pm 3.4% of anti-ICAM/ α Gal NCs bound to TNF α -treated cells were endocytosed (not shown) compared to anti-ICAM/GAA NCs (78.6 \pm 1.7% internalization, Figure 7b). This is also comparable to the uptake previously observed for anti-ICAM/ASM NCs (~70%; Table 1), and implies that even with lysosomal storage, internalization of anti-ICAM/enzyme NCs is still efficient and comparable to cells

without storage. Indeed, endocytosis of anti-ICAM/GAA NCs quickly plateaus by 1 hour: 85.06±1.7% internalization (Table 1) compared to 89.4±0.4% internalization by 3 hours, with a rapid $t_{1/2}$ of 5.1 minutes and an I_{\max} of 92.0% internalization (Figure 7b).

4.1.6. Mechanism of endocytosis of anti-ICAM/enzyme nanocarriers

Clathrin-mediated and caveolae-mediated endocytosis are known as the classical pathways of endocytosis commonly used for vesicular endocytosis as a result of ligand-receptor binding in most cell types of the body [176, 177]. In fact, current ERT for LSDs, including FD and PD, capitalize on M6PR-binding of lysosomal enzymes, which relies on clathrin-mediated uptake [82, 83]. However, as mentioned (see Background, Section 2.3.), clathrin-mediated endocytosis is often impaired in LSDs [27-29, 51]. Endocytosis of ICAM-1-targeted NCs has previously been elucidated to be mediated via the CAM-pathway, independent of the classical endocytic pathways that rely on clathrin- or caveolae-mediation [40]. However, the enzyme load may alter this because these lysosomal enzymes may co-induce the clathrin pathway. Hence, we studied the possible endocytic route elicited by anti-ICAM/ α Gal NC and anti-ICAM/GAA NCs (Figure 8).

To inhibit CAM-mediated endocytosis cells were treated with amiloride, while to inhibit clathrin-mediated endocytosis cells were treated with MDC (see Methods, Section 3.7.). Only amiloride inhibited significantly endocytosis for both anti-ICAM/ α Gal NCs and anti-ICAM/GAA NCs (54.8±2.8% and 67.9±1.9% internalization compared to control, respectively; Figure 8). MDC did not inhibit internalization (95.5±3.2% and 101.1±1.2% of control, respectively), suggesting that endocytosis of anti-ICAM/enzyme NCs occurred via the CAM-pathway as oppose to clathrin-coated pits (Figure 8). Hence, ICAM-1-targeting

strategy may prove to be beneficial in assisting enzyme delivery via this non-classical route. This is especially important since clathrin-mediated endocytosis is impaired in several LSDs [27-29, 51].

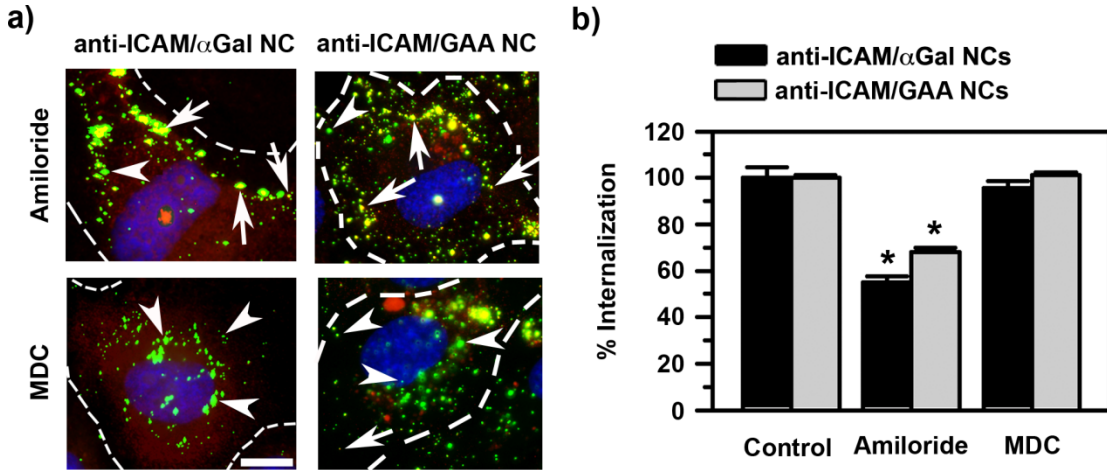


Figure 8. CAM-mediated endocytosis of anti-ICAM/enzyme nanocarriers. Green fluorescent anti-ICAM/ α Gal NCs or anti-ICAM/GAA NCs were incubated with TNF α -stimulated HUVECs, treated or not with inhibitors of CAM-mediated endocytosis (Amiloride) or clathrin-mediated endocytosis (MDC) for 1 hour at 37°C. Surface bound NCs were counterstained with Texas-Red secondary antibody (green + red = yellow). (a) Arrowheads point to internalized NCs (green); arrows point to surface bound NCs (yellow). Scale bar = 10 μ m. (b) Percent internalization was calculated based on fluorescence microscopy results. Data are mean \pm SEM. * p <0.01, comparing % internalization in inhibitor treated cells to control cells, by Student's t-test. (Figure adapted from [47, 48])

As expected, all three formulations tested thus far (anti-ICAM/ASM NCs, anti-ICAM/ α Gal NCs, anti-ICAM/GAA NCs) capitalize on CAM-mediation as the dominant endocytic route [42, 47, 48]. Interestingly, anti-ICAM/ASM NCs was shown to be inhibited by amiloride (~55% internalization compared to control) but enhanced by MDC (~20% increased internalization relative to control) [42]. This could indicate that anti-ICAM/ASM NCs may bind to both ICAM-1 and M6PR, but with M6PR being inefficient this may compete against CAM-uptake. By inhibiting clathrin, anti-ICAM/ASM NCs possibly were more readily internalized via ICAM-1. This would be in agreement with the fact that anti-

ICAM/ASM NCs did not suffer a reduction in binding versus anti-ICAM NCs (Table 1). Yet, this phenomenon was not exhibited in the other two ICAM-1-targeting systems. Since the lab has found that ASM plays a role in CAM-mediated endocytosis, this may explain this difference [161, 174]. To our knowledge, neither α Gal nor GAA have a role in CAM-mediated endocytosis. This different result suggests that different enzymes affect anti-ICAM NC properties differently.

4.1.7. Lysosomal trafficking of anti-ICAM/enzyme nanocarriers

Lysosomal delivery is the main goal for LSD treatment, e.g. ERT currently available aims to target recombinant enzymes to lysosomes by using M6PR-mediated transport [82, 83]. Previous work has shown that CAM-mediated endocytosis results in anti-ICAM NCs being transported to this location as well [40]. In fact, anti-ICAM/ASM NCs were shown to traffic to lysosomes within 3 hours, with similar efficiency as non-loaded anti-ICAM NCs [42]. Because different enzymes could elicit or add different properties that may affect lysosomal trafficking of anti-ICAM NC system, here, we study whether anti-ICAM/ α Gal NCs and anti-ICAM/GAA NCs trafficked similarly to lysosomes. We assessed this by labeling lysosomes with TexasRed dextran, as previously described [40], and following the anti-ICAM/enzyme NCs over time via fluorescence microscopy (Figure 9).

Results show that by 3 hours, majority of endocytosed anti-ICAM/ α Gal NCs were trafficked to the lysosome in TNF α -stimulated HUVECs ($27.4\pm 3.4\%$, $73.5\pm 2.1\%$, and $73.3\pm 2.3\%$ localization within lysosomes at 1, 3, and 5 hours; Figure 7a). Interestingly, a

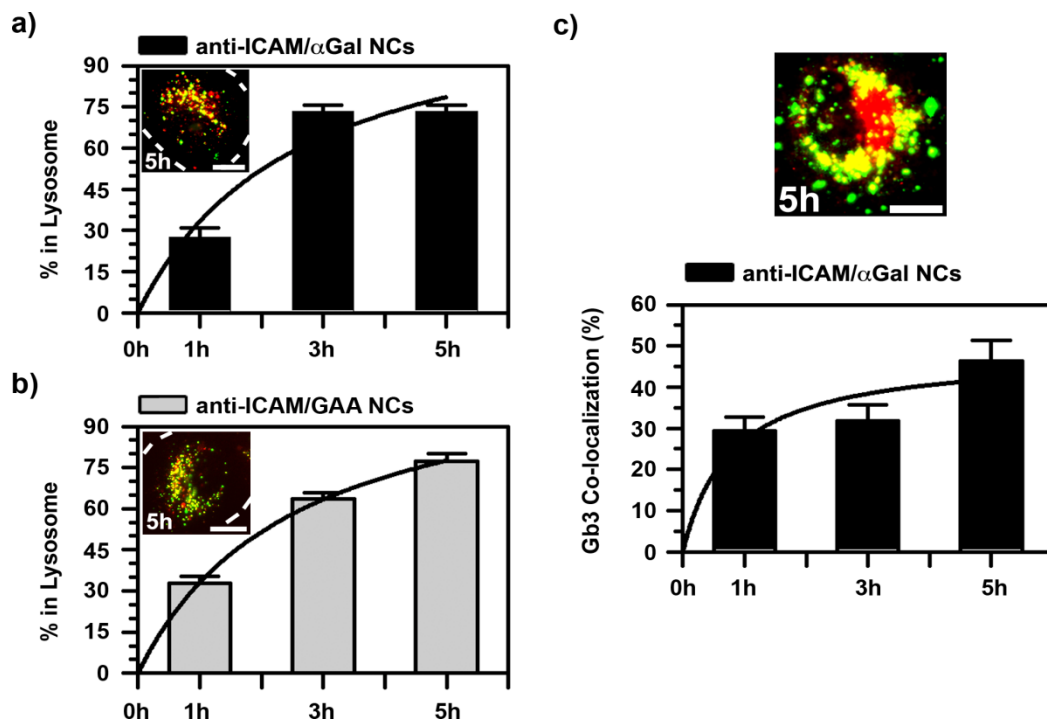


Figure 9. Intracellular trafficking of anti-ICAM/enzyme nanocarriers in diseased HUVECs. (a) TNF α -stimulated HUVECs or (b, c) LSD-model HUVECs were pre-treated with (a, b) Texas-Red dextran to label lysosomes (red) or (c) NBD-Gb3 (pseudo-colored here as red), to visualize Gb3 substrate accumulation. Cells were then incubated with green fluorescent anti-ICAM/enzyme NCs for 1 hour, washed to remove non-bound NCs, and then examined (1 hour) or incubated with media for an additional 2 or 4 hours (for a total time of 3 or 5 hours). Fluorescence microscopy determined percent of NCs which trafficked to (a, b) lysosomes or (c) regions of concentrated Gb3, shown in micrographs as yellow (red + green). Scale = 10 μ m. Data are mean \pm SEM. (Figure adapted from [47, 48])

similar intracellular trafficking profile was exhibited by anti-ICAM/GAA NCs in PD-model HUVECs: 32.8 \pm 2.5%, 63.6 \pm 2.2%, and 77.3 \pm 2.8% of NCs localized within lysosomes at 1, 3, and 5 hours, respectively (Figure 9b). Both trafficking profiles yielded a $t_{1/2}$ of \sim 2.5 hours, indicating no difference in the lysosomal transport potential regardless of the enzyme loaded or of the disease model. Previous work with anti-ICAM/ASM NCs showed this consistent trend as well: \sim 70% localization with lysosomes by 3 hours in TNF α -stimulated HUVECs (Table 1). Non-loaded anti-ICAM NCs localized to lysosomes at a slightly higher efficiency: \sim 75% by 3 hours (Table 1). Compared to anti-ICAM/enzyme NCs targeting LSD-model cells

a slight 5 to 10% difference observed could be due to the additional enzyme cargo on anti-ICAM NCs, potentially affecting lysosomal trafficking efficiency of the nanocarrier systems.

In LSD treatment, delivery of enzyme to lysosomes directly positions the enzyme at the site at which to degrade the accumulated substrate. As shown above, anti-ICAM/enzyme NCs are capable of trafficking to lysosomes. Additionally, we found that, endocytosed anti-ICAM/ α Gal NCs trafficked to areas of Gb3 substrate accumulation in FD-model HUVECs, as required in order to degrade Gb3 (Figure 9c). Specifically, $29.3\pm 3.4\%$, $31.8\pm 3.8\%$, and $46.4\pm 5.0\%$ of anti-ICAM/ α Gal NCs localized to Gb3 positive compartments at 1, 3, and 5 hours, respectively, with a $t_{1/2}$ of ~ 47 minutes. This set of results suggests that lysosomal delivery is possible, positioning the enzyme precisely at the location where it is needed.

4.1.8. Alleviation of excess lysosomal storage by anti-ICAM/enzyme nanocarriers

Delivery of active enzymes to lysosomes is the ultimate goal for LSD treatment. To assess functionality of the enzymes delivered via anti-ICAM NC, we examined the ability of these enzymes to degrade the accumulated substrate (Figure 10). For this purpose, in addition to TNF α -stimulation, disease EC models exhibiting respective substrate accumulation (Gb3 or glycogen) traceable via fluorescence analysis or PAS assay, respectively, were developed to mimic FD and PD pathology (see Methods, Section 3.11.). Since the exogenous enzymes we used here are active under neutral environments (versus the endogenous lysosomal enzymes, which are active under acidic environments) cells were also treated with chloroquine. This compound neutralizes the pH of lysosomal compartments, allowing the delivered enzyme to degrade the induced lysosomal substrate while inhibiting degradation by the endogenous enzymes. Using this model, the effectiveness of delivered α Gal and GAA were assessed.

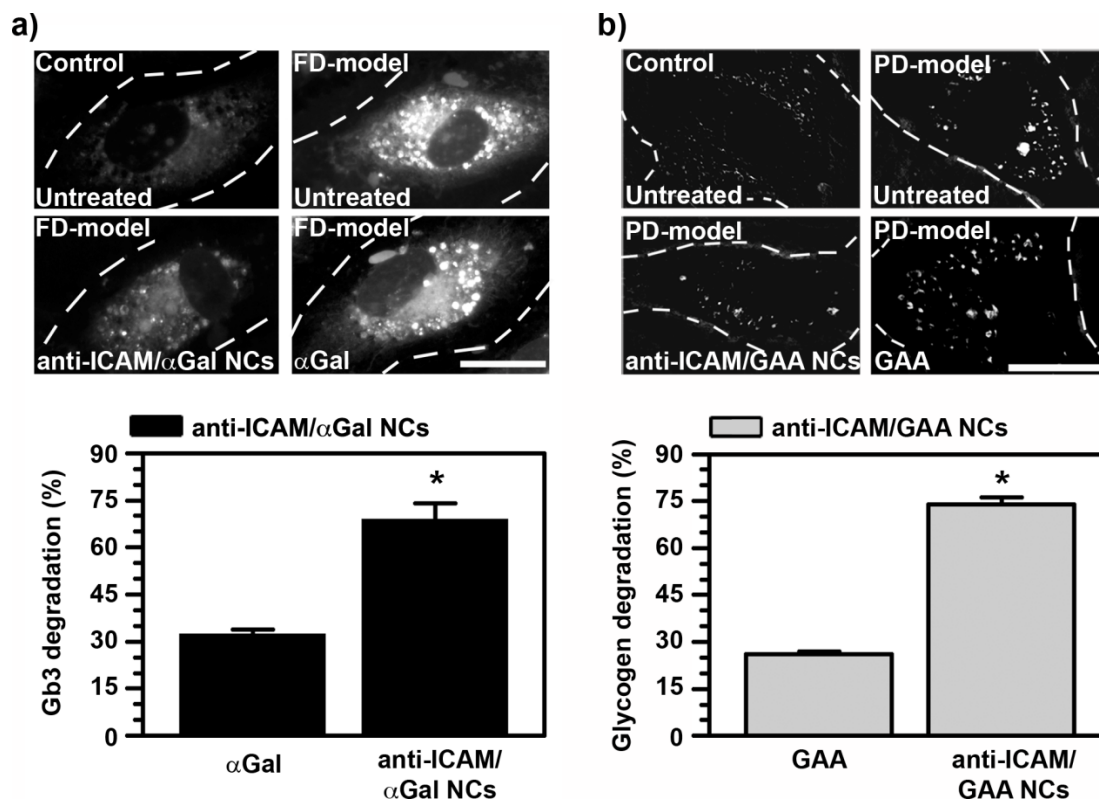


Figure 10. Degradation of lysosomal substrate by anti-ICAM/enzyme nanocarriers. TNF α -stimulated HUVECs were treated with either (a) DGJ and Gb3 to develop a traceable FD model or (b) turanose to develop a PD model. Cells were then incubated with non-fluorescence anti-ICAM/enzyme NCs for 5 hours in the presence of chloroquine. Through (a) fluorescence microscopy or (b) PAS assay, percent degradation of substrate was analyzed and calculated by comparing either cells treated with enzyme or anti-ICAM/enzyme NCs to untreated disease-model cells and control “healthy” cells (see Methods, Section 3.12.). Data are mean \pm SEM. * p <0.01, comparing anti-ICAM/enzyme NCs to non-targeted enzyme, by Student’s t-test. Scale = 10 μ m. (Figure adapted from [47, 48])

As shown in Figure 10, by 5 hours, excess Gb3 in FD-model HUVECs was reduced by $68.9\pm 5.0\%$ when incubated with anti-ICAM/ α Gal NCs, which represents a 2.1-folds enhancement in efficiency versus non-targeted α Gal (Table 1, Figure 10a). Similarly, anti-ICAM/GAA NCs reduced excess glycogen in PD-model HUVECs by $73.9\pm 2.3\%$, 2.8-folds more efficient than non-targeted GAA (Table 1, Figure 10b). These results suggest that anti-ICAM NCs deliver active α Gal and GAA to lysosomes. Previous work showed that ASM

delivered by anti-ICAM NCs remained similarly active as well [42, 158]. In fact, anti-ICAM/ASM NCs reduced accumulated sphingomyelin in ASM-deficient cells (fibroblast cells from NPD patients) by 98%, a 2-fold enhancement over the free enzyme (Table 1) [42]. Whereas 70–75% substrate reduction was observed for α -Gal and GAA, ASM delivered by anti-ICAM NCs reduced substrate levels to control values, which may be a result of experimental differences: an acidic enzyme (ASM) was tested in genetic models [42, 158] versus neutral α Gal and GAA tested in pharmacological models. In any instance, the enzymes delivered by anti-ICAM NCs improved substrate reduction by 2- to 3-folds compared to non-targeted counterparts (Table 1). These differences may be more acute in vivo, where binding of non-targeted enzymes may be further hindered as a result of blood flow.

4.1.9. Conclusion

Current ERT for LSDs fail to deliver enzyme therapeutic to lysosomes in cells due to poor binding and endocytosis. Targeting ICAM-1 can potentially amend this. Since FD affects all vascular ECs, we first confirmed that the binding and internalization pattern of anti-ICAM NCs in microvascular ECs (HBMECs) was similarly efficient in macrovascular (HUVECs), the model in which comparative historic work was performed. We then validated our cell culture model by confirming that binding is in fact enhanced on stimulated diseased cells. Interestingly, binding efficiency of anti-ICAM NCs to our LSD-model HUVECs exhibiting lysosomal storage conditions was in fact enhanced compared to stimulated HUVECs.

Previous work with anti-ICAM/ASM NCs showed promise in delivering ASM to diseased cells to attenuate accumulated lysosomal storage in cell culture models and to NPD target organs in mice [41, 157]. To study whether this anti-ICAM NC platform can be extended to other LSDs, we studied here the delivery of α Gal and GAA or treatment of FD

and PD, respectively. Interestingly, we noted that the addition of α Gal or GAA to the nanocarrier surface, which resulted in a 50% reduction in anti-ICAM coating density, did slightly decrease binding efficiency, contrary to previous work with ASM that showed that binding efficiency was conserved [42]. Nonetheless, binding was still very significant and the internalization efficiency was not affected. In fact, anti-ICAM/ α Gal NCs, anti-ICAM/GAA NCs, and anti-ICAM/ASM NCs all were efficiently internalized by cells via CAM-mediated endocytosis. This is important since ICAM-1-targeting provides a means to bypass clathrin-mediated endocytosis, a route that is currently utilized in ERT and reported to be impaired in some LSDs, affecting ERT treatment [27-29]. By targeting ICAM-1, anti-ICAM/enzyme NCs were also capable of efficiently delivering the enzyme cargo to lysosomes, the intended destination of these enzyme treatments. In all three formulations (anti-ICAM/ASM NCs, anti-ICAM/ α Gal NCs, and anti-ICAM/GAA NCs) the delivered enzyme was capable of degrading $\geq 70\%$ of aberrant storage, 2- to 3-folds more efficiently than non-targeted enzyme counterparts, suggesting that anti-ICAM NCs can enhance delivery of active lysosomal enzymes for treatment of NPD, FD, and PD. Hence, these similarities suggest that previous results seen with anti-ICAM/ASM NCs were not unique to NPD treatment model. In fact, it seems that ICAM-1-targeting platform can be used to similarly enhance binding, uptake, lysosomal trafficking, and substrate degradation of lysosomal enzymes, as evaluated here with α Gal and GAA.

4.2. Targeting of cells of the blood-brain barrier and the brain by ICAM-1-targeted nanocarriers

4.2.1. Introduction

To treat neuropathy and/or neurodegeneration associated to many LSDs, recombinant lysosomal enzymes must be delivered to glial and neurons inflicted by disease of the central nervous system (CNS) [16]. Yet brain delivery remains notoriously difficult because of the blood-brain barrier (BBB), an almost impermeable cell lining that distinctly separates circulating blood and brain tissue, and regulates transport and brain homeostasis to protect the CNS [17, 18]. Structurally, the BBB is made up of endothelial cells (ECs) that lack fenestrations [178] and form a tight cell layer directly in contact with the microcirculation, and by an adjacent subendothelial layer consisting of periendothelial cells that are in direct

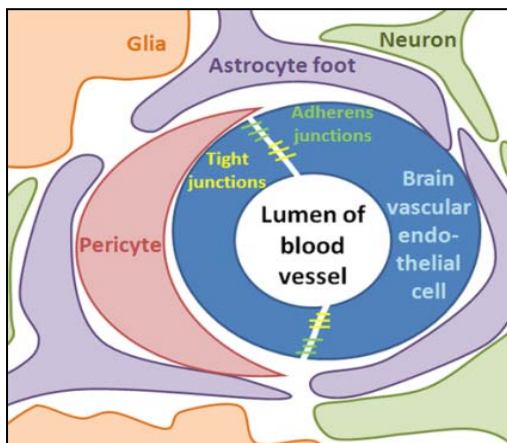


Figure 11. Cross section schematic of the blood-brain barrier and the surrounding brain tissue (glial cells and neurons).

contact with neuronal tissue (Figure 11) [17, 18]. The most abundant periendothelial cells are pericytes (PCs) and astrocytes (ACs) [179]. Together, brain microvascular ECs, immune and structural regulative ACs [180], and contractile PCs that help regulate blood flow [181] contribute to the nature of the BBB, which is nearly impermeable to passive transport of substances [17, 18].

Delivery of therapeutics to the brain circumventing the BBB has been attempted, such as direct injection into this tissue (e.g. intraparenchymal, intracerebral) or the cerebrospinal fluid (e.g. intrathecal, intracerebroventricular) [10]. Although somewhat effective in short-term studies when applied chronically to NPD models [182-185], these

methods are invasive and fail to provide the systemic relief necessary for LSDs. Systemic delivery is preferred and, hence, there is a need for strategies to traverse the BBB from the circulation.

Transport across the BBB rarely takes place via paracellular transport that opens cell-cell junctions, which can render leakage and disrupt homeostasis [186]. Rather, transport occurs more commonly via the transcellular route, requiring either transporter proteins for small molecules or vesicular transcytosis assisting transport of larger molecules [132]. Drug delivery strategies have attempted to capitalize on this natural phenomenon by targeting endothelial receptors to induce such vesicular transport, including insulin, low density lipoprotein, and transferrin receptors [187]. However, routing via these receptors requires mediation by clathrin-coated pits, which is impaired in some LSDs [27-29]. Therefore, an alternative transcytosis route is coveted to treat LSDs. Previous work in the Muro lab has shown that ICAM-1 can be targeted to assist transcytosis of nanocarriers across epithelial models [43]. However, whether this is possible for the BBB was unknown.

To explore if delivery of recombinant lysosomal enzymes to the brain could be achieved, bypassing clathrin-mediated transport across the BBB, in this section we first examined the capacity of ICAM-1-targeted systems to target cells of the BBB and brain. In particular, we focused on human brain microvascular ECs, ACs, PCs, and neuron-like cells (NLCs).

4.2.2. Expression of ICAM-1 on cells of the blood-brain barrier

To evaluate basal and disease-induced ICAM-1 expression levels on cells of the BBB, ECs, ACs, and PCs were cultured in the absence versus presence of $\text{TNF}\alpha$, which mimics healthy

or pathology-like stimulation (Figure 12), respectively. Previous works have reported ICAM-1 expression on healthy and activated brain cells [188], so this represents a confirmation for our experimental set-up.

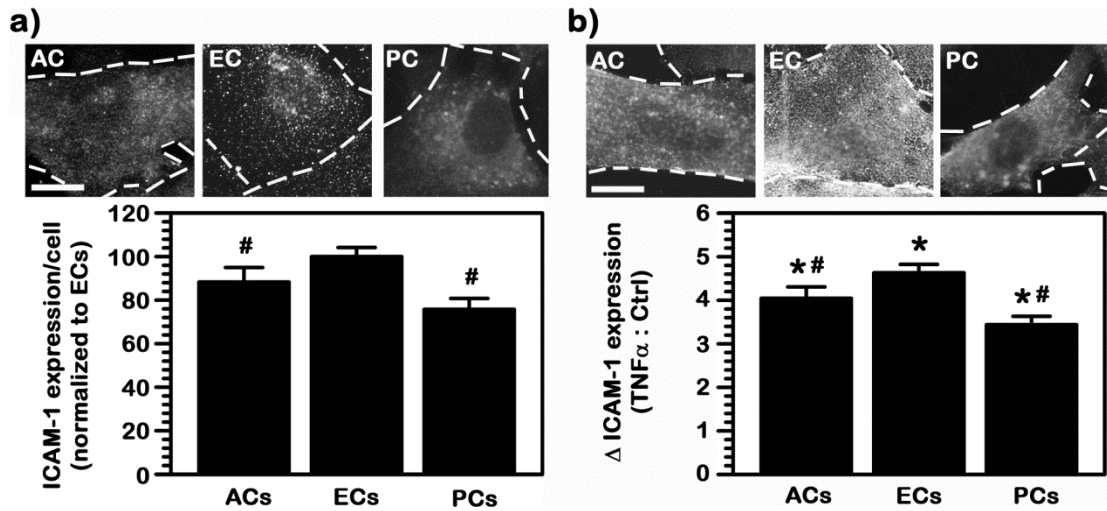


Figure 12. ICAM-1 expression on cells of the blood-brain barrier. Cells were cultured with or without TNF α , then fixed and stained for ICAM-1 using immunofluorescence. ICAM-1 expression was then measured by fluorescence microscopy. (a) ICAM-1 expression for control astrocytes (ACs) and pericytes (PCs) was normalized to control human brain microvascular endothelial cells (ECs). (b) Fold increase of ICAM-1 expression (Δ) on pathological-stimulated (TNF α treated) ACs, PCs, and ECs versus healthy control cells. Scale bar = 10 μ m. Data are mean \pm SEM. Statistical difference observed by ANOVA. # p <0.05, comparing ACs or PCs to ECs for each respective condition; * p <0.05, comparing TNF α to control for each cell type, by Student's t-test. (Figure reproduced from [49])

Using immunofluorescence, we observed that although all three cell types had fairly low detectable level of expression under control conditions (3- to 5-fold over background fluorescence), ECs had the highest ICAM-1 expression of the three cell types, with ACs and PCs expressing 88.3% and 75.8% of endothelial ICAM-1, respectively (Figure 12a). Once exposed to TNF α , ICAM-1 expression increased significantly for all three cell types: expression on ECs was enhanced the most with a 4.6-fold increase versus healthy conditions. ICAM-1 expression enhancement between diseased and healthy conditions for ACs and PCs was slightly lower but still significant: 4.0-fold and 3.4-fold enhancement, respectively

(Figure 12b). We observed a higher ICAM-1 expression level and higher increase as a result of TNF α -stimulation in ECs (Figure 12), as expected, since these cells make up the endothelial layer of the BBB with an active role in adhesion and transportation of leukocytes [189]. Also, recent studies imply that ACs play an important role in leukocyte recruitment to the brain through production of chemoattractant and pro-inflammatory factors, thereby regulating both resident and recruited immune cells [180]. Therefore, as expected, ACs also express ICAM-1 (Figure 12), as previously shown [190]. As per PCs, previously it was deemed that these cells have a less prominent role in leukocyte recruitment and more of a role in BBB structural support [191], which correlates well with our results showing the least ICAM-1 expression (Figure 12). This may be influenced also by the fact that similar to ACs placed in the subendothelial lining of the BBB structure, PCs are not subjected to blood flow, and therefore express less ICAM-1. This experiment demonstrates that ICAM-1 is expressed on all cells of the BBB, particularly under pathological stimulation, with higher expression on ECs, necessary for targeting from the blood stream, as intended.

4.2.3. Binding of ICAM-1-targeted nanocarriers to cells of the blood-brain barrier

We then tested the potential specificity and efficiency of ICAM-1-targeting nanocarriers to bind cells of the BBB (Figure 13). Green fluorescent NCs were coated with anti-ICAM to prepare anti-ICAM NCs as described in the Methods section (Section 3.3.). This yielded a coat of 222 \pm 8 antibodies/NC, and a resultant size of 283 \pm 4 nm diameter, with a PDI of 0.18 \pm 0.01 and a ζ -potential of -33 \pm 3 mV. Similarly, as a control, non-specific IgG NCs were prepared by coating green fluorescent NCs with non-specific IgG, which yielded a coat of 170 \pm 8 antibodies/NC, and a resultant size of 288 \pm 8 nm in diameter, with a PDI 0.18 \pm 0.02 and ζ -potential -27 \pm 5 mV, comparable to anti-ICAM NCs.

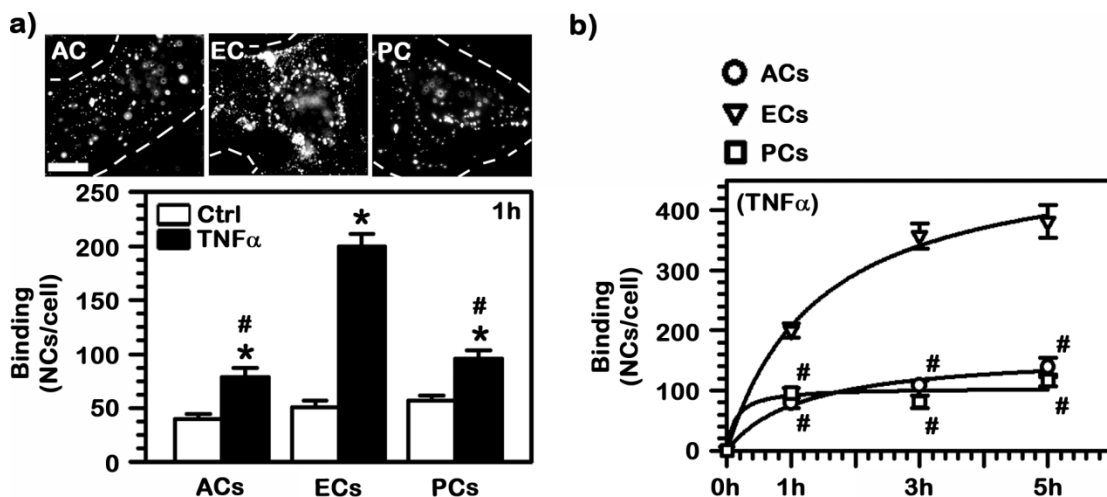


Figure 13. Binding of anti-ICAM nanocarriers to cells of the blood-brain barrier. (a) Anti-ICAM NCs were incubated with control or TNF α -activated BBB cells for 1 hour at 37°C. Scale bar = 10 μ m. (b) Stimulated cells were continuously incubated with anti-ICAM NCs for 1, 3, or 5 hours. Data were fitted to non-linear regression curves, all with $r^2 > 0.92$. Data are mean \pm SEM. Statistical difference observed by ANOVA. # $p < 0.05$, comparing ACs or PCs to ECs of each respective condition; * $p < 0.05$, comparing TNF α to control cells for each cell type, by Student's *t*-test. (Figure reproduced from [49])

In agreement with its positive expression on ECs, ACs, and PCs, binding of anti-ICAM NCs to these three cell types was significant as compared to control non-specific IgG NCs (1 hour, 37°C): ~40 to 57 anti-ICAM NCs/cell (Figure 13a) versus ~3 IgG NCs/cell (not shown) in control conditions. This demonstrates specificity of binding of anti-ICAM NCs to ICAM-1.

Also in agreement with ICAM-1 overexpression in pathologically conditions [38], binding of anti-ICAM NCs was enhanced in all three cell types upon TNF α -stimulation, with the greatest increase observed for ECs (3.9-fold enhancement), followed by ACs (2.0-fold) and PCs (1.7-fold). Hence, the absolute binding was considerably greater for ECs (199.9 \pm 11.6 NCs/cell), followed by PCs (95.4 \pm 8.4 NCs/cell; 48% of ECs) and ACs (79.0 \pm 8.0 NCs/cell; 39% of ECs). In general, this result correlates with the pattern of ICAM-1 presence on these cells. However, some differences were observed. As an example, for ECs the level

of overexpression of ICAM-1 by TNF α was similar to the enhancement in anti-ICAM NC targeting (4.6-fold and 3.9-fold, respectively). However, for subendothelial cells the increase in nanocarrier targeting in disease over control cells was lower than the change in ICAM-1 expression observed for these conditions (2- to 4-fold difference in binding versus 3- to 5-fold difference in expression; Figures 12 and 13). Hence, it seems that not all surface ICAM-1 overexpressed during pathology is available for targeting on subendothelial cells. Nanocarrier binding is likely to depend on the receptor location, interaction with other molecular partners, etc. (apart from other factors) [24, 160], explaining this result. This could be due to the multi-valent binding of anti-ICAM NCs, as oppose to individual antibody targeting that was used to detect expression. For instance, while PCs expressed the lowest ICAM-1 levels under control conditions, they afforded levels of anti-ICAM NC targeting greater than ACs and to the same extent as ECs. These examples illustrate that the relationship between target presence and its functional “targetability” is not always straightforward and may also vary from one cell type to another. This is often underappreciated and makes success of targeting strategies somewhat unpredictable.

However, with time, saturation of binding of anti-ICAM NCs correlated to the ICAM-1 expression initially observed. For instance, ECs accumulated the most anti-ICAM NCs of the three BBB cells types tested with 199.9 ± 11.6 NCs/cell in diseased cells and 50.9 ± 6.2 NCs/cell in control cells (Figure 13b), as predicted since it yielded the most ICAM-1 expression. Additionally, binding of anti-ICAM NCs to ECs increased with time and even by 5 hours (with 381.4 ± 26.9 anti-ICAM NCs/cell) the calculated binding saturation had not yet been reached ($t_{1/2}$ of ~ 85.6 minutes, B_{\max} of 503.6 ± 35.9 anti-ICAM NCs/cell; Figure 13c).

Interestingly, while both ICAM-1 expression and its increase due to disease was lowest for PCs, out of all BBB cells tested, these cells accumulated slightly more anti-ICAM

NCs under healthy conditions compared to ECs or ACs: 56.9 ± 4.4 NCs/cell in control cells. However, under disease conditions, PCs only accumulated half of NCs as compared to ECs: 95.4 ± 8.4 NCs/cell 1 hour. By 5 hours of incubation, binding to diseased PCs had not increased much more: 116.7 ± 9.9 NCs/cell (Figure 13c).

ACs accumulated the least amount of NCs initially with 39.9 ± 4.5 NCs/cell in control cells and 79.0 ± 8.0 NCs/cell in diseased cells by 1 hour. However, this amount doubled by 5 hours: 138.5 ± 15.7 NCs/cell, surpassing PCs (Figure 13b, c). Kinetic studies showed a $t_{1/2}$ of ~ 70.5 minutes to ACs versus ~ 8.3 minutes for PCs, yielding binding saturation indicative of the relationship between ICAM-1 expression and anti-ICAM NC binding: B_{\max} of 163.8 ± 17.4 anti-ICAM NCs/cell for ACs versus 104.4 ± 19.4 anti-ICAM NCs/cell for PCs. Therefore, binding of anti-ICAM NCs increased with enhanced ICAM-1 expression and offers preferential selectivity toward diseased versus control cells.

4.2.4. Internalization of ICAM-1-targeted nanocarriers by cells of the blood-brain barrier

In addition to binding, endocytosis is important as it represents a key step towards transport across the BBB. Also, its efficiency could be impacted by the observed binding rate. Using immunofluorescence, the total number of anti-ICAM NCs endocytosed by these cells was determined (Figure 14a). In agreement with the fact that more anti-ICAM NCs bound to diseased ECs as compared to ACs and PCs, more were endocytosed into these cell over time: 109.5 ± 4.2 , 202.1 ± 6.2 , and 221.8 ± 7.9 anti-ICAM NCs/cell by 1, 3, and 5 hours (Figure 14b). Similar to their binding pattern, the saturation point for uptake by ECs was not achieved by 5 hours: $t_{1/2}$ of ~ 99.9 minutes, B_{\max} of 302.1 ± 19.8 anti-ICAM NCs/cell. For ACs, anti-ICAM NCs were internalized at a slightly slower rate: 42.2 ± 1.0 , 58.7 ± 1.6 , and 78.7 ± 2.4 anti-ICAM

NCs/cell by 1, 3, and 5 hours, resulting in a $t_{1/2}$ of ~ 87.4 minutes and a B_{max} of 96.6 ± 14.2 anti-ICAM NCs/cell. Interestingly, even though the binding rate was rapid for PCs ($t_{1/2}$ of ~ 8.3 minutes), the internalization rate in these cells was much slower and similar to that of ACs, with only a slightly faster rate and lower saturation limit: 43.1 ± 1.7 , 49.5 ± 1.2 , and 76.9 ± 2.7 anti-ICAM NCs/cell by 1, 3, and 5 hours; $t_{1/2}$ of ~ 76.9 minutes, B_{max} of 87.2 ± 0.9 anti-ICAM NCs/cell.

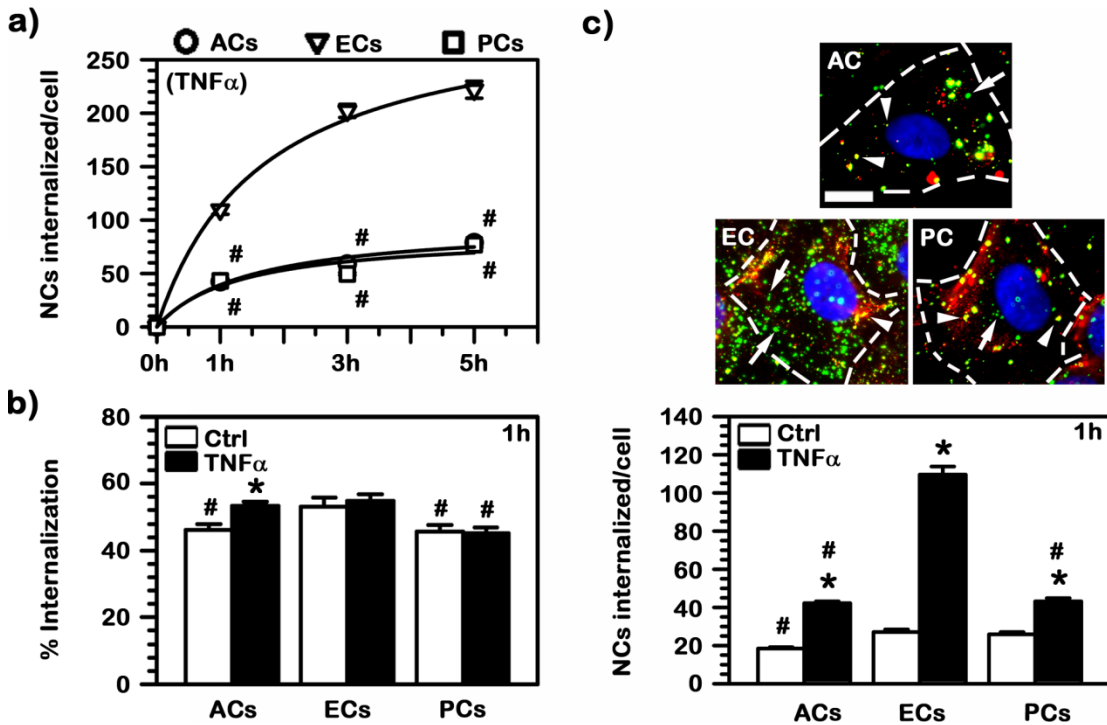


Figure 14. Internalization of anti-ICAM nanocarriers into cells of the blood-brain barrier. Control or TNF α -stimulated cells were incubated with green fluorescent anti-ICAM NCs for 1, 3, or 5 hours at 37°C. Non-bound NCs were then washed, surface bound anti-ICAM NCs were stained with Texas Red secondary antibody (red), and the nucleus was labeled with DAPI (blue). Fluorescent images were captured and analyzed by microscopy. (a) Kinetics of anti-ICAM NC uptake by TNF α -stimulated cells over a 5 hour period. Data were fitted to non-linear regression curves, all with $r^2 > 0.92$. (b) Percent of anti-ICAM NCs internalized by cells from the total cell-associated amount and (c) absolute number of anti-ICAM NCs internalized per cell under control or TNF α -stimulated conditions (1 hour). Micrographs depict TNF α -stimulated cells at 1 hour. Green (arrows) depicts internalized anti-ICAM NCs, yellow (arrowheads) points to anti-ICAM NCs on the surface of the cell (red + green = yellow). Scale bar = 10 μ m. Data are mean \pm SEM. Statistical difference observed by ANOVA. # $p < 0.05$, comparing ACs or PCs to ECs under each condition; * $p < 0.05$, comparing TNF α to control cells for each cell type, by Student's t-test. (Figure reproduced from [49])

To determine the efficiency of endocytosis, the percentage of anti-ICAM NCs internalized by the cell from the total cell-association fraction was calculated. Interestingly, this was similar between diseased and healthy cells: $46.2 \pm 1.8\%$ in healthy versus $53.4 \pm 1.3\%$ in diseased ACs, $53.2 \pm 2.7\%$ in healthy versus $54.8 \pm 2.1\%$ in diseased ECs, and $45.5 \pm 2.0\%$ in healthy versus $45.2 \pm 1.8\%$ in diseased PCs (1 hour; Figure 14b). Only ACs exhibit significant difference between healthy and disease condition, which could be a reflection of their role in recruiting immune cell to the brain [180]. Yet, the absolute increase of the number of anti-ICAM NCs endocytosed per cell showed significant differences between diseased and healthy cells, 2.2-fold in ACs, 4.1-fold in ECs, 1.7-fold in PCs (Figure 14c). Again, this verifies selectivity of anti-ICAM NCs to bind and internalize into diseased cells. Interestingly, this suggests that induction of endocytosis via the ICAM-1 pathway does not depend on the diseased state of the cell nor the number of nanocarriers able to target the cell surface, and rather endocytosis of each bound carrier is an independent event, as observed by ECs in the previous chapter. This is in agreement with previous observations on this pathway obtained in other cell types [162], which may warrant transport without the need to surpass a certain targeting threshold. Because of this phenomenon, the absolute level of internalization of anti-ICAM NCs was ruled by the absolute level of binding on cells. As a consequence, subendothelial cells internalized lower absolute levels of anti-ICAM NCs as compared to ECs, which was particularly evident under disease conditions (about half the EC level).

4.2.5. Mechanism of endocytosis of ICAM-1-targeted nanocarriers into cells of the blood-brain barrier

ICAM-1-targeting nanocarriers showed mechanism of endocytosis to be independent of clathrin-mediation [40], providing a potential alternative for ERT enhancement. As

mentioned in the previous section, this mechanism was conserved with anti-ICAM NCs bearing different lysosomal enzymes (Section 4.1.6.) [47, 48]. Since cells of the BBB are more restrictive in terms of transport, we tested whether the mechanism operates in human brain microvascular ECs, ACs, and PCs (Figure 15).

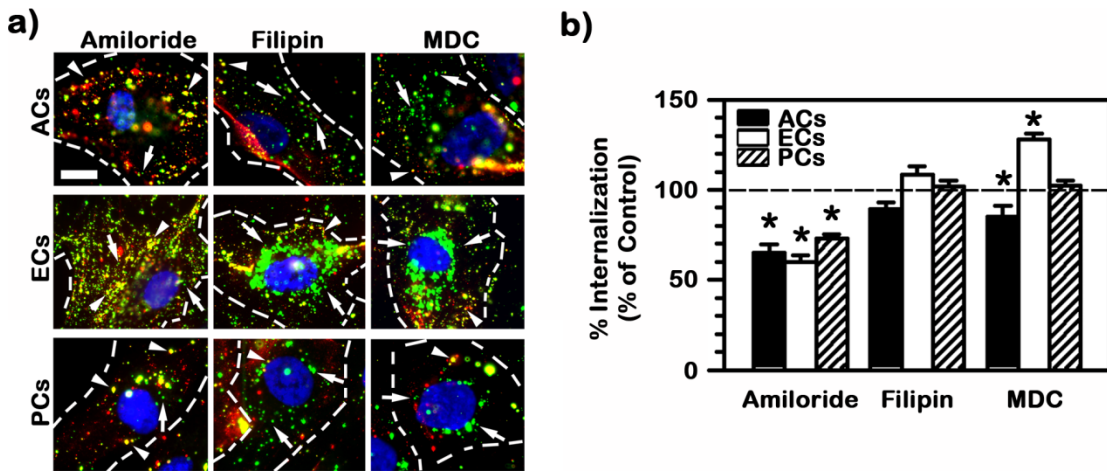


Figure 15. Endocytosis mechanism of anti-ICAM nanocarrier uptake into cells of the blood-brain barrier. TNF α -activated cells were incubated with anti-ICAM NCs for 3 hours at 37°C in absence (control) or in presence of either amiloride (CAM-mediated endocytosis inhibitor), filipin (caveolae-mediated endocytosis inhibitor), or MDC (clathrin-mediated endocytosis inhibitor). Cells were washed to remove non-bound NCs and stained with Texas Red secondary antibody. The nucleus was stained with DAPI. (a) Arrows point to internalized anti-ICAM NCs (green). Arrowheads point to surface bound anti-ICAM NCs (red + green = yellow). Scale bar = 10 μ m. (b) Percent of internalization relative to control cells. Data are mean \pm SEM. * p <0.05, comparing ACs or PCs to HBMECs of respective conditions, by Student's t-test. (Figure reproduced from [49])

When cells were incubated with amiloride, the pharmacological agent known to inhibit CAM-mediated endocytosis, internalization of anti-ICAM NCs was significantly reduced by 35.1 \pm 4.7% in ACs, 40.0 \pm 3.7% in ECs, and 27.3 \pm 2.7% in PCs. Endocytosis in cells treated with filipin, which inhibits caveolae-mediated endocytosis, was not significantly reduced, as expected. Interestingly, while endocytosis in cells treated with MDC, which inhibits clathrin-mediated endocytosis, was not affected in PCs (102.4 \pm 2.8% of control), this was increased for ECs (28.0 \pm 3.3% increase) and slightly reduced in ACs (14.9 \pm 5.9%

reduction; Figure 15). Interestingly, CAM-mediated transport of anti-ICAM NCs by BBB cells seemed influenced by the clathrin pathway, where inhibition of this pathway enhanced transport of anti- ICAM NCs by ECs while it decreased it in ACs. This may be related to the function of the cellular components of the BBB. For instance, while ECs from most other origins display a diversity of pathways (clathrin-, caveolae-, phagocytosis-like, etc. [177, 192]), yet endocytic transport in brain microvascular ECs seems restricted to the clathrin route [132, 187, 193]. Because of this, it is possible that common endocytic machinery (e.g., dynamin, cytoskeletal elements, motor proteins, SNARES, etc.) is “sequestered” by the clathrin pathway and not fully available for other endocytic routing. Inhibition of clathrin-mediated transport may “free” such common elements, allowing enhancement of the CAM pathway in brain ECs. In contrast, ACs regularly display additional endocytic routes (caveolae-mediated, phagocytic, etc. [194, 195]) and such an effect would not be expected. Since ACs actively mobilize several toll-like and scavenger-like receptors associated to the clathrin route [194, 195], it is possible that a small fraction of anti-ICAM NCs are not being specifically internalized by the CAM pathway but their antibody component may interact with these other clathrin-associated receptors. Although ECs may also express these other receptors [177], it is possible that this route is avoided since activated ECs express higher levels of ICAM-1 compared to activated ACs. Indeed, anti-ICAM NCs bound at a much greater extent on activated ECs versus ACs.

In summary, this set of results shows that binding and internalization rate of anti-ICAM NCs into all three BBB cell types vary depending on the cell phenotype. The endothelial layer of the BBB binds and internalizes anti-ICAM NCs faster and to a great absolute extent than ACs or PCs, which represents the subendothelial layer of the BBB. ECs are directly in contact with blood and therefore more capable of accessing anti-ICAM NCs that would be systemically administered. Additionally, it is more important for ECs to bind

anti-ICAM NCs more readily, as these cells regulate vesicular transport across the BBB via transcytosis. Hence, high traffic of anti-ICAM NCs into ECs could potentially equate to more transport across the BBB. Indeed, the subsequent subendothelial layer does not internalize anti-ICAM NCs as efficiently as brain ECs. With less “entrapment” of anti-ICAM NCs in these cells, there is more potential for anti-ICAM NCs to penetrate further into the brain parenchyma.

4.2.6. Lysosomal trafficking of ICAM-1-targeted nanocarriers in cells of the blood-brain barrier

To treat brain tissue plagued by LSD, delivery of lysosomal enzyme across the BBB is required. However, since all cells are affected by LSD pathology, delivery of lysosomal enzyme to lysosomes of all cells is desirable, even cells that make up cell barriers. Hence, through fluorescence microscopy, we evaluated whether cells of the BBB could efficiently traffic endocytosed anti-ICAM NCs to their respective lysosomes (Figure 16). Lysosomes were labeled with Texas-Red dextran (a 10 kDa polysaccharide that cannot be enzymatically degraded in mammalian cells) and anti-ICAM NCs with green fluorescence were used to allow for fluorescence tracing. After 1 hour incubation of anti-ICAM NCs with cells, cells were washed to remove non-bound excess anti-ICAM NCs and continued to be incubated for a total of 1, 3, or 5 hours at 37°C to study trafficking of internalized NCs.

Similar to macrovascular ECs shown in the previous chapter, a considerable amount of NCs trafficked to lysosomes: by 1 hour, 18.3±2.3%, 24.5±2.4%, and 16.9±1.8% of bound anti-ICAM NCs trafficked to the lysosome of ACs, human brain microvascular ECs, and PCs, respectively (Figure 16). By 5 hours, ACs accumulated the least percentage of anti-ICAM NCs in lysosomes (39.6±2.6%), which is only 2.2-folds greater than that accumulated

at 1 hour. PCs accumulated $49.4 \pm 2.4\%$ of cell-associated NCs in lysosomes by 5 hours, ~3-fold increase over the percentage at 1 hour. ECs' lysosomes accumulated a greater portion of carriers, $71.2 \pm 1.9\%$ of cell-associated anti-ICAM NCs by 5 hours, also ~3-folds the amount versus 1 hour. All three types of BBB cells tested showed similar trafficking rates ($t_{1/2}$ of ~3.7 to ~4 hours) but differed in absolute lysosomal trafficking, which was greater for ECs.

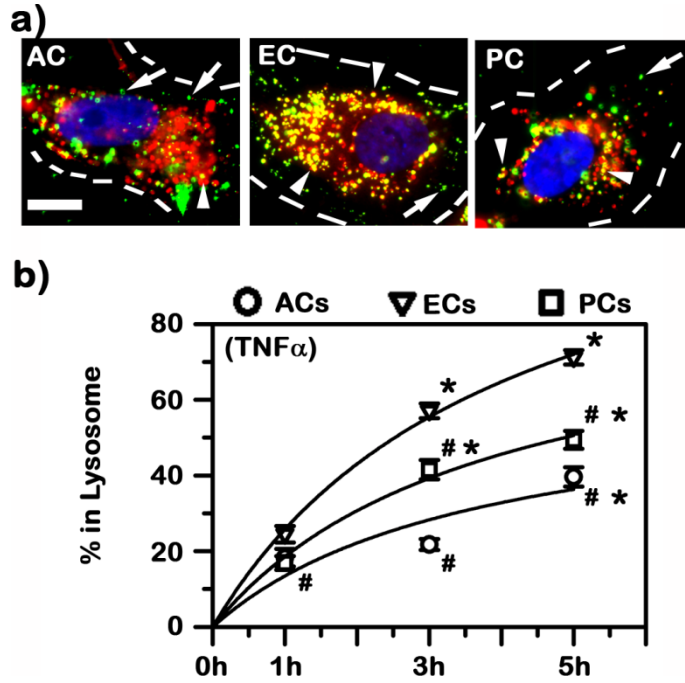


Figure 16. Intracellular trafficking of anti-ICAM nanocarriers to the lysosome of cells of the blood-brain barrier. $\text{TNF}\alpha$ -activated cells were pre-incubated Texas Red dextran to stain lysosomes, then incubated with green fluorescent anti-ICAM NCs for 1 hour at 37°C . To synchronize internalization trafficking of anti-ICAM NCs, cells were then washed to remove non-bound NCs and were then examined or continued to be incubated for a total of 3 or 5 hours at 37°C . Nuclei were stained blue with DAPI. (a) Micrographs of cells incubated for 5 hours. Arrows point to anti-ICAM NCs that do not co-localize with lysosomes (green). Arrowheads point to anti-ICAM NCs that co-localized with lysosomes (red + green = yellow). Scale bar = $10\mu\text{m}$. (b) Kinetics of lysosomal trafficking over 5 hours. Data were fitted to non-linear regression curves, all with $r^2 > 0.90$. Data are mean \pm SEM. # $p < 0.05$, comparing ACs or PCs to ECs for each respective time point; * $p < 0.05$, comparing 1 hour to 3 or 5 hours for each cell type, by Student's t-test.

Since the intended subcellular destination for LSD treatment is the lysosome, lysosomal delivery of anti-ICAM NCs will be optimal for treatment of affected cells, including BBB cells. As seen here, all BBB cell types were able to traffic anti-ICAM NCs to lysosomes to some extent, similar to observations in the previous chapter. This shows ICAM-1-targeting potential to enhance delivery for LSDs. Yet, different cell types yielded various absolute degrees of lysosome transport, and this difference may be due to their different roles. As previously mentioned, brain ECs are heavily involved in endocytotic transport between the blood stream and the brain as compared to ACs or PCs. Hence, it may be expected that ECs could also traffic more material to lysosomes in absolute levels. Yet, due to its role in transcytosis across the BBB, brain ECs are expected to retain less endocytic cargo within intracellular compartments, which may explain the slower trafficking rate to lysosomes: $t_{1/2}$ of ~4 hours compared to ~1-2.5 hours for peripheral ECs (HUVECs) (see Section 4.1.5.). Nonetheless, significant lysosomal delivery achieved in brain ECs is beneficial for many LSDs.

4.2.7. Binding and transport of ICAM-1-targeted nanocarriers across blood-brain barrier endothelial monolayers

In order to treat tissue beyond the vasculature, i.v. administered anti-ICAM NCs must traverse cell barriers to reach the tissue parenchyma. Such is the challenge in crossing the BBB where NCs must traffic across the endothelial and subendothelial linings. The previous experiments involved cells seeded on glass coverslips (Figure 17a). This model is limited in that it does not offer a basolateral compartment underneath the cells and does not allow us to study transport across cells. Therefore, our next step was to study transport of anti-ICAM NCs using a transwell model (Figure 17b). We first tested the specificity and potential

transcellular transport of anti-ICAM NCs across an endothelial monolayer representative of the BBB endothelium. For this purpose, ECs were grown to confluence on porous membrane transwell inserts (Figure 17b). Binding and transport of ICAM-1-targeted delivery systems was evaluated by tagging anti-ICAM with a radioisotope, ^{125}I -anti-ICAM.

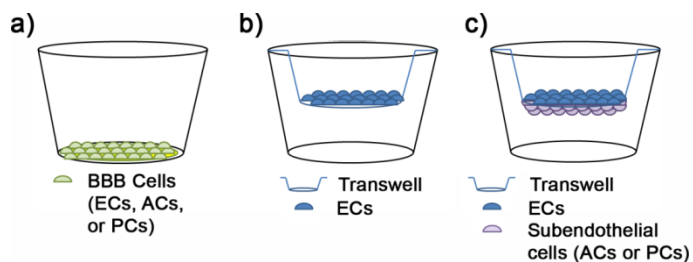


Figure 17. Experimental cell culture models. (a) Cells were seeded onto coated coverslips to analyze binding, internalization, and intracellular trafficking. (b) A BBB monoculture (endothelial) model was developed by culturing human brain microvascular ECs to confluence on 1.0- μm pore transwell inserts for transport assays. (c) Endothelial and subendothelial co-culture models of the BBB were developed by culturing ECs to confluence on apical side of 1.0- μm transwell inserts and either ACs or PCs on the basolateral side of the insert, to study transport across bi-layered cell barrier.

One hour after adding the carriers to the apical chambers above the cells, as many as 1.3×10^6 anti-ICAM NCs per mm^2 surface associated to control healthy cells, a 5.4-fold difference versus non-specific IgG NCs (Figure 18a). In $\text{TNF}\alpha$ -stimulated cells, a total of 6.2×10^6 NCs/ mm^2 of anti-ICAM NCs associated to cells, a 4.7-fold increase over control healthy cells (Figure 18a). The difference between anti-ICAM NCs and IgG NCs associated to cells increased to 18.7-fold difference in $\text{TNF}\alpha$ -stimulated cells, confirming the specificity of anti-ICAM NCs and selectivity toward diseased areas (Figure 18a). Additionally, by 5 hours, there was a 42% reduction in the amount of anti-ICAM NCs associated to cells compared to that at 1 hour. This decrease could be due to active transport across cells and into the basolateral chamber.

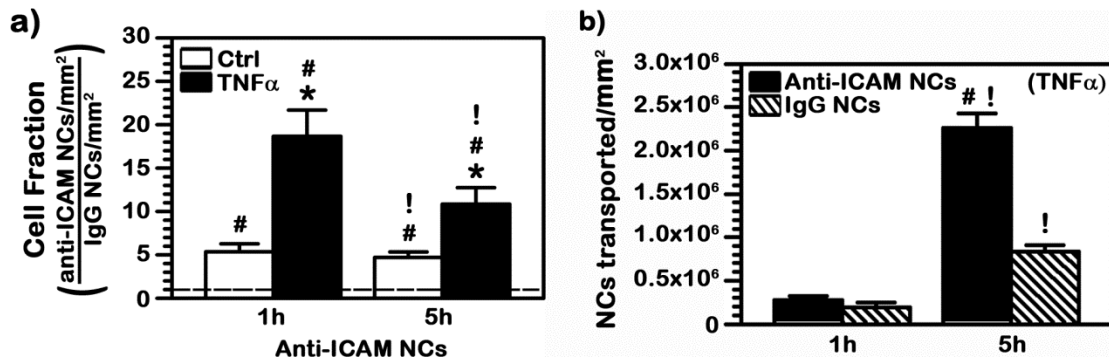


Figure 18. Specific binding and transport of anti-ICAM nanocarriers across brain endothelial monolayers. Control or TNF α -activated HBMECs were cultured to confluence on porous transwell inserts and incubated with ^{125}I -anti-ICAM NCs or non-specific ^{125}I -IgG NCs added to the apical chamber for 30 minutes at 37°C. Non-bound carriers were washed and cells were incubated for a total time of 1 or 5 hours at 37°C. The radioisotope content of the cell fraction (filter inserts) and transported to the basolateral chamber was quantified as absolute number of NCs per mm² insert surface area. (a) Specific binding of anti-ICAM NCs compared to IgG NCs of cells. (b) Amount of NCs transported per surface area of cells. Data are mean \pm SEM. * $p < 0.05$, comparing TNF α to control; # $p < 0.05$, comparing anti-ICAM NCs to IgG NCs; ! $p < 0.05$, comparing 1 hour to 5 hours for each condition, by Student's t-test. (Figure reproduced from [49])

Indeed, by 1 hour, 2.8×10^5 NCs/mm² of anti-ICAM NCs had accumulated in the basolateral chamber, which suggests transport. Although basolateral recovery of control IgG NCs was 3-fold less than anti-ICAM NCs, it was still detectable (8.4×10^5 NCs/mm²), suggesting that the model may allow some non-specific leakage between the compartments. Nonetheless, subtracting this non-specific transport still yielded 1.4×10^6 NCs/mm² of anti-ICAM NCs being specifically transported to the basolateral chamber by 5 hours (Figure 18). This is in line with previous work using transwell models of gastrointestinal epithelial cells (Caco-2 cells [43]), which showed significant ICAM-1-mediated transport across a monolayer of cells. However, less anti-ICAM NCs were transported across epithelial cells compared to that of ECs (~ 250 NCs/cell by 3 hours across Caco-2 monolayers versus ~ 2000 NCs/cell by 5 hours across EC monolayers), possibly because a higher tightness of the Caco-2 monolayer and perhaps lower expression of ICAM-1 [43]. This difference could also be due

to contribution by other transport pathways that was apparent in our results for brain ECs, but was not observed in Caco-2 cells [43]. Hence, the mechanism of transport needs to be studied further.

4.2.8. Mechanism of transport of ICAM-1-targeted nanocarriers across blood-brain barrier endothelial monolayers

Since previous studies have shown CAM-mediated endocytosis to be the primary mechanism of uptake by ECs and also in the case of transcytosis in epithelium (Caco-2 cells [43]), we focused here on testing whether this is conserved for transcytosis by brain ECs (Figure 19).

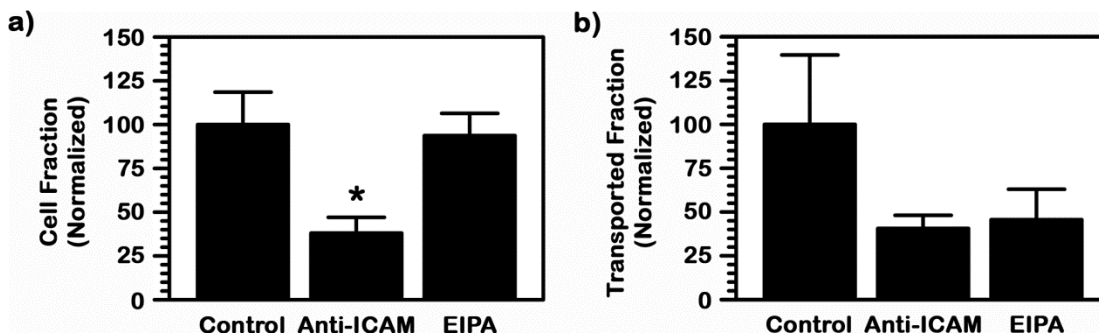


Figure 19. Transport mechanism of anti-ICAM nanocarriers across brain endothelial monolayers. Binding and transport of ^{125}I -anti-ICAM NCs incubated with human brain microvascular EC monolayers in the absence or presence of anti-ICAM molecules (competitive binding of ICAM-1) for 1 hour or amiloride derivative (EIPA, inhibitor of CAM-mediated endocytosis) for 5 hours. (a) Total anti-ICAM NCs remaining in the cell fraction normalized to control. (b) Total anti-ICAM NCs transported into the basolateral chamber normalized to control. Data are mean \pm SEM. * $p < 0.05$, comparing each inhibition condition to respective control, by Student's t-test. (Figure reproduced from [49])

First, to ensure the mechanism of transport was mediated selectively by ICAM-1 binding, we performed a competitive inhibition assay by incubating brain EC monolayers with anti-ICAM NCs in the presence of additional “naked” anti-ICAM molecules. Binding was reduced to $38.0 \pm 9.0\%$ of control and transport to the basolateral chamber diminished to

40.6±7.5% of control (Figure 19), verifying ICAM-1-dependence for this process. In addition, incubation of cells in the presence of EIPA, an amiloride-derivative that inhibits CAM-mediated endocytosis [43], also markedly reduced basolateral transport (45.6±17.4% of control), indicating that this occurs mainly reliant on the CAM-mediated pathway. As expected, EIPA did not reduce binding of anti-ICAM NCs to cells (93.7±12.7% of control) since this molecule only affect endocytic mobilization and not ICAM-1-expression.

Altogether, this set of results shows that ICAM-1-targeted NCs are capable of specifically targeting and traversing through the endothelial layer of the BBB, which is mediated by the CAM-pathway.

4.2.9. Transport of ICAM-1-targeted nanocarriers across blood-brain barrier endothelial-subendothelial bi-layers

Then, to test for transport across both endothelial and subendothelial aspects of the BBB, bi-layer co-culture BBB models were constructed where human brain microvascular ECs were cultured on the apical side of the insert and either ACs or PCs were placed on the opposing basolateral side of the membrane insert (EC-AC or EC-PC co-cultures; Figure 17c). TNF α -stimulated cells were continuously incubated with green fluorescent anti-ICAM NCs. To visually confirm the presence of anti-ICAM NCs associated to cells, transwell membrane inserts were excised and mounted onto microscopy slides, and images were captured with confocal microscopy (Figure 20a). To validate this and avoid potential visual interference of fluorescent carriers which may accumulate in the membrane between the cells, we used ¹²⁵I-anti-ICAM NCs and separately quantified carriers associated with either the endothelial or subendothelial cell lining by scraping off each of these layers from the porous membranes.

Confocal images show that by 24 hours, substantial anti-ICAM NC accumulation in both endothelial and subendothelial layers (Figure 20a). Slightly more anti-ICAM NCs associated to ECs of the bi-layer models versus the subendothelial layer (8.5-fold enhancement over ACs and 20.0-fold over PCs; Figure 20b). Despite the difference and significant accumulation of anti-ICAM NCs in cells, transport of anti-ICAM NCs across both layers and into the basolateral chamber was detectable even by 1 hour (2.6×10^5 NCs/mm² for ECs-ACs and 2.1×10^5 NCs/mm² ECs-PCs) and increased over time (13.1- and 5.8-fold increase by 5 hours, 41.5- and 45.5-fold increase by 24 hours; Figure 20c).

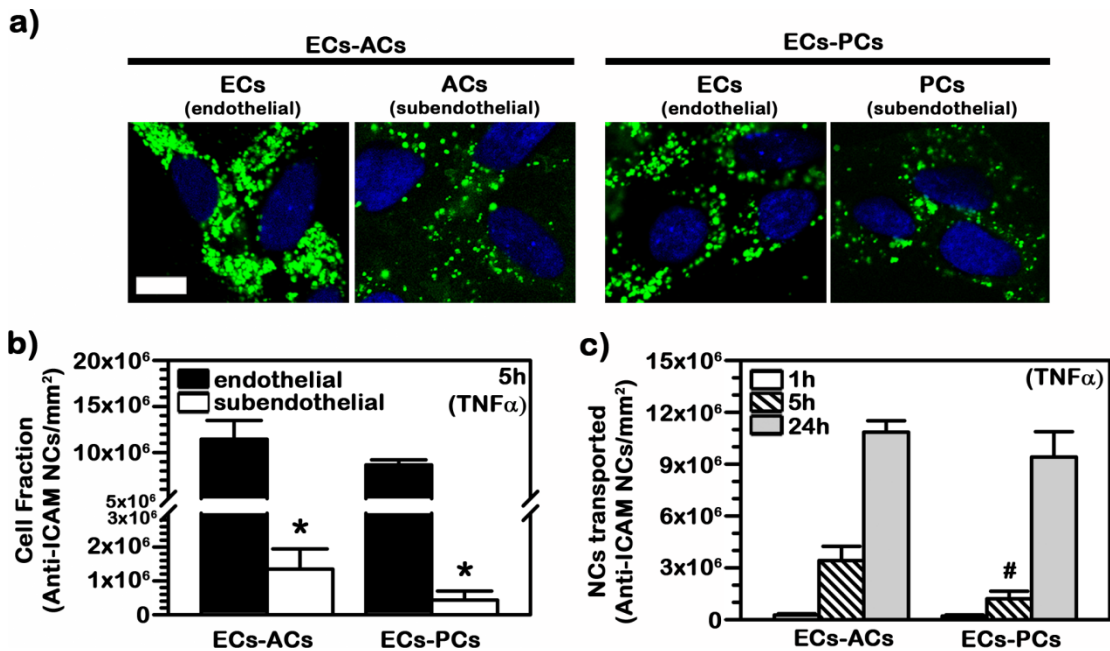


Figure 20. Binding and transport of anti-ICAM nanocarriers across endothelial-subendothelial cell layers. Apical side of porous transwell inserts was seeded with human brain microvascular ECs and grown to confluence and the basolateral side of the same transwell was seeded with either ACs or PCs, also grown to confluence. TNF α -activated cells were incubated with anti-ICAM NCs added to the apical chamber for 1, 5, or 24 hours at 37°C. (a) Confocal images of the endothelial and subendothelial cell linings showing green fluorescent anti-ICAM NCs associated to cells after 24 hours at 37°C. The nuclei of cells were stained blue with DAPI. (b) Total ¹²⁵I-anti-ICAM NCs associated per mm² surface area of endothelial or subendothelial cell layers after 5 hours of incubation at 37°C. (c) Total ¹²⁵I-anti-ICAM NCs transported per mm² surface area across both endothelial-subendothelial cell layers and into the basolateral chamber over 24 hours period. Data are mean \pm SEM. *p<0.05, comparing endothelial layer (ECs) to subendothelial layer (ACs or PCs); #p<0.05, comparing ECs-ACs to ECs-PCs, by Student's t-test. (Figure reproduced from [49])

These results are considerably relevant since successful transport across the BBB and into the brain parenchyma requires that drug delivery systems traverse all layers of both the endothelial and the subendothelial layers of the BBB. Our previous assays had confirmed ICAM-1 expression of ACs and PCs, as well as binding and endocytosis of anti-ICAM NCs via CAM-mediated uptake (Sections 4.2.2. to 4.2.4.). We have also shown transport across brain endothelial monolayers was possible by targeting ICAM-1 (Section 4.2.5.). Here we have completed this information by showing that binding and further transport across both endothelial and subendothelial layers of the BBB is possible. We noted that association of anti-ICAM NCs to the endothelial layer of the BBB is in fact more relevant than of the subendothelial layer, paralleling our findings performed with individual cell cultures, where also ECs bound and internalized anti-ICAM NCs more significantly than ACs and PCs. This difference could be due to more involved role of the ECs on the BBB compared to supporting roles of subendothelial cells. Association of anti-ICAM NCs in subendothelial cells confirms transport across the endothelial layer and also implies that transported anti-ICAM NCs can still interact with subendothelial cells. Additionally, transport yielded across two layers of cells is indicative that anti-ICAM NCs can traverse across the entire BBB structure, therefore, amenable for brain delivery.

4.2.10. ICAM-1 expression on neuroblastoma derived neuron-like cells

Delivery to cells of the brain must be tested to evaluate the potential of ICAM-1-targeted drug delivery to the brain. To evaluate if cells in the brain parenchyma (e.g. neurons) could bind and internalize anti-ICAM NCs, as a proof of concept, we used human neuroblastomas differentiated into neuron-like cells (NLCs). ICAM-1 expression on NLCs was first evaluated to determine whether targeting ICAM-1 is a possible method to deliver cargo to these cells.

As shown in Figure 21, ICAM-1 was expressing on healthy control NLCs (3.0-fold over background fluorescence). Pathological-mimicking conditions ($\text{TNF}\alpha$ -stimulation) heightened the overall ICAM-1 expression (7.7-fold over background; Figure 21a). This correlates well with historic work portraying abundant ICAM-1 expression on neurons [196], especially of those affected by disease [197, 198]. Although, the role of ICAM-1 on neurons has not been clearly elucidated, but speculated to be similar to that of other cell types [196], its involvement in inflammation and immune cell recruitment [139]. Curiously, we noted that ICAM-1 expression was not uniform between the NLC body and cellular processes. In fact, in control healthy cells, 1.9-fold more ICAM-1 expressed at the cell body versus processes. This difference diminished to 1.3-fold under pathological-like conditions. Normalization of

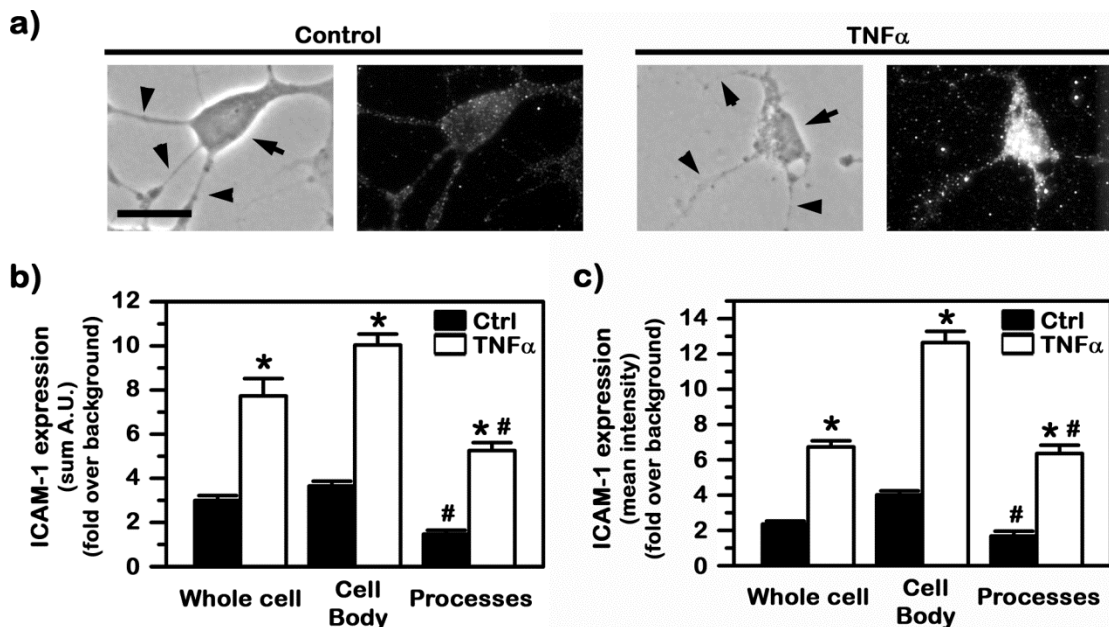


Figure 21. ICAM-1 expression on healthy versus disease-like human neuron-like cells. Differentiated SH-SY5Y cells (NLCs) were cultured with or without $\text{TNF}\alpha$ then fixed and stained for ICAM-1 expression using immunofluorescence. ICAM-1 expression levels were imaged and analyzed through fluorescence microscopy. (a) Phase-contrast images and corresponding fluorescence images portraying ICAM-1 expression on control and $\text{TNF}\alpha$ -activated cells. Arrows point to cell bodies and arrowheads point to processes. Scale bar = 10 μm . (b) The sum intensity of fluorescence or (c) the mean intensity corresponding to ICAM-1 expression per surface area of a whole cell, the cell body, or cell processes was calculated as fold-difference over background fluorescence. Data are mean \pm SEM. * $p < 0.05$, comparing $\text{TNF}\alpha$ to control within each group; # $p < 0.05$, comparing cell body to processes, by Student's t-test.

expression to the cell surface area in each of these compartments showed that ICAM-1 expression was more concentrated on the cell body versus processes (2.4-fold difference in control cells, 2.0-fold in diseased cells; Figure 21b). Yet, the overall fold-enhancement of ICAM-1 expression as a result of TNF α -stimulation was higher in the processes: 2.3-fold increase on the cell body versus 3.4-fold increase on cellular processes compared to healthy controls (Figure 21a). It was interesting to observe regional differences in ICAM-1 expression. This also suggests the possibility of controlling avidity of ICAM-1-targeting drug delivery systems to differentiate regional targeting on neurons altogether.

4.2.11. Binding of ICAM-1-targeted nanocarriers to neuron-like cells

Previous works suggest that the level and pattern of ICAM-1 expression on cells does not necessarily predict the cell's potential to bind anti-ICAM NCs. Hence, binding specificity, efficiency, and disease selectivity was studied on NLCs. Indeed, ICAM-1 expression did not correlate to binding efficiency. For instance, even though the overall expression difference between healthy versus TNF α -activated NLCs was 2.7-fold (Figure 21b), the binding difference was 4-folds by 1 hour, with anti-ICAM NCs binding more efficiently to TNF α -activated cells (107.5 \pm 9.8 NCs/cell) than healthy cells (27.1 \pm 1.8 NCs/cell; Figure 22a, b). Interestingly, this fold difference between healthy and diseased cells was consistent amongst different cellular regions: 3.9-fold increase in cell body and 4.0-fold increase in cell process (Figure 22a, b). A closer look revealed that processes bound \sim 2.1-fold more anti-ICAM NCs than cell body in both healthy and diseased conditions (Figure 22b), opposite to the fact that less ICAM-1 was expressed on processes versus the cell body (1.3- to 1.9-fold less than cell body; Figure 21b). Normalizing binding to area to assess density of bound anti-ICAM NCs illustrated that 8.1 \pm 0.6 NCs bound per mm² on healthy cells versus 33.4 \pm 3.1 NCs/mm² on

diseased cells. Binding density on NLC processes proved to be 2.1-fold more dense compared to the cell body in control conditions and 1.6-fold more dense in diseased conditions (11.0 ± 0.5 NCs/ μm^2 and 39.7 ± 1.7 NCs/ μm^2 ; Figure 22c).

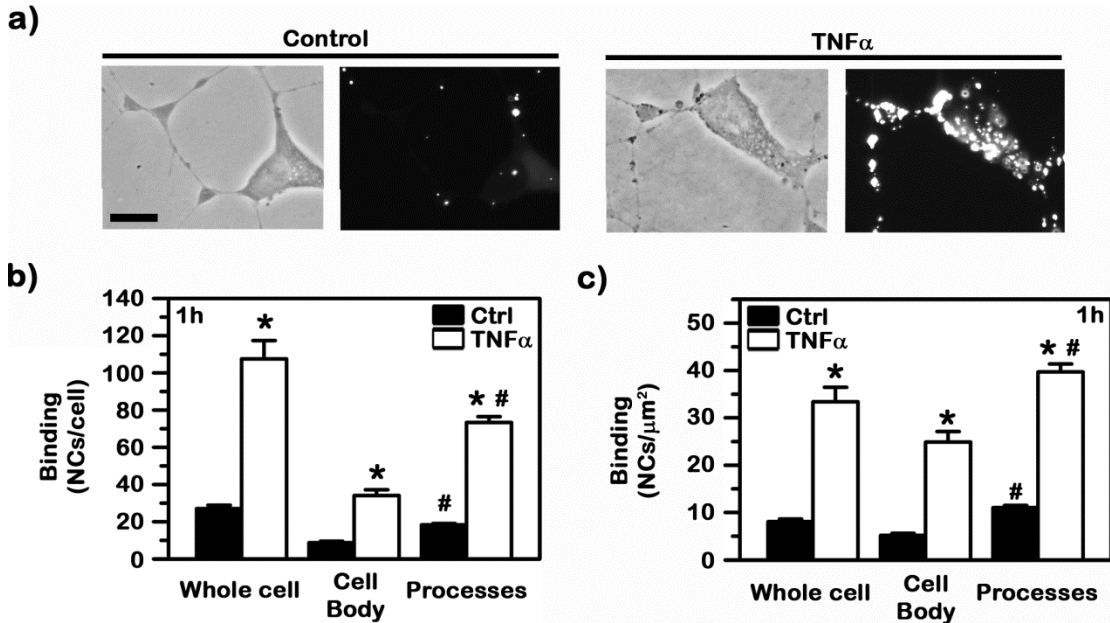


Figure 22. Binding of anti-ICAM nanocarriers to neuron-like cells. Green fluorescent anti-ICAM NCs were incubated with control or TNF α -activated NLCs for 1 hour at 37°C, then washed and fixed for immunofluorescence analysis. (a) Phase-contrast images and corresponding fluorescence images portraying anti-ICAM NCs bound on control versus TNF α -activated cells. Scale bar = 10 μm . (b) Comparison of total anti-ICAM NCs bound per control or TNF α -activated whole cell, cell body, or cell processes. (c) Comparison of total anti-ICAM NCs bound per μm^2 area of control or TNF α -activated cells quantified per whole cell, cell body, or cell processes of a cell. Data are mean \pm SEM. * $p < 0.05$, comparing TNF α to control within each group; # $p < 0.05$, comparing cell body to processes, by Student's t-test.

By 5 hours, binding of anti-ICAM NCs to NLCs had minimally increased (127.3 ± 7.8 NCs/cell; Figure 23a). Regionally, binding of anti-ICAM NCs did not change over this time in processes (73.4 ± 3.1 NCs/cell at 1 hour, 65.6 ± 5.2 NCs/cell by 5 hours). However, binding of anti-ICAM NCs did increase with time on the cell body (34.1 ± 3.1 NCs/cell at 1 hour, 61.8 ± 5.2 NCs/cell by 5 hours), accounting for the minimal increase in the whole cell. Hence, it appears that anti-ICAM NCs bind to processes of NLCs more rapidly ($t_{1/2}$ of < 0.1 minute)

than the cell body ($t_{1/2}$ of 83.9 minutes), reaching a similar binding saturation: B_{max} of ~ 63.2 NCs/cell for the cell process versus B_{max} of ~ 70.2 NCs/cell for the cell body. Interestingly, when analyzing change in binding over time as binding density per surface area, similar binding rates were observed. However, saturation of binding density of the cell body was 1.5-fold more than processes: B_{max} of ~ 51.2 NCs/ μm^2 of the cell body versus B_{max} of ~ 34.2 NCs/ μm^2 of processes (Figure 23b), suggesting that more anti-ICAM NCs could potentially bind to the cell body versus the cell process.

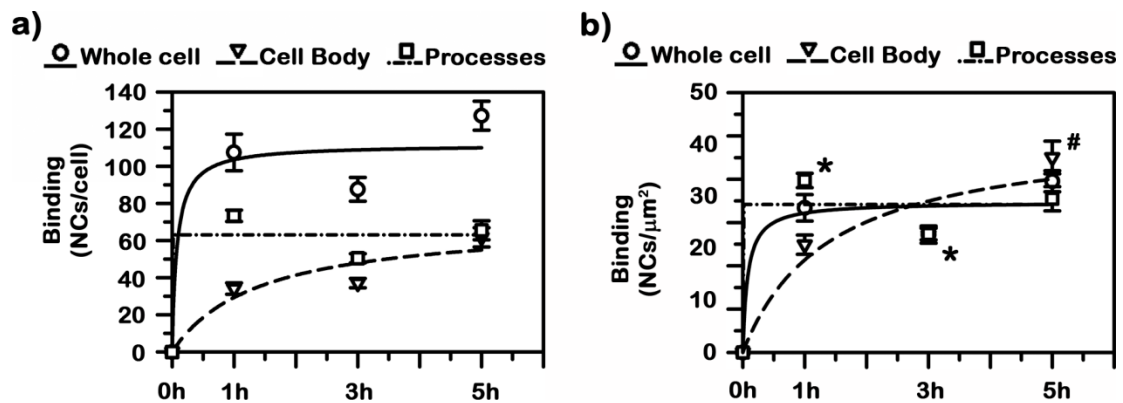


Figure 23. Kinetics of anti-ICAM NCs binding to neuron-like cells and cell regions. Green fluorescent anti-ICAM NCs were incubated with TNF α -activated NLCs for 1, 3, or 5 hours at 37°C, then washed and fixed for immunofluorescence analysis. (a) Total anti-ICAM NCs bound per whole cell, cell body, or cell processes over time. (b) Total anti-ICAM NCs bound per μm^2 area of a whole cell, cell body, or cell processes over time. Data were fitted to non-linear regression curves, all with $r^2 > 0.90$. Data are mean \pm SEM. * $p < 0.05$, comparing TNF α to control within each group; # $p < 0.05$, comparing cell body to processes, by Student's t-test.

Once again, the level of ICAM-1 expression did not dictate accessibility and availability for binding. Total anti-ICAM NCs bound to cell processes (absolute or normalized by surface area) was greater than that bound to the cell body, even though more ICAM-1 was expressed on cell body over processes. This might be due to accessibility of ICAM-1 protein on the neuron surface, e.g. either dispersed versus concentrated in clusters, or masked by furrows on the membrane, interactions with other receptors, etc., which may

cause steric hindrance affecting binding of NCs differently from binding of antibodies used for assessing expression. Or, maybe simply binding saturation as a result of accessibility and availability of ICAM-1 varies depending on the rate of binding. As seen, a slower binding rate to the NLC body could potentially result in greater binding of anti-ICAM NCs compared to the rapid binding to NLC processes, suggesting that total amount of anti-ICAM NCs capable of binding is not necessarily dependant on the rate of binding. Nonetheless, anti-ICAM NCs can bind to both regions, albeit at different densities and at different rates. This is promising for drug delivery purposes as processes in many mature neurons are myelinated creating another barrier to delivery and, therefore, anti-ICAM NCs may be able to circumvent this issue and bind directly to the cell body. Depending on the purpose of the delivery, anti-ICAM NCs can possibly be controlled by adjusting NC formulation to control avidity. In these studies, it is possible that binding saturation may also be dependent of subsequent cellular trafficking of NCs, such as endocytosis, which has the potential for recycling ICAM-1 back to the surface for sustained binding of NCs or the potential for limiting binding due to endocytosis with concomitant uptake of surface ICAM-1, as observed in macrovascular endothelial cells (HUVECs) [157].

4.2.12. Endocytosis of ICAM-1-targeted nanocarriers into neuron-like cells

Next, using fluorescence microscopy, we examined whether bound anti-ICAM NCs were endocytosed by NLCs. Within 1 hour of incubation, anti-ICAM NCs was in fact endocytosed into NLCs (9.7 ± 0.3 NCs/cell; Figure 24b). Similar to selectivity in binding, uptake of anti-ICAM NCs was significantly higher in cells stimulated with $\text{TNF}\alpha$ versus healthy cells (35.9 ± 1.4 NCs/cell; 3.7-fold increase over control cells; Figure 24a, b). Interestingly, upon closer examination, a similar regional relationship between cell body and processes exhibited

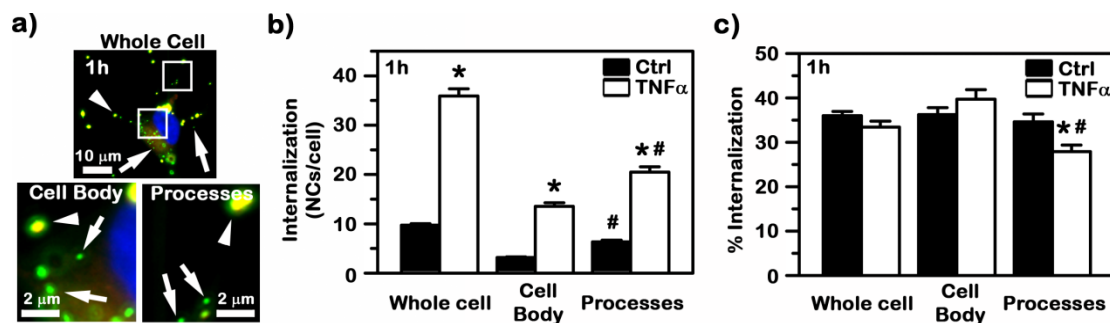


Figure 24. Internalization of anti-ICAM nanocarriers into neuron-like cells. Green fluorescent anti-ICAM NCs were incubated with control or TNF α -activated NLCs for 1 hour at 37°C, then washed and fixed. Surface bound NCs were stained with Texas Red secondary antibody and nuclei were stained blue with DAPI for fluorescence microscopy analysis. (a) Fluorescence images of anti-ICAM NCs internalized into TNF α -activated NLCs after 1 hour. Arrows point to internalized anti-ICAM NCs (green) and arrowheads point to surface bound anti-ICAM NCs (red + green = yellow). Scale bar = 10 μ m or 2 μ m. (b) Total internalized anti-ICAM NCs per control or TNF α -activated whole cell, cell body, or cell processes. (c) Percentage of bound anti-ICAM NCs internalized into control or TNF α -activated whole cell, cell body, or processes of a cell. Data are mean \pm SEM. * p <0.05, comparing TNF α to control within each group; # p <0.05, comparing cell body to processes, by Student's t-test.

in anti-ICAM NC binding was conserved regarding the endocytosis pattern. Cell processes endocytosed 1.5- to 2-folds more NCs than cell bodies in both control and diseased cells (Figure 24b). Interestingly, endocytosis efficiency, described as percent uptake relative to total anti-ICAM NCs associates to cells, remained consistent between healthy and diseased cells (~35%; Figure 24c), suggesting that uptake efficiency is not dependent nor affected by pathological state of cell. This is also true when examining the cell body (~38% internalization). However, this is not the case for cell processes, in fact, internalization efficiency decreases with TNF α -stimulation (34.6 \pm 1.8% in control cells versus 27.9 \pm 1.5% in diseased cells), contrasting ICAM-1-expression and anti-ICAM NC binding pattern which increased in the cell processes of diseased cells (Figures 21 and 22). Perhaps binding of anti-ICAM NCs to cell processes is rapid (as with a rapid $t_{1/2}$ of <0.1 minute; Figure 23) and hence quickly saturates, but the mobilization of vesicular uptake is slow. Nonetheless, even though cell processes endocytose more anti-ICAM NCs than the cell body (20.5 \pm 1.1 NCs/cell in cell

processes versus 13.6 ± 0.7 NCs/cell in the cell body; Figure 24b), it seems that the cell body is more efficient in internalizing associated anti-ICAM NCs ($39.7 \pm 2.2\%$ in cell body versus $27.9 \pm 1.5\%$ in cell processes; Figure 24c).

With regard to the kinetics of endocytosis, similar to binding patterns, absolute number of anti-ICAM NCs endocytosed into whole NLCs minimally increases over time, 35.9 ± 1.4 NCs/cell at 1 hour to 40.3 ± 2.6 NCs/cell by 5 hours (Figure 25a, b). This may be due to a rapid internalization rate ($t_{1/2}$ of 1.2 minutes), yielding an I_{\max} of ~ 35.7 NCs/cell. The rapid internalization rate is largely contributed by rapid uptake into NLC processes ($t_{1/2}$ of < 0.1 minute) similar to the observed binding rate. A modest maximum internalization (I_{\max}) calculated to be ~ 17.3 NCs/cell, and interestingly, total number of NCs internalized into processes decreases over time (Figure 25b). This may suggest that uptake is rapid in processes perhaps followed by retrograde transport to the cell body. In agreement with this,

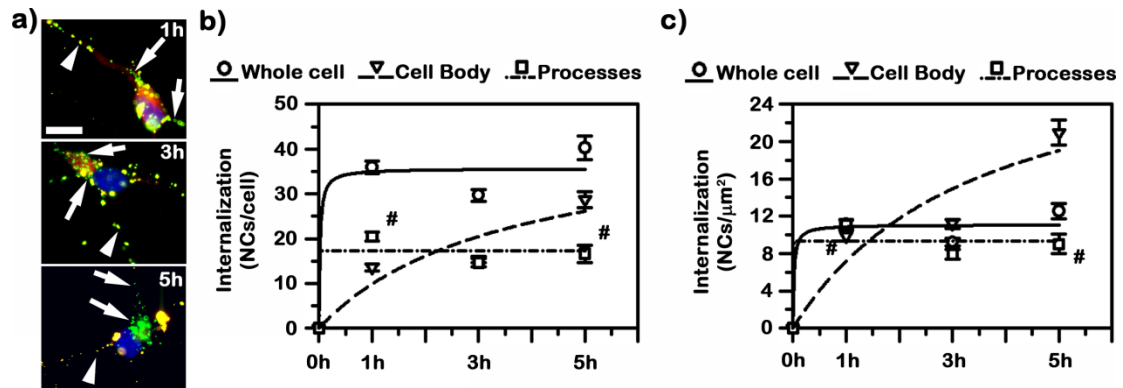


Figure 25. Kinetics of anti-ICAM nanocarriers uptake by neuron-like cells. Green fluorescent anti-ICAM NCs were incubated with TNF α -activated NLCs for 1, 3, or 5 hours at 37°C, then washed and fixed. Surface bound NCs were stained with Texas Red secondary antibody and nuclei were stained blue with DAPI for fluorescence microscopy analysis. (a) Fluorescence images of anti-ICAM NCs internalized into TNF α -activated NLCs after 1, 3, or 5 hours. Arrows point to internalized anti-ICAM NCs (green) and arrowheads point to surface bound anti-ICAM NCs (red + green = yellow). Scale bar = 10 μm . (b) Total anti-ICAM NCs internalized per whole cell, cell body, or cell processes over time. (c) Total anti-ICAM NCs internalized per μm^2 area of a whole cell, cell body, or cell processes over time. Data were fitted to non-linear regression curves, all with $r^2 \geq 0.89$. Data are mean \pm SEM. # $p < 0.05$, comparing cell body to cell processes, by Student's t-test.

uptake rate in the NLC body was observed to be extremely slow ($t_{1/2}$ of 3.5 hours) and total anti-ICAM NC accumulation increases 2.1-fold by 5 hours compared to 1 hour, with the potential to reach an I_{\max} of ~ 44.4 anti-ICAM NCs/cell (I_{\max} of ~ 32.4 anti-ICAM NCs/ μm^2 in cell body versus ~ 10.2 anti-ICAM NCs/ μm^2 for cell processes and whole cell; Figure 25c).

As compared to our previous data, this study revealed that the endocytosis efficiency is not affected by pathological state of the cell, a similar phenomenon to that seen in other cell types (e.g. HBMECs, PCs). However, relative uptake in NLCs remained modest ($\sim 35\%$) in comparison to BBB cells, which had an average uptake efficiency of $\sim 50\%$ (Figure 14). Nonetheless, this could be due to the innate role of these cell types. BBB cells regulate transport of small and large material and protect the brain parenchyma from foreign invasions, and therefore may endure higher frequency of endocytosis. Indeed, rate of endocytosis into these cell types is not as rapid as NLC processes but not as slow as NLC body ($t_{1/2}$ of ~ 3.5 hours in NLC body versus an average $t_{1/2}$ of 88 minutes in BBB cells; Figure 25 and 14, respectively), but the achievable internalization maximum is much higher, ~ 90 to ~ 300 NCs/cell in BBB cells versus ~ 30 NCs/cell in NLC body. In any instance, this may still be relevant from the perspective of delivery into NLCs via ICAM-1-mediated mechanisms.

4.2.13. Mechanism of endocytosis of ICAM-1-targeted nanocarriers in neuron-like cells

Uptake of molecules into neurons appears largely been dependent on clathrin endocytosis (e.g. neurotransmitters [199, 200]), yet ICAM-1-targeted carriers do not capitalize this pathway but on CAM-mediation for endocytosis. In agreement with this, amiloride did inhibit internalization of anti-ICAM NCs in NLCs more so than any other inhibitor ($15.9 \pm 3.4\%$ reduction; Figure 26). However, interestingly, the effect of amiloride was significant only for the cell body but not cellular processes; $40.5 \pm 3.8\%$ reduction in cell body versus $2.9 \pm 8.9\%$

reduction in processes (Figure 26b). Moreover, MDC treatment to inhibit clathrin-mediated endocytosis resulted in a modest increase of internalization into the cell processes, although without statistical significance ($7.9\pm 9.5\%$ increase), but slightly decreased internalization in the cell body ($11.7\pm 4.5\%$ reduction; Figure 26b). Additionally, filipin treatment, inhibitor of caveolae-mediated endocytosis, did not affect internalization efficiency in either cell regions ($\sim 95\%$ of control for both cell body and cellular processes).

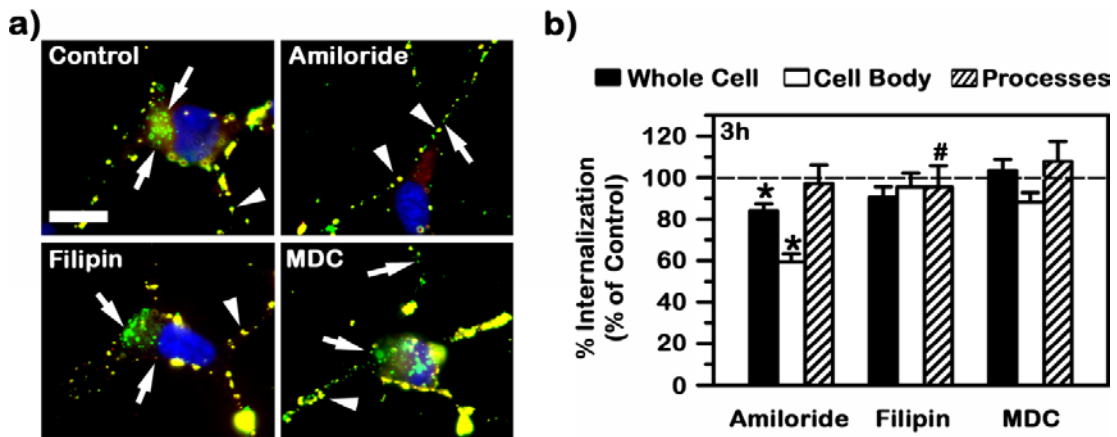


Figure 26. Mechanism of uptake into neuron-like cells and cell regions. $\text{TNF}\alpha$ -activated NLCs were incubated with FITC-analog labeled anti-ICAM NCs for 3 hours at 37°C in absence (control) or presence of either amiloride (CAM-mediated endocytosis inhibitor), filipin (caveolae-mediated endocytosis inhibitor), or MDC (clathrin-mediated endocytosis inhibitor). Cells were washed to remove non-bound NCs and stained with Texas Red secondary antibody, nucleus was stained with DAPI. (a) Arrows point to internalized anti-ICAM NCs (green). Arrowheads point to surface bound anti-ICAM NCs (red + green = yellow). Scale bar = $10\mu\text{m}$. (b) Percent of internalization relative to control cells. Data are mean \pm SEM. * $p < 0.05$, comparing inhibitors to control within each group; # $p < 0.05$, comparing cell body to processes, by Student's t-test.

Therefore, similar to other cell types previously tested, the main mechanism of endocytosis into NLCs is via CAM-mediation, although, whole NLC internalization was only modestly reduced compared to BBB cells (e.g. reduction of $40.0\pm 3.7\%$ in ECs (Figure 15). This was similar to the effect seen on the NLC body. Perhaps this is because neuron morphology has vastly differing regions with distinct roles while other cell types, such as

BBB cells, have a more uniform cell surface and more dynamic plasmalemmas. Internalization into NLC processes, on the other hand, was not affected by amiloride. Neuronal processes are known to heavily utilize clathrin-mediated endocytosis for uptake [199, 200]. Therefore, it is possible that anti-ICAM NCs bound to ICAM-1 can be passively incorporated into the abundant clathrin-pits that continuously form in NLC processes in the case of CAM-inhibition so that no effect is observed. As previously emphasized, some classical endocytic mechanisms, such as clathrin-mediated endocytosis, are impaired in some LSDs [27-29]. Hence, anti-ICAM NCs may overcome this impediment not only by CAM-mediation, but also by relying on multiple options of endocytosis (Figures 16, 26).

4.2.14. Lysosomal trafficking of ICAM-1-targeted nanocarriers in neuron-like cells

Lysosomal delivery of anti-ICAM NCs into model neurons was analyzed by fluorescently labeling the lysosome with Texas Red dextran and tracing green fluorescent anti-ICAM NCs for co-localization with lysosomes (red + green = yellow) (Figure 27a). Immunofluorescence showed a low level of anti-ICAM NCs colocalization with intracellular lysosomes by 1 hour ($25.4 \pm 2.4\%$ of all cell-associated anti-ICAM NCs; Figure 27b), but this was increased with time: up to $42.8 \pm 2.4\%$ of all cell-associated carriers localizing within this compartment by 3 hours in activated human NLCs (arrows pointing to yellow particles; Figure 27a). This seemed to be a saturating level of lysosomal transport, as it did not further increase by 5 hours ($45.9 \pm 2.3\%$ colocalization, with a $t_{1/2}$ of ~ 74.5 minutes and a calculated co-localization maximum of 58.4%), which is in agreement with a total level of $\sim 35\%$ of carrier being internalized by this time (compare with Figure 25). Therefore, focusing only on those carriers internalized by cells, the level of lysosomal transport would be $\sim 100\%$. A closer examination showed regional differences. Interestingly, the cell body had a faster rate of lysosomal

trafficking than cell processes ($t_{1/2}$ of ~22.2 minutes in cell body versus $t_{1/2}$ of ~75.9 minutes in processes; Figure 27b). In fact, by 5 hours a greater percentage of anti-ICAM NCs trafficked to the lysosome of the cell body ($54.6 \pm 2.5\%$) versus that of NLC processes ($36.7 \pm 5.5\%$ in lysosomes).

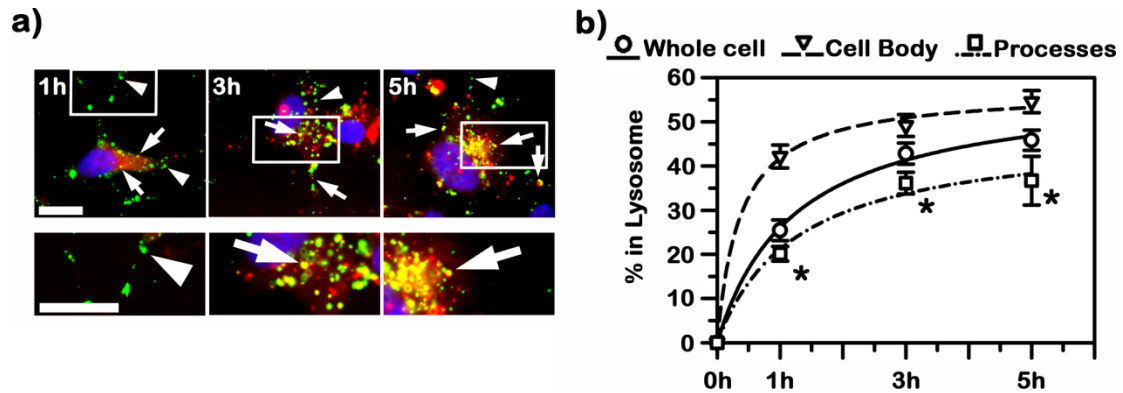


Figure 27. Lysosomal trafficking of anti-ICAM NCs in neuron-like cells. $\text{TNF}\alpha$ -activated NLCs were pre-incubated Texas Red dextran to stain lysosomes, then incubated with green fluorescent anti-ICAM NCs for 1 hour at 37°C . To synchronize internalization trafficking of anti-ICAM NCs, cells were then washed to remove non-bound NCs and were then examined or continued to be incubated for a total of 3 or 5 hours at 37°C . Nuclei were stained blue with DAPI. (a) Fluorescence images of cells incubated for 1, 3, or 5 hours (top). Boxed regions are magnified 2-folds (bottom). Arrows point to anti-ICAM NCs in lysosomes (red + green = yellow). Arrowheads point to anti-ICAM NCs which do not co-localize with lysosomes (green). Scale bar = $10\mu\text{m}$. (b) Kinetics of lysosomal trafficking over 5 hours. Data are mean \pm SEM. * $p < 0.05$, comparing cell body to processes, by Student's t-test.

Lysosomes is the intended destination for LSDs, hence these results show the potential of targeting ICAM-1 for lysosomal delivery in neurons. Interestingly, neurons trafficked anti-ICAM NCs to the lysosome faster than BBB cells ($t_{1/2}$ of ~4 hours, see Section 4.2.6.; Figure 16). The overall percentage of anti-ICAM NCs trafficked to the lysosomes of NLCs was actually similarly efficient compared to ACs and PCs ($45.9 \pm 2.3\%$ in lysosomes of NLCs versus $39.6 \pm 2.6\%$ in ACs and $49.4 \pm 2.4\%$ in PCs; Figure 27 and 16, respectively), but less efficient than brain ECs (1.6-fold less). It is especially interesting that a greater percentage of NCs co-localize with lysosomes in the cell body while uptake was faster for

processes and total amount of NCs associated with processes decreased with time. In fact, the cell body traffics anti-ICAM NCs faster to the lysosome than NLC processes, yet the opposite is seen for rate of endocytosis. This may indicate that lysosomes in the NLCs are predominately located in the cell body and anti-ICAM NCs follow a processes-to-body transport. Since neuron processes actively and frequently retrograde endocytosed material to the cell body, such as other delivery vectors [201], this phenomenon could indirectly increase the lysosomal co-localization detected in cell body and diminish the absolute values in the NLC processes. Nonetheless, anti-ICAM NCs ultimately target lysosomes, showing that ICAM-1-targeted drug delivery systems can systemically deliver NCs to lysosomes of various cell types, including difficult to reach tissue.

4.2.15. Conclusion

Targeting to the brain is highly coveted for several neuropathy and/or neurodegenerative treatments. However, the highly regulating BBB have often been the main impediment. Here we show that targeting ICAM-1, a cell surface molecule inherently involved in leukocyte extravasation, assisted the binding, uptake, and transport of NCs to and across cell barriers [49]. Specifically, anti-ICAM NCs were capable of binding and internalizing into cells of the BBB (ECs, ACs, and PCs), traverse this lining, and target cells of the brain, such as NLCs. Uptake of anti-ICAM NCs into cells was shown to be achieved mainly via CAM-mediated endocytosis, although other routes may assist and compensate endocytosis. This shows that uptake of anti-ICAM NCs into these cells can bypass clathrin-mediated endocytosis if that route is impaired, as speculated in several LSDs [27-29]. Moreover, a fraction of anti-ICAM NCs was also able to traffic to lysosomes of these cells (~35-70% of cell associated anti-

ICAM NCs by 5 hours). This is important for LSD treatment since all cells are affected by LSDs, hence the need for systemic delivery.

Interestingly, due to cell morphology and phenotype, subendothelial cells and NLCs portrayed different binding and uptake profiles than ECs. Since ECs directly interact with the circulating blood, ECs could have a tendency to bind and internalize more anti-ICAM NCs faster than other BBB cell, as seen in our results. Additionally, ACs and PCs uptake less anti-ICAM NCs. This suggests that anti-ICAM NCs traversing across the BBB would not be “entrapped” in the subendothelial layer, and can further bind to cells of the brain. Indeed, anti-ICAM NCs can target cells of the brain. Another interesting phenomenon is that different regions of the NLC behave differently in response to anti-ICAM NCs. In fact, faster and more anti-ICAM NCs bound to cell processes, yet more anti-ICAM NCs internalized and trafficked to lysosomes, and faster, in the cell body. This may be in line with historic observations showing reliance on cellular neurites to uptake material versus the cell body, and for endocytosed materials to retrograde towards the cell body [201]. This may explain how we observed less anti-ICAM NCs binding to cell body, but more internalized in this region.

All in all, in addition to vascular endothelial cell targeting, anti-ICAM NCs seem to traverse the BBB and target lysosomes in cells of the BBB and the brain, showing promise in utilizing ICAM-1-targeting platform to enhance delivery of therapeutic to treat diseases that manifest both systemic and CNS symptoms, such as several LSDs.

4.3. Enhanced delivery of lysosomal enzyme to organs in mice by ICAM-1-targeting

4.3.1. Introduction

As mentioned, currently available ERTs target M6PR for lysosomal delivery. However, this method renders poor cellular uptake and leads to suboptimal distribution of ERT to target organs while accumulating into clearance organs (e.g. kidneys, liver, spleen) [35, 84, 85], pairing well with liver and spleen having high M6PR expression [80, 90-92]. Moreover, the major tissues that are severely affected by FD (kidney, vasculature) [45], PD (heart, liver, skeletal muscles) [46], and NPD (brain, liver, lungs) [202] are challenging to reach by a therapeutic that does not preferentially target to diseased organs, especially intractable tissue that requires transport across cell barriers (e.g. brain) [34]. Hence, an alternative targeting strategy to help deliver the enzyme therapeutic to all tissues affected by the disease may improve ERT efficacy.

Previous work with anti-ICAM/ASM NCs has shown promise [41]. ICAM-1-targeting of ASM, for NPD treatment, was able to enhance enzyme delivery to major tissues (heart, kidneys, liver, lungs, spleen) versus non-targeted enzyme, while avoiding majority of delivered enzyme from being cleared to clearance organs [41]. However, it is unknown whether this is unique to anti-ICAM/ASM NCs or if other cargoes could contribute a steric hindrance or somehow disrupt binding pattern of anti-ICAM NCs. Hence, we assess here whether ICAM-1-targeted α Gal and GAA share the same fate. Furthermore, the brain is a major target organ for neuropathic LSDs. Enzyme delivery to this organ via anti-ICAM NCs has not been assessed previous to this work.

4.3.2. Circulation of anti-ICAM/enzyme nanocarriers versus non-targeted enzyme in mice

We first studied enzyme enzyme circulation after i.v. injection, for which α Gal and GAA were radioactively labeled with ^{125}I to enable tracing in vivo. As a proof-of-concept model, 100 nm diameter polystyrene nanoparticles were coated with ICAM-1-targeting antibodies and ^{125}I -enzyme molecules (95:5 antibody to enzyme mass ratio; minimal amounts of enzyme were needed to trace its distribution). As previously discussed, polystyrene nanoparticles enable tracing without the effects of biodegradation. As an anti-ICAM NC model, polystyrene NCs have been previously characterized and determined to behave similarly to biodegradable PLGA NCs [41, 203]. Anti-ICAM/ ^{125}I - α Gal NCs, anti-ICAM/ ^{125}I -GAA NCs, and respective dose matched non-targeted enzyme were i.v. injected into mice. To evaluate rate of retention or removal of ^{125}I - α Gal and ^{125}I -GAA in circulation, mouse blood was collected 1, 15, and 30 minutes post-injection and analyzed by determining the presence of ^{125}I using a gamma counter.

Within 1 minute of injection, minimal amount of anti-ICAM NC-associated enzymes were traceable in blood (Figure 28): only $5.85\pm 0.67\%$ and $2.60\pm 0.47\%$ of injected dose (%ID) of anti-ICAM/ α Gal NC and anti-ICAM/GAA NC, respectively, remained in circulation, and continued to remain low throughout the duration of the experiment (Figure 28a, b). The rapid removal of anti-ICAM/enzyme NCs from circulation correlates well with historical data on anti-ICAM/ASM NCs, of which only $3.32\pm 0.46\%$ ID remained in circulation 30 minutes post-injection [41]. This was opposite for non-targeted enzyme equivalents, where the majority of the injected dose was detected in circulation by 1 minute: $64.72\pm 3.96\%$ ID and $51.76\pm 1.62\%$ ID of non-targeted α Gal and GAA, respectively, which only minimally decreased by 30 minutes ($42.07\pm 2.22\%$ ID and $38.40\pm 2.11\%$ ID; Figure 28a, b). This is also in agreement with previous work on delivery of ASM, in which $59.9\pm 6.5\%$ ID

of non-targeted ASM remained in circulation by 1 minute post-injection, and similarly, decreased only to $31.6 \pm 2.9\%ID$ by 30 minutes.

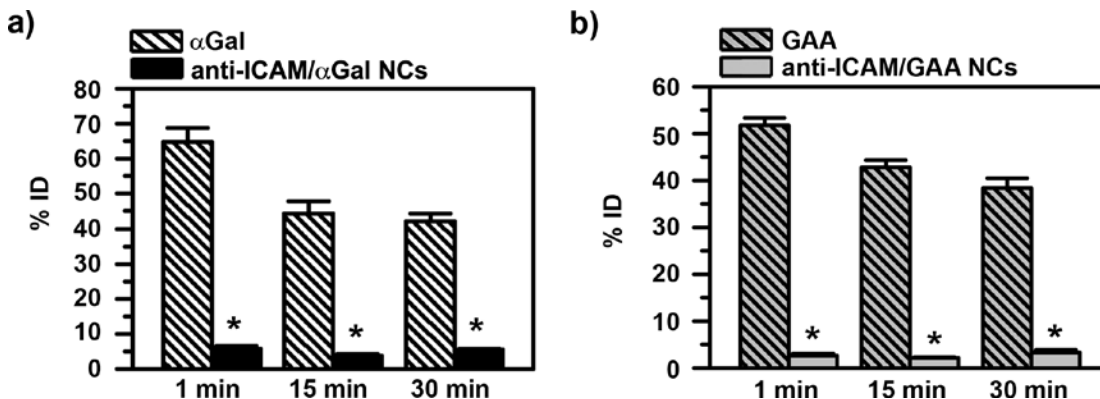


Figure 28. Circulation of anti-CAM/enzyme nanocarriers. ^{125}I -labeled enzyme was used to trace enzyme in the body. Mice were injected with either anti-ICAM/ ^{125}I -enzyme NCs or non-targeted ^{125}I -enzyme and blood was collected at 1, 15, or 30 minutes post-injection. Percent of injected dose (%ID) describes the total amount of enzyme traced in blood samples from mice injected with (a) anti-ICAM/ ^{125}I - α Gal NCs versus ^{125}I - α Gal or (b) anti-ICAM/ ^{125}I -GAA NCs versus ^{125}I -GAA. Data are mean \pm SEM. * $p < 0.01$, comparing anti-ICAM/enzyme NCs to non-targeted enzyme, by Student's t-test. (Figure adapted from [47, 48])

A priori, short half-life in blood of anti-ICAM/enzyme NCs may seem detrimental to efficient therapy. Indeed, this is the case for delivery strategies that rely on diffusion of relatively small drug molecules from the circulation into tissues, or for drug carriers designed for delivery of cancer therapeutics [204]. These strategies require passive transport into the tumor parenchyma across the leaky vasculature of tumor blood vessels, via the enhanced permeability and retention effect [204]. However, in the case of ERT for LSDs, the non-targeted enzyme counterparts studied here that remained in circulation for longer most likely due to the lack of active targeting, which is needed to achieve receptor-mediated endocytosis through the body. Such extended circulation time could prolong therapeutic effects by allowing slow accumulation to tissue, but it can also give rise to immune recognition and inevitable clearance by RES and kidneys, as have been noted with current ERT [95-99, 101].

Hence, rapid removal from the blood may be beneficial in this case to avoid premature degradation and/or recognition by the immune system [95, 205]. This is particularly relevant in the case of therapeutic biologics, as long as fast clearance from blood does not impair targeting of the intended tissues. Rapid clearance may be indicative of fast targeting to ICAM-1-rich tissue. Presentation of multiple copies of the enzyme on the nanocarrier surface may also pose immunological concerns, which remain to be investigated. Yet, this model represents a proof-of-concept for ICAM-1-targeting and enzymes can be encapsulated to avoid such outcome.

4.3.3. Blood versus tissue distribution of anti-ICAM/enzyme nanocarriers in mice

Bulk biodistribution of anti-ICAM/enzyme NCs was studied *in vivo* to evaluate the potential of this strategy for targeting compared to non-targeted enzymes. Previous work with anti-ICAM/ASM NCs had shown promise in distributing ASM through tissues, while the naked enzyme had rapidly cleared from circulation [41]. To evaluate the bulk distribution of enzyme in tissues or retention in circulation, mice were injected with anti-ICAM/¹²⁵I-enzyme NCs or non-targeted ¹²⁵I-enzyme. Blood from mice was collected at time of euthanization (30 minutes) and peripheral organs (heart, kidneys, liver, lungs, spleen) were harvested. Samples were measured with a gamma counter to detect the presence of ¹²⁵I-enzyme.

Again, while minimal NCs remaining in circulation by 30 minutes post-injection (~4.5%ID; Figure 29), majority of injected anti-ICAM/ α Gal NCs or anti-ICAM/GAA NCs were found in collected organs: 60.1 \pm 4.5%ID and 71.8 \pm 1.9%ID, respectively (Figure 29). The opposite was seen for non-targeted enzymes, with a large percentage of injected dose remaining in the circulation after 30 minutes after injection (~40.3%ID; Figure 29) and only ~17.0%ID in all collected tissues (Figure 29), which is an over-estimation since blood is

contained in organs. All in all, a marked ~4-fold difference in tissue was observed in the enzyme detected in all tissues, which indicates the contrast between targeted versus non-targeted enzyme.

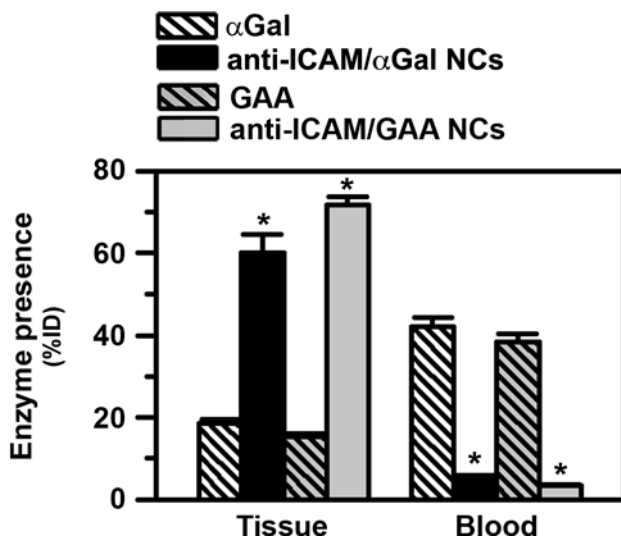


Figure 29. Enzyme distribution in tissue versus circulation in mice. ¹²⁵I-labeled enzyme was used to trace enzyme distribution. Mice were injected with either anti-ICAM/¹²⁵I-enzyme NCs or non-targeted ¹²⁵I-enzyme and blood and organs (heart, kidneys, liver, lungs, spleen) were collected 30 minutes post-injection. Enzyme presence was expressed as the percent of injected dose (%ID) remaining in blood or %ID collected from mouse organs. *p<0.01, comparing anti-ICAM/enzyme NCs to non-targeted enzyme, by Student's t-test. Data are mean±SEM. (Figure adapted from [47, 48])

4.3.4. Visualization of anti-ICAM nanocarriers in mice

We then imaged the pattern of biodistribution of anti-ICAM NCs injected i.v. in mice. For this purpose, nanocarriers consisted of green fluorescent nanoparticles coated with anti-ICAM and tracer amounts of NIR-labeled IgG, to allow co-visualization of both nanoparticle and coat components, respectively. Optical (fluorescence) imaging of the nanoparticle component showed clear and predominant accumulation of anti-ICAM NCs in lungs 30 minutes after i.v. injection, with lower accumulation in clearance organs such as the liver and spleen, whereas the opposite outcome was observed in the case of control IgG NCs (Figure 30a, b). Pulmonary accumulation (11.6-fold greater for anti-ICAM NCs over IgG NCs, Figure 30c) suggests specificity of targeting, since this organ contains a significant fraction (1/5–1/4) of the total vascular endothelium in the body, has relatively high ICAM-1 expression, and has first-pass exposure to i.v. injected materials [41]. This is in accord with

our previous studies showing pulmonary accumulation of anti-ICAM NCs ~14.2-fold over control IgG NCs in wild-type mice [203], but not in ICAM-1 knockout mice discussed below (11.4-fold below wild-type mice; Section 4.4.4.).

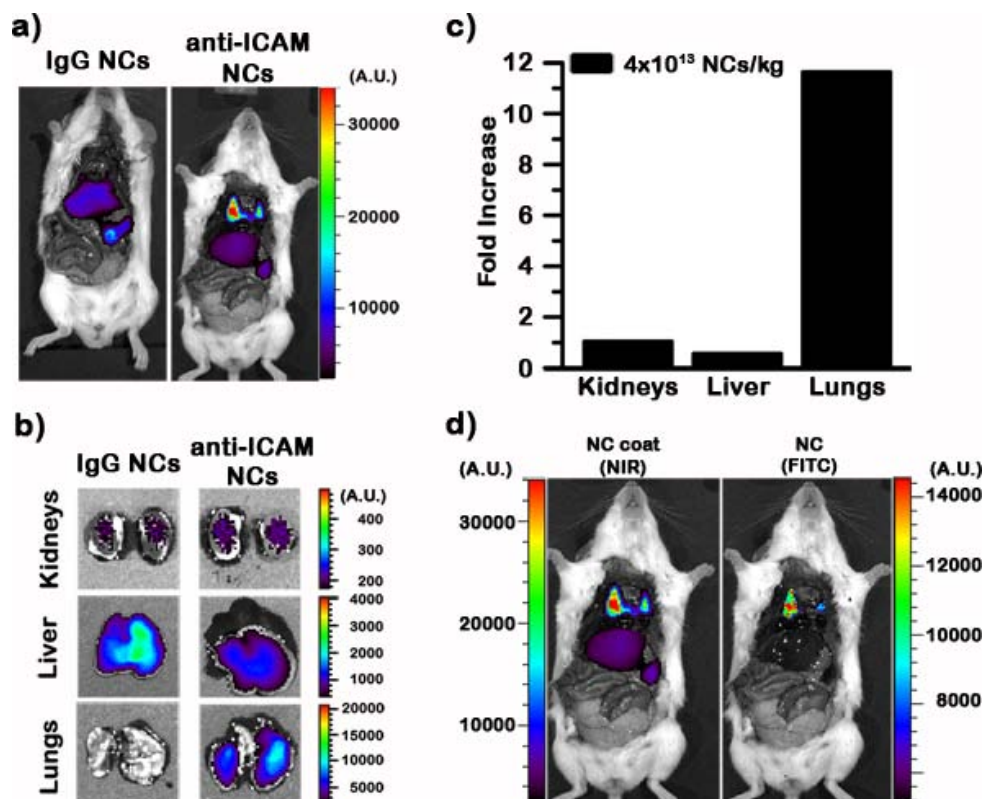


Figure 30. Visualization of specific targeting of anti-ICAM nanocarriers in mice. Optical imaging of (a) mice or (b) isolated organs 30 min after i.v. injection with green fluorescent nanocarriers (4×10^{13} NCs/kg) coated with control IgG or anti-ICAM labeled with FITC-analog (green fluorescent) and coated with either control IgG or anti-ICAM. (c) Semi-quantitative measurement of nanocarrier distribution, from optical imaging results shown in (b). (d) Visualization of anti-ICAM NCs consisting of green fluorescent nanoparticles coated with anti-ICAM and Alexa Fluor 750-labeled IgG as a near-infrared (NIR) tracer, revealing co-localization of both nanocarrier and coat counterparts in the lungs. (Figure adapted and reproduced from [50])

Hence, these results confirm specific and dose-dependent targeting by anti-ICAM NCs, in accord with previous studies showing a similar outcome when the targeting-antibody coat component was traced by ¹²⁵I-labeling [41, 203]. Optical imaging also showed lung co-

localization of the green fluorescent (FITC-analog) and NIR signals, which correspond to the nanocarrier particle and the antibody coat, respectively (Figure 30d). This confirms in vivo stability of the coat on the nanocarrier surface, validating previous works that show a similar result in models in vitro in Section 4.1.2. [48].

4.3.5. Biodistribution pattern and specificity of anti-ICAM/enzyme nanocarriers in mice

To confirm and quantify in vivo targeting by anti-ICAM/enzyme NCs, a closer examination of the presence of enzyme in each major organ was then conducted to evaluate the biodistribution pattern. This was achieved by using anti-ICAM/¹²⁵I-enzyme NCs. Specifically, peripheral organs, including the heart, kidneys, liver, lungs, and spleen, were examined. Due to its dense vasculature [206-208], high ICAM-1 expression [41], and the fact that they receive the whole cardiac output as a first pass, the lungs are a main target of ICAM-1-targeting strategies (e.g. $26.35 \pm 3.22\%ID$ of anti-ICAM NCs [41, 47, 157]). Anti-ICAM/ α Gal NCs and anti-ICAM/GAA NCs follow that similar pattern (Table 2). The lungs accumulated $36.24 \pm 3.47\%ID$ and $48.75 \pm 3.25\%ID$ of anti-ICAM/ α Gal NC and anti-ICAM/GAA NC, respectively. This is significantly higher than the second most accumulating organ, the liver, which is also very densely vascularized and expresses ICAM-1 while also serving as a clearance organ [41]. Nevertheless, the liver is a main target for many LSDs, e.g. PD [46]. This organ accumulated $18.41 \pm 1.22\%ID$ and $17.32 \pm 2.05\%ID$ of anti-ICAM/ α Gal NCs and anti-ICAM/GAA NCs accumulated in the liver. Instead, since non-targeted enzymes lack ICAM-1-specificity, neither non-targeted α Gal nor GAA accumulated in the lungs: $0.7 \pm 0.1\%ID$ and $1.0 \pm 0.1\%ID$, respectively (Table 2). As for the liver, since this is an RES organ, non-targeted α Gal and GAA accumulated moderately here: ($6.7 \pm 0.6\%ID$ and $9.7 \pm 0.8\%ID$, respectively; Table 2), although not as much as ICAM-1-targeted counterparts.

Table 2. Biodistribution of anti-ICAM/enzyme nanocarriers and non-targeted lysosomal enzyme in mice. (Adapted from [47])

	Blood	Heart		Kidney		Liver		Lung		Spleen	
	%ID	%ID	LR	%ID	LR	%ID	LR	%ID	LR	%ID	LR
<u>Non-targeted Enzyme:</u>											
ASM	31.56 ± 2.91	0.33 ± 0.02	0.18 ± 0.02	2.13 ± 0.15	0.41 ± 0.04	22.87 ± 2.55	1.19 ± 0.09	0.95 ± 0.09	0.33 ± 0.03	0.80 ± 0.06	0.46 ± 0.04
αGal	42.07 ± 2.22	0.49 ± 0.06	0.16 ± 0.01	10.12 ± 0.77	1.21 ± 0.06	6.68 ± 0.56	0.22 ± 0.01	0.74 ± 0.07	0.19 ± 0.02	0.40 ± 0.03	0.18 ± 0.01
GAA	38.40 ± 2.11	0.50 ± 0.05	0.17 ± 0.01	2.96 ± 0.07	0.40 ± 0.01	9.70 ± 0.77	0.37 ± 0.02	0.96 ± 0.13	0.27 ± 0.03	0.54 ± 0.03	0.30 ± 0.03
<hr/>											
<u>Anti-ICAM/enzyme NCs:</u>											
Anti-ICAM NC	4.71 ± 0.94	0.34 ± 0.04	1.31 ± 0.27	1.34 ± 0.07	2.05 ± 0.34	31.90 ± 3.58	13.33 ± 3.16	26.35 ± 3.22	81.54 ± 21.54	4.08 ± 0.48	19.50 ± 4.21
Anti-ICAM/ASM NC	6.94 ± 2.96	0.35 ± 0.02	1.64 ± 0.24	1.37 ± 0.05	2.07 ± 0.19	39.60 ± 2.81	17.31 ± 2.43	21.51 ± 2.73	63.61 ± 11.43	4.08 ± 0.37	23.24 ± 3.83
Anti-ICAM/αGal NC	5.59 ± 0.33	0.33 ± 0.04	0.80 ± 0.13	1.89 ± 0.14	1.69 ± 0.09	18.41 ± 1.22	4.66 ± 0.40	36.24 ± 3.47	66.95 ± 9.51	3.11 ± 0.43	9.57 ± 1.14
Anti-ICAM/GAA NC	3.32 ± 0.46	0.41 ± 0.03	1.91 ± 0.39	2.08 ± 0.18	3.49 ± 0.63	17.32 ± 2.05	8.42 ± 2.19	48.75 ± 3.25	159.74 ± 37.79	2.91 ± 0.27	20.00 ± 4.12

N/A = not applicable, no enzyme was loaded. %ID = percentage of injected dose. LR = localization ratio of %ID/g of tissue to %ID/g of blood. Data are mean±SEM, n≥5 mice (30 min after i.v. injection).

To account for density of accumulation in an organ, which allows us to compare organs of difference sizes, we normalized %ID per weight of the organ. The liver accumulated $12.36 \pm 0.71\%$ ID/g of anti-ICAM/ α Gal NCs and $12.80 \pm 1.65\%$ ID/g of anti-ICAM/GAA NCs, which represented is the third most densely accumulating organ, exceeded by the spleen ($25.69 \pm 2.78\%$ ID/g and $30.88 \pm 3.38\%$ ID/g) and the lungs ($175.3 \pm 21.4\%$ ID/g and $246.8 \pm 20.4\%$ ID/g). Interestingly, even though the liver and the spleen are RES organs, the accumulation could be due to a combination of targeting and clearance, since both non-targeted α Gal and GAA did accumulate in the liver and spleen but still to a lower level than anti-ICAM/enzyme NCs: $4.5 \pm 0.4\%$ ID/g and $7.0 \pm 0.4\%$ ID/g, respectively, in liver and $3.7 \pm 0.3\%$ ID/g and $5.7 \pm 0.4\%$ ID/g, respectively, in spleen.

We then normalized organ accumulation (%ID/g) to the circulating amount of enzyme, since the circulation levels are very different for anti-ICAM/enzyme NCs versus non-targeted enzyme, where the enzyme detected in an organ can be contributed by the circulating fraction in the case of circulating free enzyme. This parameter is called localization ratio (LR, Table 2) and represents more accurately enzyme retention in the tissue versus in blood. As expected, LR of lungs for anti-ICAM/ α Gal NCs (67.0 ± 9.5) and anti-ICAM/GAA NCs (159.7 ± 37.8) were significantly higher than their non-targeted counterparts (0.19 ± 0.02 and 0.27 ± 0.03 , respectively). This shows a specific enzyme delivery improvement by ICAM-1-targeting of 351.4- and 584.1-fold (specificity index, SI; Figure 31a) compared to the non-targeted enzymes, which is similar to previous work on anti-ICAM/ASM NCs (195.2-fold, [41]). Resultant LR of liver for anti-ICAM/ α Gal NCs (4.76 ± 0.51) and anti-ICAM/GAA NCs (8.42 ± 2.19) were also significantly higher than their non-targeted counterparts (0.22 ± 0.01 and 0.37 ± 0.02 , respectively). This indicates a 21.67-fold specific targeting enhancement (SI; Figure 31a) achieved by anti-ICAM/ α Gal NCs versus non-

targeted α Gal, and similarly by anti-ICAM/GAA NCs over non-targeted GAA (23.1-fold). Indeed, this shows that in addition to RES clearance, targeting of ICAM-1 can lead to specific accumulation in the liver. This is largely beneficial for treatment of LSDs, since the disease plagues all tissues, inclusive of vascular ECs. It is particularly beneficial for treatment of FD, a vasculopathy, and for PD, where liver is a target organ.

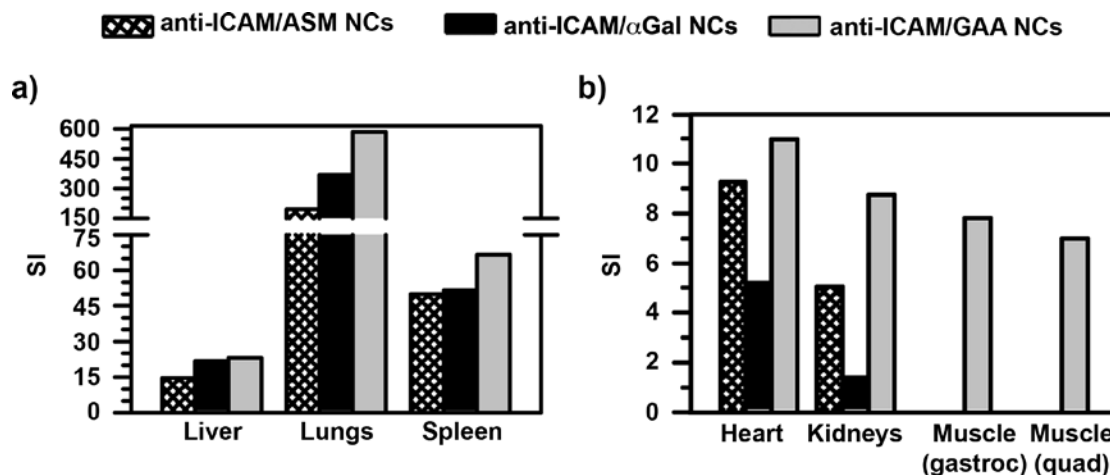


Figure 31. Specificity index of tissue targeting by anti-ICAM/enzyme nanocarriers versus non-targeted enzyme counterpart. Mice were injected with either anti-ICAM/ 125 I-enzyme NCs or 125 I-enzyme equivalent. Blood and organs were collected 30 minutes post-injection to measure 125 I-enzyme in a gamma counter. The specificity index (SI) was calculated as a ratio comparing the localization ratio (LR, %ID/g in tissue versus %ID/g in blood) of anti-ICAM/enzyme NCs to LR of non-targeted enzyme equivalent, depicting fold increase of enzyme presence in tissue as a result of ICAM-1-targeting compared to non-targeted enzyme. SI of (a) liver, lungs, and spleen and (b) heart, kidneys, gastrocnemius muscle, and quadriceps muscle.

Other important FD target organs are the kidneys and the heart, which portrayed a bulk accumulation of $1.89 \pm 0.14\% \text{ID}$ and $0.33 \pm 0.04\% \text{ID}$, respectively (Table 2), with a density $4.58 \pm 0.32\% \text{ID/g}$ and $2.12 \pm 0.32\% \text{ID/g}$, respectively, for anti-ICAM/ α Gal NC treatment. Even though the kidneys and heart were less densely targeted by anti-ICAM/ α Gal NCs than most other organs and apparently accumulated less anti-ICAM/ α Gal NCs than non-targeted α Gal ($24.6 \pm 1.5\% \text{ID/g}$ and $3.23 \pm 0.30\% \text{ID/g}$, respectively), significantly more α Gal

reached these tissues as a result of ICAM-1-targeting versus non-targeted α Gal since a good fraction of non-targeted α Gal detected was actually in the blood and not the tissue (SI of 1.41 and 5.06, respectively; Figure 31b). Additionally, the heart and skeletal muscles are key target organs for PD treatment. The heart accumulated anti-ICAM/GAA NCs at a density of $2.88 \pm 0.19\% \text{ID/g}$, compared to $3.30 \pm 0.23\% \text{ID/g}$ of non-targeted GAA. Yet, due to high retention of non-targeted GAA in the blood, resultant LR showed that anti-ICAM/GAA NCs accumulated better to this tissue versus non-targeted GAA (LR: 1.91 ± 0.39 versus 0.17 ± 0.01 ; Table 2). Indeed, GAA delivery to the heart was enhanced as a result of anti-ICAM NC, by an 11-fold increase. Additionally, enzyme delivery to the left gastrocnemius and left quadriceps were evaluated as examples of skeletal muscle tissue, which is difficult to reach and another main PD target. Specific targeting by anti-ICAM NCs improved delivery of GAA to these skeletal muscles by 7.8- and 7.0-folds (SI, Figure 31b). These results show that enzyme delivery can be enhanced by anti-ICAM NC platform, even to difficult to reach tissue.

All in all, enzyme delivery to all peripheral tissues tested was enhanced by ICAM-1-targeting compared to non-targeted delivery, with a difference from 1.4- to 67.8 for α Gal and 5.6- to 584.2-folds for GAA depending on the organ. This is somewhat similar to enhancement of ASM delivery to tissue, which was within a range of 5.1- to 195.2-fold enhancement. Interestingly, for some formulations, adding an enzyme cargo on the nanocarrier surface at the expense of displacing some targeting molecules seems to have increased targeting to certain tissues, e.g. anti-ICAM/ASM NCs improved delivery to the liver and spleen versus anti-ICAM NCs, and anti-ICAM/GAA NCs improves delivery to heart, lungs, and kidneys versus anti-ICAM NCs (LR, Table 2). Yet, this was not the case for anti-ICAM/ α Gal NC. Also interestingly, amongst the three enzymes, anti-ICAM NCs provided the least α Gal delivery enhancement to the heart and kidneys, while nanocarriers

provided greatest GAA delivery enhancement to the all tissue except the brain (this will be discussed in further detail in Section 4.3.6.). This correlates well with cell culture studies showing internalization efficiency of anti-ICAM/GAA NCs to be the greatest amongst the three preparations, even with the least number of targeting moieties on the surface (Table 1). All in all, these results show that each individual enzyme cargo may elicit similar biodistribution pattern but achieve varying degrees of delivery improvement compared to the non-targeted enzyme. Yet, since all tissues are affected in LSDs, delivery enhancement by ICAM-1-targeting show potential in improving enzyme delivery to all tissues, especially target organs.

4.3.6. Brain targeting of anti-ICAM/enzyme nanocarriers in mice

Many LSDs manifest neuropathy and/or neurodegenerative symptoms [16], hence, treatment must also be delivered to the brain, which requires targeting and traversing across the BBB. Cell culture work showed promise in delivering anti-ICAM NCs across cell barriers [43], including the BBB as shown in the previous chapter [49]. Hence, we studied the potential of anti-ICAM NCs to deliver lysosomal enzymes to the brain in mice.

Previous work showed that $0.27 \pm 0.05\% \text{ID}$ of anti-ICAM/ASM NCs reached th brain (Muro, unpublished results). In this work we also found that $0.13 \pm 0.01\% \text{ID}$ of anti-ICAM/ α Gal NCs and $0.15 \pm 0.01\% \text{ID}$ of anti-ICAM/GAA NCs also reached this organ (Figure 32a). Density of brain accumulation was $0.65 \pm 0.13\% \text{ID/g}$ for anti-ICAM/ASM NCs, $0.28 \pm 0.02\% \text{ID/g}$ for anti-ICAM/ α Gal NCs, and $0.32 \pm 0.03\% \text{ID/g}$ for anti-ICAM/GAA NCs (Figure 32b).

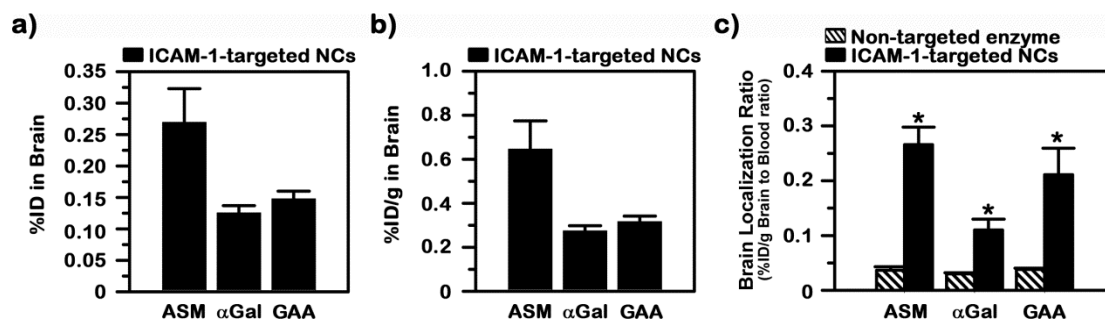


Figure 32. In vivo brain accumulation and specificity of anti-ICAM/enzyme nanocarriers. Mice were injected (a, b, c) with anti-ICAM NCs carrying ^{125}I -radioisotope labeled ASM, αGal , or GAA or (c) with non-targeted ^{125}I -enzyme counterparts. Blood samples and the brain were collected 30 minutes post-injection and analyzed for ^{125}I content. (a) Percent of injected anti-ICAM/enzyme NC dose (%ID) found in brain tissue. (b) %ID normalized to the weight of the organ (%ID/g) showing the density of accumulation in the brain tissue. (c) Brain localization ratio (LR) was calculated by comparing %ID/g of brain tissue to %ID/g of blood. Data are mean \pm SEM. * $p < 0.05$, comparing enzyme delivered ICAM-1-targeted NCs to non-targeted enzyme, by Student's t-test.

To account for free enzyme in circulation, the LR was calculated as in the previous section (ratio of %ID/g in tissue versus %ID/g in blood) which was 0.27 ± 0.03 , 0.11 ± 0.02 , and 0.21 ± 0.05 for anti-ICAM/ASM NCs, anti-ICAM/ αGal NCs, and anti-ICAM/GAA NCs, respectively (Figure 32c). By comparing the LR of anti-ICAM/enzyme NCs versus non-targeted enzyme, the specificity index (SI) can be determined, defining the specific enhancement provided by ICAM-1-targeting. Targeting ICAM-1 specifically enhanced delivery of ASM, αGal , and GAA to the brain by 7.2-, 3.9-, and 5.6-fold, respectively, after a single injection. This is in line with other difficult to reach tissues previously discussed (see Section 4.3.5.).

Therefore, all three formulations of anti-ICAM/enzyme NCs accumulated efficiently to the brain, although at different levels. Interestingly, amongst the three types of anti-ICAM/enzyme NCs, delivery of ASM to the brain seemed the most efficient, ~2-folds greater than αGal and GAA, perhaps due to ASM binding to abundant sphingomyelin in this organ.

This is particularly favorable for NPD, as the neuropathy is most severe in this disease compared to FD or PD. Although, in comparison to other organs, the total amount of anti-ICAM/enzyme NCs to reach the brain may seem trivial (Figure 32 versus Table 2), this strategy seems to be more efficient compared to other targeting methods, such as targeting transferrin receptors (TfR) [162], a favorable and well studied method of brain delivery. In fact, ICAM-1-targeting enhanced ASM delivery to the brain 2.5-fold greater than the enhancement provided by ASM targeted to transferrin receptors [162].

4.3.7. Visualization of anti-ICAM/enzyme nanocarriers in the brain of mice

Both cell culture studies on BBB transport and in vivo brain accumulation showed the ability of anti-ICAM NCs to target the brain. To examine in detail the distribution of green fluorescent anti-ICAM/¹²⁵I-enzyme NCs in regions of the brain, this organ was collected 30 minutes after i.v. injection and was then divided into eight sections and measured for ¹²⁵I-enzyme content, and green fluorescent NCs were visualized by optical fluorescence imaging. NCs and enzyme were observed throughout the brain, with a greater accumulation toward the caudal region, especially the cerebellum (Figure 33).

Even though the whole brain is highly vascularized, the cerebellum seems to be more dense with capillaries than any other region of the brain [209, 210]. Hence, circulating anti-ICAM NCs have the opportunity to target and traverse the vast surface area provided by the vascular endothelial cells. In case of treating NPD, the cerebellum is known to be particularly vulnerable, hence delivery to purkinje cells of the cerebellum would be optimal [211]. Additionally, since PD also severely affects muscles, delivery of enzyme to smooth muscles in the brain vasculature may relieve symptoms seen in these tissue, e.g. rupturing of aneurysms [46, 212], of which anti-ICAM NCs do target. Also, significant glycogen storage

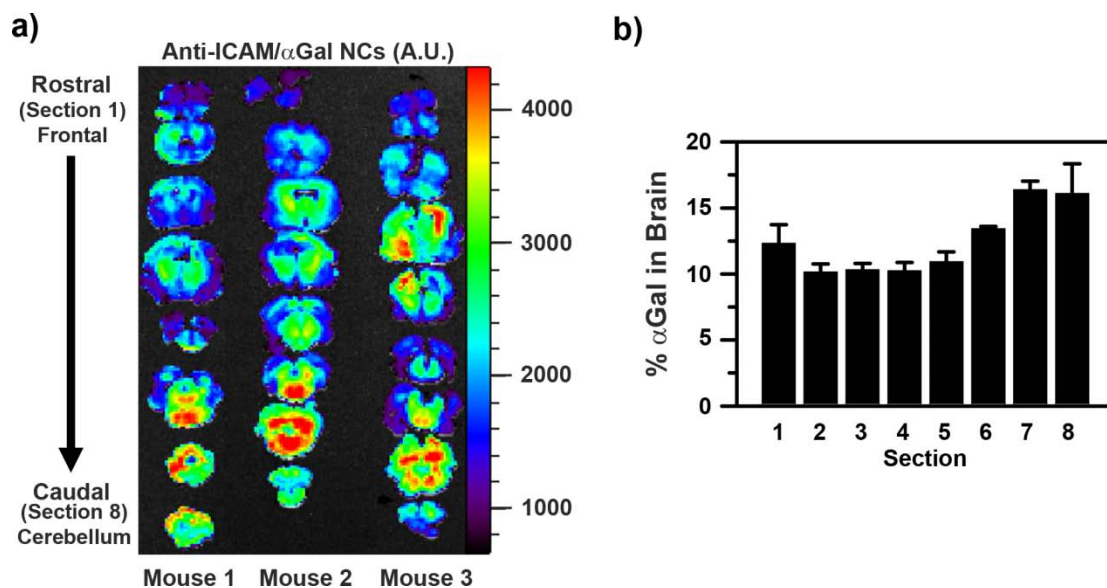


Figure 33. Distribution of anti-ICAM/enzyme nanocarriers in brain of mice. Green fluorescent NCs were coated with anti-ICAM/ ^{125}I - αGal (50:50 antibody to enzyme mass ratio) to formulate anti-ICAM/enzyme NCs. Mice were injected with anti-ICAM/ ^{125}I - αGal NCs (2.4×10^{13} NCs/kg) and euthanized 30 minutes post-injection. Brains were collected and sliced into 8 coronal sections. Sections were imaged, analyzed for ^{125}I content, and weighed. (a) Fluorescence image of nanocarriers in sectioned brain samples. (b) Percent of αGal in each section relative to the total αGal targeted to the brain tissue. Data are mean \pm SEM.

has been reported in neurons of the cerebellum of PD patients which exhibit motor control issues [213, 214]. Hence, since motor control is affected in PD and is likely due to excess glycogen storage in the cerebellum, the region of the brain that coordinates and fine-tune movement, treatment to this region would be beneficial. All in all, targeting ICAM-1 to deliver ERT for neuropathic LSDs could prove to be optimistic, especially in treating the cerebellar region of the brain.

4.3.8. Tissue retention of anti-ICAM/enzyme nanocarriers in mice tissue

The results discussed above indicate enhanced targeting of lysosomal enzymes to both peripheral organs and the CNS by targeting ICAM-1. To verify strong association with

tissues with transport into tissues we performed similar injections followed by intravascular perfusion, which would eliminate the circulating fraction and that loosely bound to the vascular endothelium. As shown in Figure 34, intravascular perfusion did not result in release of nanoparticles accumulated in organs (Figure 34a); in fact, an average of $98.2 \pm 11.9\%$ ID relative to %ID of non-perfused tissue was retained. The heart retained the least amount and yet this was 81% of non-perfused heart, while the kidneys increased in α Gal targeting (136% of non-perfused tissue; Figure 34a), perhaps through forced perfusion lingering anti-ICAM/ α Gal NCs passed through the kidneys allowing for increased binding. This increase shows the potential for kidneys to accumulate more anti-ICAM/ α Gal NCs than the allotted amount retained by 30 minutes.

At 24 hours post-injection, anti-ICAM/ α Gal NCs were still present in tissue, although the particular amount had shifted slightly (Figure 34b). For instance, about 60% of the lung fraction of anti-ICAM/ α Gal NCs was removed from the organ by 24 hours after injection, in part which appeared in the liver and spleen, as traced by fluorescence (Figure 34b). Similarly, by 24 hours 60% of residual α Gal in lungs was also re-distributed in part to the liver and spleen (increase of 10-22%; Figure 34c), as traced by ^{125}I - α Gal. This is in contrast to previous results showing lung retention of 75% anti-ICAM NCs [215] and may be due to either lower affinity binding of anti-ICAM/ α Gal NCs carrying lower anti-ICAM surface density and/or rapid metabolism of nanoparticles bearing a lysosomal enzyme by pulmonary endothelial cells. In any case, the fraction of anti-ICAM/ α Gal NCs retained in the lung still represented a 150-fold enhancement in the amount of enzyme delivered to this organ compared to non-targeted α Gal.

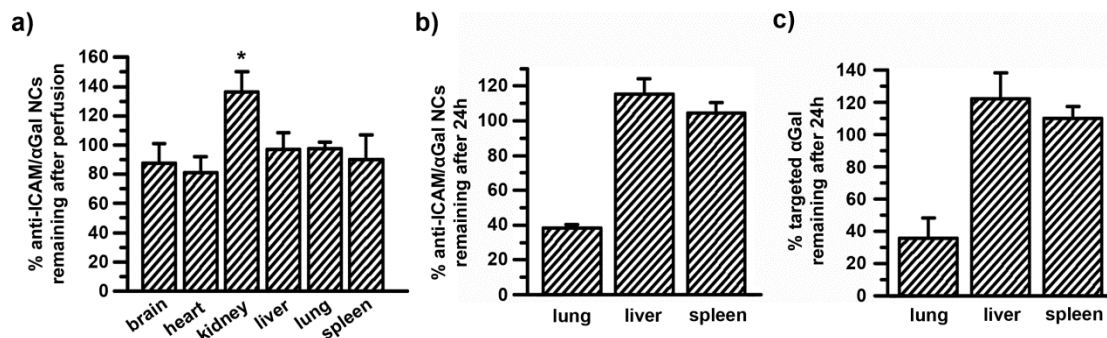


Figure 34. Anti-ICAM/ α Gal nanocarriers target and remain in tissue. (a) Mice injected with anti-ICAM/ 125 I- α Gal NCs were perfused at 30 minutes. Data shows relative quantity of anti-ICAM/ α Gal NCs remaining in perfused organs as a percent of non-perfused organs. * $p < 0.05$, comparing perfused tissue to non-perfused tissue, by Student t-test. (b) Green fluorescent anti-ICAM/ α Gal NCs were injected into mice, which were then perfused at 30 minutes or 24 hours after injection. The amount of anti-ICAM/ α Gal NCs remaining in perfused tissue after 24 hours was assessed via fluorescence microscopy and compared to that of perfused organs harvested at 30 minutes. (c) Mice were perfused at 30 minutes or 24 h post-injection of anti-ICAM/ 125 I- α Gal NCs. Relative 125 I- α Gal remaining per organ by 24 hours was calculated as percent of 125 I- α Gal detected at 30 minutes. Data are mean \pm SEM. (Figure reproduced from [48])

4.3.9. Conclusion

In the previous two sections we discussed the potential of improving enzyme delivery for treatment of LSDs by using anti-ICAM NCs to enhance binding, internalization, and intracellular delivery of lysosomal enzymes to lysosomes of disease-model cells to alleviate substrate accumulation. We also discussed the potential of anti-ICAM NCs to improve transport across the BBB to target cells of the brain. Pairing well with cell culture results, in vivo work showed mice treated with anti-ICAM/enzyme NCs rapidly cleared enzyme from circulation and majority of enzyme was found to target tissue within 30 minutes, while non-targeted enzyme lingered in circulation with little bound to tissue. This was indicative of fast targeting of enzyme to tissue by ICAM-1-targeted nanocarriers. Indeed, previous work has shown that anti-ICAM/ASM NCs can enhance delivery of enzyme to tissue in vivo as a treatment model for NPD [41]. Here, we showed that this phenomenon was not unique to

ASM and translatable to two other lysosomal enzymes, α Gal and GAA for treatment of FD and PD. As a result, delivery of all three enzymes to all tissues of mice was enhanced by ICAM-1-targeting systems compared to non-targeted enzyme treatment counterparts, although with unique ranges of improvement. Delivery of GAA was most effectively enhanced to all organs by anti-ICAM NCs, compared to other anti-ICAM/enzyme NC systems. We note that perhaps this effect is seen in the tissue due to a synergistic effect between the ICAM-1-targeting antibody and the enzyme, unique to the combination that is not present or distinguishable in cell culture. Regardless of variance, successful enhancement of enzyme delivery demonstrates the potential of using ICAM-1-targeted delivery systems for LSD treatment by ERT delivery.

In agreement with peripheral organs, in vivo works showed promise in enhancing enzyme delivery to the brain as well. Anti-ICAM/enzyme NCs were ~4- to 7-folds more effective in delivering lysosomal enzyme to the brain than non-targeted enzyme counterparts within 30 minutes of administration. Moreover, a closer examination illustrated by delivery of α Gal that the enzyme accumulated preferentially to the cerebellum, the region notably affected by NPD and other LSDs. This rapid accumulation to the brain shows the potential for anti-ICAM NCs to improve brain delivery of lysosomal ERTs.

4.4. Enhancement of enzyme delivery by modulation of ICAM-1-targeted nanocarriers

4.4.1. Introduction

Previous sections have focused on the applicability of anti-ICAM/enzyme NCs to be extended to other lysosomal enzymes aside from the previously examined ASM enzyme. Additionally, we also examined if anti-ICAM NCs could be used to improve delivery to the brain. Given positive results indicative of the potential for anti-ICAM NCs to improve ERT delivery for treatment of LSDs, we then examined how modulation of nanocarrier parameters can enhance enzyme delivery further. In particular, we evaluated the influence of two parameters: variation of the coat and the bulk nanocarrier concentration.

Previous work has examined the effects of these variables in the biodistribution of anti-ICAM NCs [44]. Specifically, results showed that increasing the density of anti-ICAM on the surface of nanocarriers or increasing the concentration of anti-ICAM NCs injected increases shifts the biodistribution from high accumulation in liver and spleen to high accumulation to lungs, and low accumulation in the liver and spleen [44]. However, it was unknown whether the presence of a cargo on the nanocarrier surface may further impact biodistribution, particularly in the case of lysosomal enzymes because they typically have residues targeting the M6PR [216]. Since both the targeting moiety and the cargo is coated on the nanocarrier surface, we evaluate whether shifting the targeting avidity to increase cargo load could affect targeting efficacy and biodistribution of anti-ICAM/enzyme NCs. Additionally, it is well known that binding interactions depend on the ligand-receptor concentration and, thus, by increasing the bulk-concentration of anti-ICAM/enzyme NCs administered may potentially vary the biodistribution pattern.

4.4.2. Visualization of dose-dependent targeting of anti-ICAM nanocarriers in mice

As shown in Section 4.3.4. above, we first visualized the biodistribution of anti-ICAM NCs injected i.v. at different doses, using optical imaging. Figure 35 shows that accumulation of anti-ICAM NCs over the level of control IgG NCs in lungs and kidneys was dose-dependent: e.g., 11.6-fold and 26.4-fold enhancement when using 4×10^{13} versus 8×10^{13} NCs/kg, respectively, in the case of lungs. The observed linear dependence in targeting of both organs suggests that binding saturation has not been reached at the doses tested. In contrast, liver accumulation of anti-ICAM NCs was consistently lower (0.6-fold) compared to IgG NCs.

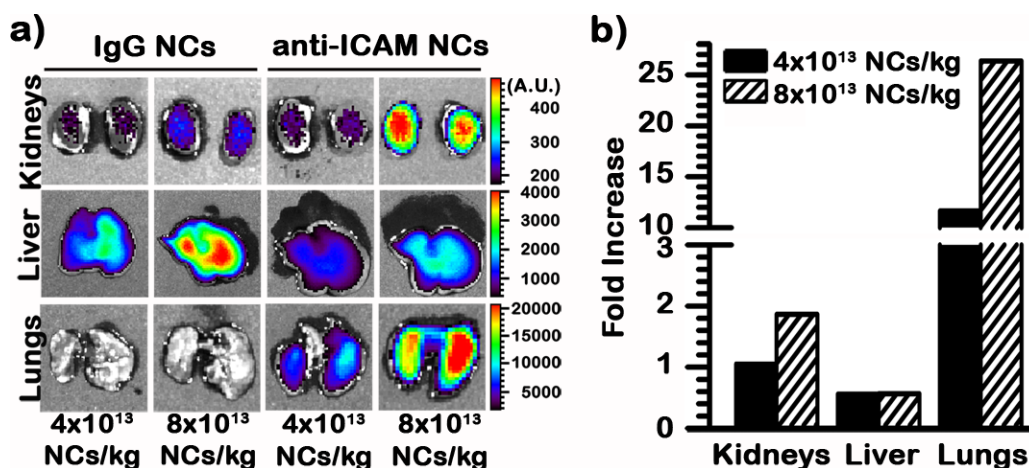


Figure 35. Visualization of dose-dependent targeting of anti-ICAM nanocarriers in mice. Optical imaging of isolated organs of mice 30 minutes after i.v. injection with model nanocarriers (4×10^{13} or 8×10^{13} NCs/kg) labeled with green fluorescent and coated with either control IgG or anti-ICAM. (b) Semi-quantitative measurement of nanocarrier distribution, from optical imaging results shown in (a). (Figure reproduced from [50])

4.4.3. Comparative tissue versus blood re-distribution of anti-ICAM/enzyme nanocarriers

We next focused on examining in more detail the effect of varying bulk nanocarrier dose and also the coated antibody surface density on the biodistribution of anti-ICAM/enzyme NCs. We prepared three different anti-ICAM/ α Gal NC formulations by varying (1) targeting antibody to enzyme cargo ratio, or (2) nanoparticle bulk-concentration, to examine the impact

of these variations on the in vivo biodistribution of the lysosomal enzyme (Figure 36). For two formulations, the surface-density of anti-ICAM-to- α Gal was varied from ~95:5 to 50:50 mass ratio, which rendered an enzyme load of ~50 versus 500 α Gal molecules/NC. These formulations were injected at a concentration of 1.6×10^{13} NCs/kg, which represents final enzyme doses of ~45 (low) versus 449 (intermediate) α Gal μ g/kg. In the “high dose”, the coating was maintained at a 50:50 anti-ICAM-to- α Gal mass ratio (as is in the “intermediate dose”), yet the concentration of the injected dose was varied to 2.4×10^{13} NCs/kg (1.5-folds greater than low and intermediate dose), which represents a final enzyme dose of ~550 (high)

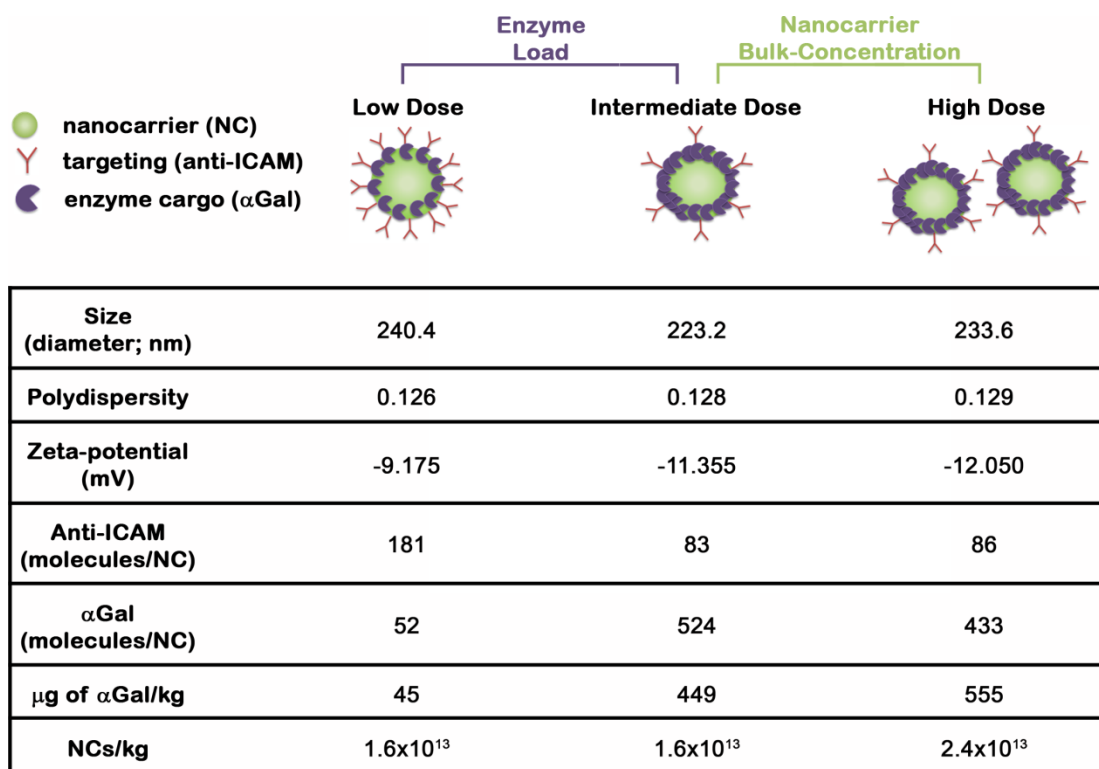


Figure 36. Anti-ICAM/ α Gal nanocarriers formulations. Model 100-nm diameter, polystyrene nanoparticles were coated with anti-ICAM as a targeting moiety and α Gal as an enzyme cargo. Three formulations were prepared by varying the antibody-to-enzyme ratio on the nanoparticle surface or the final concentration of nanoparticles in solution, as indicated. These variations rendered three different enzyme doses: low, intermediate, or high. The size, polydispersity, zeta potential, surface coating, and nanoparticle bulk-concentration of these formulations are provided. (Figure reproduced from [50])

α Gal $\mu\text{g}/\text{kg}$ (Figure 36). For all formulations, the size, polydispersity, and zeta-potential of the resulting nanoparticles was similar, ranging between 223 to 240 nm in diameter, 0.126 to 0.129 polydispersity, and from -9.12 to -12.0 mV (Figure 36).

All three anti-ICAM/ ^{125}I - α Gal NC formulations or equivalent doses of non-targeted ^{125}I - α Gal were administered separately into mice to examine their overall biodistribution after i.v. injection. In all three cases, anti-ICAM/ α Gal NCs rapidly disappeared from the circulation, while free α Gal remained in blood to a much greater extent (Figure 37a, b), consistent to previously discussed enzyme delivery enhancement patterns. For instance (Figure 37c), 30 min after injection, the level of α Gal in circulation associated with anti-ICAM NCs ranged from ~2 to 6% ID, contrasting with ~40 to 60% ID of free α Gal, a ~10-fold decrease in circulation of anti-ICAM/ α Gal NCs compared to the naked enzyme. Additionally, anti-ICAM/ α Gal NCs accumulated in tissues at a greater extent than naked α Gal (Figure 37d). Considering collectively the major organs of the body (brain, heart, kidneys, liver, lungs, and spleen), ICAM-1 targeting resulted in tissue accumulation ranging from ~60 to 70% ID, compared with only ~20% ID in the case of the free enzyme. This represents ~3.5-fold increase of global tissue distribution as a result of ICAM-1 targeting. This level of enhancement still underestimates the targeting potential of anti-ICAM NCs, because the circulating enzyme level is significantly higher for naked α Gal (Figure 37c), and this circulating fraction also contributes to the level of enzyme detected in each organ. This result is comparable and pairs well with previously discussed work (Figure 29, Section 4.3.3.) where anti-ICAM/ASM NCs for NPD and anti-ICAM/GAA NCs for PD were prepared similarly to the low dose α Gal formulation described here [41, 47].

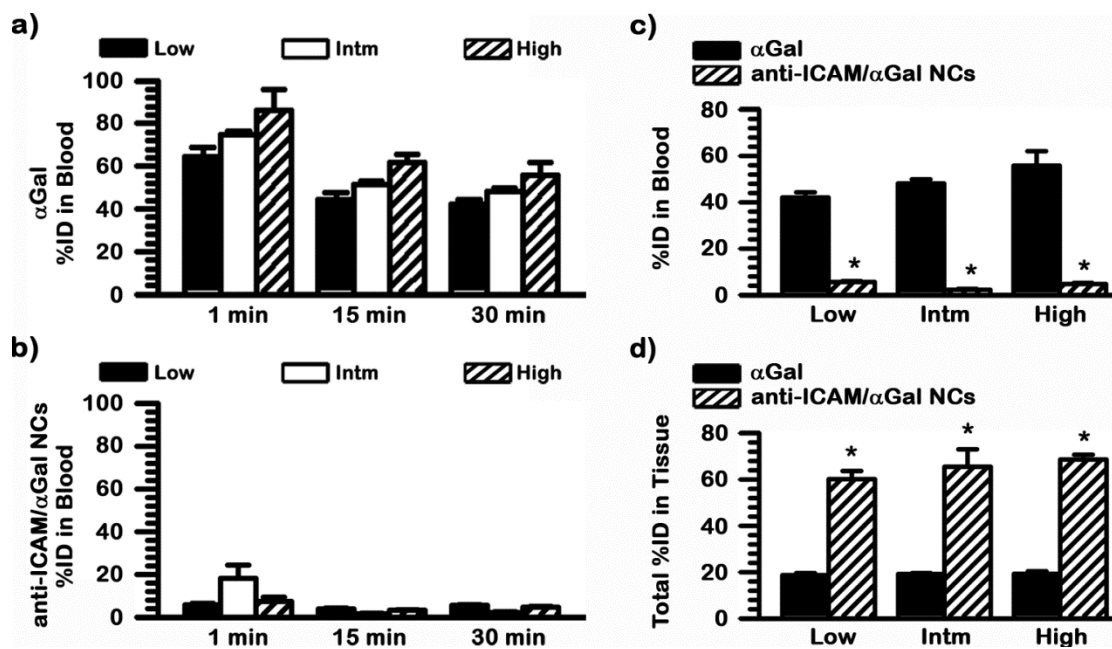


Figure 37. Presence of non-targeted α Gal versus anti-ICAM/ α Gal nanocarriers in circulation and tissue. Non-targeted ^{125}I - α Gal or anti-ICAM/ ^{125}I - α Gal NCs were injected i.v. in mice. Blood samples collected at 1, 15, and 30 minutes post-injection and major organs (brain, heart, kidney, liver, lungs, and spleen) collected at 30 minutes post-injection were measured for ^{125}I - α Gal content to determine percent of total injected dose (%ID) remaining in circulation or tissues. (a, b) %ID remaining in circulation over time of mice injected with (a) non-targeted ^{125}I - α Gal or (b) anti-ICAM/ ^{125}I - α Gal NCs. (c,d) %ID in (c) circulation or (d) all collected tissue by the 30 minute endpoint. Intm = Intermediate dose. Data are mean \pm SEM. Comparison by Student's t-test of each anti-ICAM/ α Gal NC formulation to its naked α Gal counterpart rendered $p < 0.001$. (Figure reproduced from [50])

With regard to comparing the global targeting efficacy (cumulative %ID in all organs) of the different anti-ICAM/ α Gal NC formulations, the amount of targeting anti-ICAM on the nanoparticle surface was reduced by half (from 181 to 83 molecules per particle; Figure 36) when increasing the enzyme load by 10-fold (low and intermediate α Gal doses). This is in line with the size difference between these molecules, e.g., ~150 kDa for anti-ICAM versus ~32.25 kDa for the α Gal form used. However, despite this variation of surface-density of the targeting coat, as well as the change concerning nanoparticle-bulk concentration (from 1.6×10^{13} to 2.4×10^{13} NCs/kg), no statistically significant differences were observed, and all formulations cause a similar blood-to-tissue shift of the enzyme.

4.4.4. Effects of varying targeting surface-density or nanocarrier bulk-concentration on enzyme distribution in vivo

We next evaluated whether modification of these design parameters led to changes in the biodistribution pattern of anti-ICAM/ α Gal NCs. Very few changes were found concerning different antibody surface-densities (low versus intermediate α Gal doses; 45 versus 449 μ g α Gal/kg), which occurred in the liver (figure 38). For instance, a 2-fold reduction of the antibody surface-density on the nanocarrier coat resulted in an increased liver accumulation of α Gal from \sim 12 to 24%ID/g (Figure 38b). This seems to reflect reduced targeting, which is only noticeable (yet not statistically significant) in the brain, possibly due to the low magnitude of targeting to this organ compared to others. Instead, the cumulative effect of small reductions in targeting through the body was noticed in the liver, likely due to non-specific clearance. In accord, coating of α Gal alone on the surface of nanocarriers lead to an even more enhanced liver accumulation ($53.4\pm 2.6\%$ ID; data not shown), which is a characteristic clearance pattern for particulate objects of this size range [158].

However, varying anti-ICAM surface density did not cause significant changes in the levels of enzyme accumulation in other organs, which represent FD targets. For example, the lungs accumulated the highest dose of anti-ICAM/ α Gal NCs for all formulations (\sim 35%ID; Figure 38a). This was also the case after normalization by organ weight, with \sim 180%ID/g (Figure 38b). This suggests endothelial specificity, validated by the fact that control IgG NCs or α Gal NCs did not accumulate in the lungs ($1.6\pm 0.3\%$ ID and $0.9\pm 0.1\%$ ID, respectively; data not shown) and this was also the case for anti-ICAM NCs injected in ICAM-1 knockout mice ($2.0\pm 0.3\%$ ID; data not shown). Kidneys and heart accumulated \sim 2%ID and \sim 0.3%ID α Gal, equivalent to \sim 5%ID/g and \sim 2%ID/g of the enzyme, respectively, regardless of the variation in the antibody surface density.

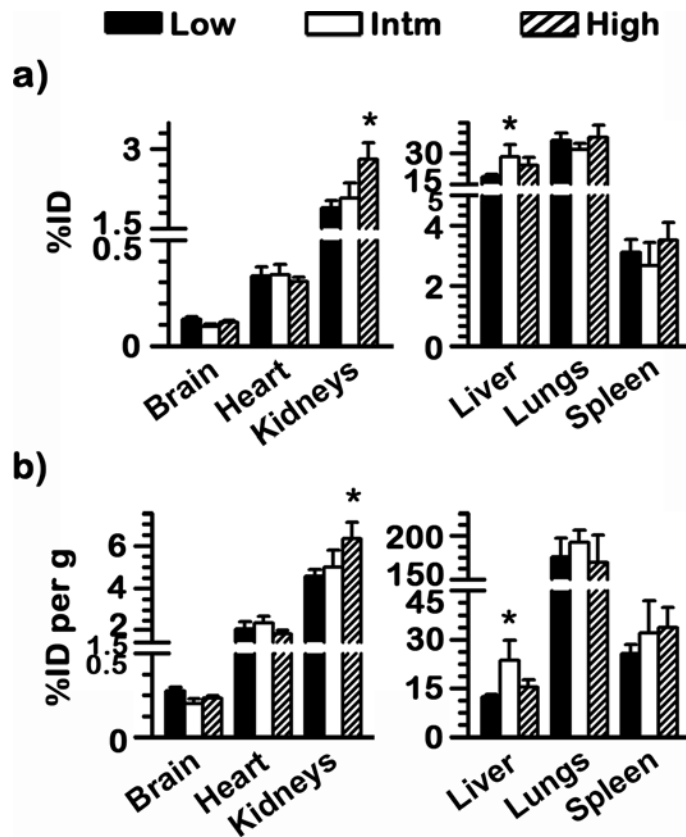


Figure 38. Similar α Gal biodistribution with varying the design parameters of anti-ICAM nanocarriers. Mice were injected i.v. with 1.6×10^{13} NCs/kg of anti-ICAM/ 125 I- α Gal NCs prepared to contain 95:5 or 50:50 antibody-to-enzyme surface-density ratios (52 versus. 524 α Gal molecules/NC), which rendered low (45 μ g/kg) or intermediate (Intm; 449 μ g/kg) α Gal doses. In addition, anti-ICAM/ 125 I- α Gal NCs displaying 50:50 antibody-to-enzyme surface-density ratios was injected at 2.4×10^{13} NCs/kg (high α Gal dose; 555 μ g/kg). Organs were harvested 30 minutes after injection, weighed, and measured for 125 I content to determine (a) percent of total injected α Gal dose (%ID) in each organ and (b) relative tissue-to-blood targeting efficiency as %ID α Gal per gram of tissue (%ID/g) to compare among organs of different size. Data are mean \pm SEM. * $p < 0.05$, comparing to low α Gal doses, by Student's t-test. Comparing intermediate and high α Gal doses rendered $p > 0.1$, by Student's t-test. (Figure reproduced from [50])

These findings are consistent with previous results demonstrating no significant changes in the pulmonary biodistribution of cargo-free anti-ICAM NCs, along with an enhanced accumulation in the liver, when antibody surface-densities varied between 55 and 165 molecules/NC [44] (surface-densities in this study are 83 versus 181 antibodies/NC). Perhaps at this range of antibody surface density, nanocarrier particles already surpass the

avidity threshold that allows them to effectively bind to the target in vivo, and this makes it possible for the enzyme cargo to occupy the nanocarrier coat without impairing binding. Minimal retention in circulation described above (Figure 37) indeed suggests rapid targeting.

In addition, no changes were observed by varying the carrier-bulk concentration within the range tested, corresponding to intermediate versus high α Gal doses; 449 versus 550 μ g α Gal/kg (note that the statistical significance associated with high dose in Figure 38 is compared to low dose, which also encompasses different targeting surface density). The lack of biodistribution changes observed here regarding variation of the nanocarrier bulk-concentration is opposite to the outcome reported for cargo-free anti-ICAM NCs [44]. However, these differences may be due to the different nanocarrier concentrations used in these two studies: 1.6×10^{13} and 4.8×10^{13} NC/kg (a 3-fold change) employed in a previous work versus 1.6×10^{13} and 2.4×10^{13} NC/kg in this report, where the 1.5-fold concentration change may have been insufficient to cause targeting differences. This outcome may have been also affected by the allegedly lower avidity of nanocarriers used in this comparison, which displayed ~ 85 anti-ICAM molecules/NC versus 209 anti-ICAM molecules/NC reported previously [44].

Interestingly, the relative extent of targeting versus clearance, exemplified by accumulation of anti-ICAM NCs in the lungs versus liver, is significantly different between cargo-free [44] and α Gal-containing counterparts shown here. For instance, in a previous work, pulmonary accumulation of cargo-free anti-ICAM NCs displaying 55 versus 165 antibody molecules/NC was 56%ID/g versus 63%ID/g, respectively, compared to 48%ID/g versus 46%ID/g for the liver [44]. In contrast, in this study using anti-ICAM/ α Gal NCs displaying 83 versus 181 antibodies/NC, pulmonary accumulation was 192%ID/g versus 175%ID/g, respectively, compared to 24%ID/g versus 12%ID/g for the liver (Figure 38b). It

thus appears that targeting of α Gal-loaded anti-ICAM NCs is enhanced. This could be due to relative differences between the anti-ICAM batch used and/or the presence of the enzyme on the nanocarrier coat, which could have conferred enhanced avidity. This is possible because most lysosomal enzymes display mannose or M6P residues that can interact with their receptors and also α Gal can interact with glycosphingolipid ligands on the cell surface [216, 217]. In particular, pulmonary accumulation of α Gal NCs was negligible ($0.9\pm 0.1\%$ ID; data not shown) and similar to that of control IgG NCs ($1.6\pm 0.3\%$ ID; data not shown), indicating a synergistic rather than additive effect. It is likely that avidity of multivalent α Gal is still relatively low as to confer relevant targeting by itself, yet after initial binding to the endothelium via ICAM-1, additional α Gal interactions may occur. Similar effects have been observed for strategies where one nanocarrier particle is targeted to multiple receptors [44, 218]; yet in this study the cargo, not a second targeting moiety, would provide this ability.

4.4.5. Specificity and absolute enzyme delivery by anti-ICAM nanocarriers

All anti-ICAM NC formulations resulted in similar overall shift α Gal from the blood to tissues (Figure 37), with a similar relative biodistribution in organs (Figure 38). Since dose may also affect the biodistribution of naked α Gal, we next examined the specificity offered by ICAM-1-targeting. This was achieved by determining the effect of varying antibody surface-density on the nanocarrier particle or the nanocarrier bulk-concentration (described above) on the specificity index (SI) of anti-ICAM/ α Gal NCs over non-targeted α Gal, which corrects for the different circulating fractions in these formulations (see Methods).

For all three formulations, SI was greater than 1 in all organs tested, reflecting a specific increase on enzyme targeting as a result of coupling it to anti-ICAM NCs, across

variations of the injected enzyme dose from ~45 to 555 $\mu\text{g}/\text{kg}$ (Figure 39a). Counter-intuitively, the formulation displaying a greater targeting specificity in each organ was the one with reduced antibody surface-density and nanocarrier bulk-concentration (intermediate αGal dose of 449 $\mu\text{g}/\text{kg}$). For this formulation, anti-ICAM NCs enhanced specific targeting of αGal from 4-fold (in kidneys) up to 981-fold (in lungs) over the equivalent naked counterpart. This could be explained if the range of anti-ICAM surface-density used in this study already surpassed the threshold for effective targeting in vivo, and αGal presented on the nanocarrier surface could provide a synergistic targeting effect, as discussed above.

A reduced enhancement in tissue targeting specificity was seen when varying nanocarrier bulk-concentration between 1.6×10^{13} and 2.4×10^{13} NCs/kg. Judging by the similar biodistribution (Figure 38) but not specificity (Figure 39) patterns observed for these two formulations, it appears a change in the nanocarrier concentration within this range does not impact binding in the case of high-avidity multivalent anti-ICAM/ αGal NCs. Instead, it is plausible that such a change in concentration enhances binding of allegedly low-avidity, monovalent naked αGal . If this was the case, the outcome would be a decreased SI for anti-ICAM/ αGal NCs, as observed. Nonetheless, even in this situation ICAM-1 targeting offered a marked and significant enhancement in the specific tissue accumulation of αGal , with SI values ranging from 3.5 to 496 for high dose, observed in the kidneys and lungs, respectively.

Importantly, modulation of either antibody surface density or nanocarrier bulk-concentration both resulted in an increase in the absolute amount of αGal accumulated in each organ (Figure 39b). Since variation of these nanocarrier design parameters did not negatively or significantly impact the potential for ICAM-1 targeting through the body, the increasing dose of αGal carried by these three formulations resulted in a corresponding

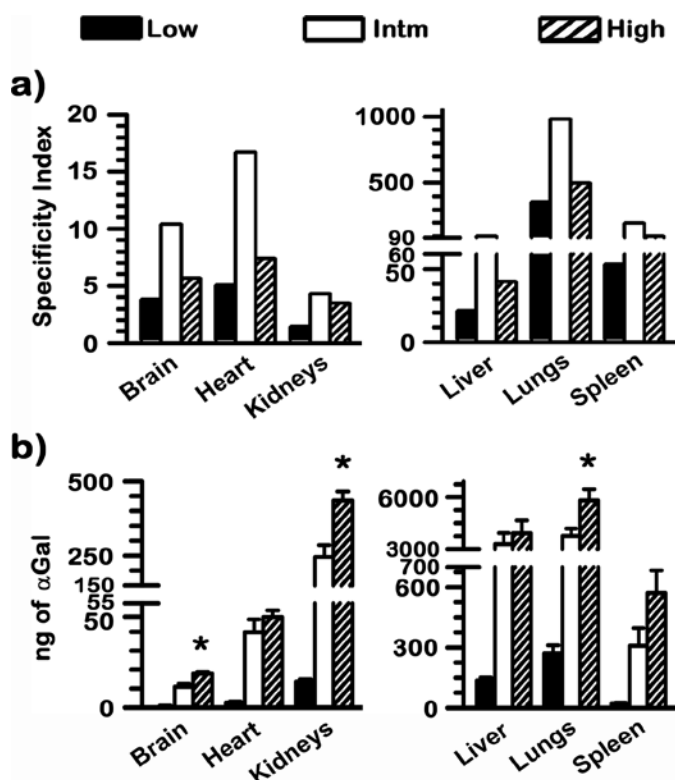


Figure 39. Enhanced specificity and absolute α Gal targeting by varying nanocarrier design parameters. Mice were injected i.v. with anti-ICAM/ 125 I- α Gal NCs displaying varying antibody-to-enzyme surface-density ratios, at varying nanocarrier bulk concentrations, rendering low (45 μ g/kg), intermediate (Intm; 449 μ g/kg), or high (555 μ g/kg) α Gal doses, or with equivalent doses of naked, non-targeted 125 I- α Gal. Blood samples and organs were collected, weighed, and measured for 125 I content 30 min after injection. (a) Specificity index, SI, was determined by comparing %ID/g per gram of organ over %ID per gram of blood (tissue-to-blood localization ratio) of anti-ICAM/ 125 I- α Gal NCs to the equivalent parameter for naked, non-targeted α Gal. This parameter describes the fold enhancement of α Gal targeted to tissue via anti-ICAM NCs. (b) Total dose (ng) of 125 I- α Gal accumulated in each organ. Data are mean \pm SEM. * $p < 0.05$, comparing intermediate versus high α Gal doses by Student's t-test. Comparing intermediate or high to low α Gal doses rendered $p < 0.001$. (Figure reproduced from [50])

increase in the enzyme delivered. Anti-ICAM/ α Gal NCs displaying ~ 500 α Gal molecules/NC (449 μ g α Gal/kg; intermediate dose) enhanced α Gal accumulation in organs (cumulatively) over 10-fold versus counterparts displaying ~ 50 α Gal molecules/NC (45 μ g α Gal/kg; low dose). Anti-ICAM/ α Gal NCs displaying ~ 500 α Gal molecules/NC and administered at 2.4×10^{13} NCs/kg (550 μ g α Gal/kg; high dose) enhanced cumulative α Gal targeting by 20%

versus administration of the same nanocarriers at 1.6×10^{13} NCs/kg (449 μg αGal /kg; intermediate dose). Total αGal delivered to the lungs 30 minutes after i.v. injection increased from ~ 270 ng to ~ 5800 ng for these three formulations. Significant enhancement was also found even for organs that are difficult to target, such as the brain, where μGal delivery increased ~ 20 -fold when comparing high to low dose (max. brain accumulation was 17.8 ng). This was also the case for the heart and kidneys, key FD organs, with maximum accumulation of ~ 48 ng and ~ 435 ng, respectively.

Notably, total amount of αGal delivered to tissues increased from 0.45 μg (low dose) to 7.7 μg (intermediate dose) to 10.8 μg (high dose), which is very significant compared to the initial administered dose of ~ 0.73 μg , ~ 11.7 μg , and ~ 15.8 μg of αGal , respectively. This represents a consistent pattern of 65% of the injected dose accumulating in the six harvested organs. Although these data was obtained 30 minutes after injection, as mentioned above, previously published results indicated that a significant amount of αGal transported by anti-ICAM NCs remain in the targeted organs 24 hours after administration (Figure 34c): e.g., 150-fold pulmonary accumulation over free αGal at this time [48, 215]. This result suggests that these variations of the nanocarrier formulation have a linear effect on the enzyme delivery, rendering a relatively controllable system for delivering such a cargo. From a translational perspective, current ERT for FD in the clinic typically consists of i.v. infusions of 1 mg/kg every two weeks, associated with high probability for development of resistance due to generation of anti- αGal blocking antibodies [95]. The lowest dose of 45 μg of αGal /kg tested in this study is ~ 20 -fold lower than current clinical doses, yet ICAM-1 targeting provides targeting enhancement compared to the naked enzyme.

4.4.6. Conclusion

As a stable pro-drug coat of targeting moiety and drug model with conditional enzyme drug release (Figure 5, Section 4.1.2.), eliciting similar binding, uptake, lysosomal trafficking, and substrate degradation by 3 lysosomal enzyme cargos targeted to ICAM-1 (Section 4.1.), and similar biodistribution pattern with varying enzyme delivery enhancement levels to tissue (Section 4.3.), we further questioned whether anti-ICAM/enzyme NCs can be modulated to optimize enzyme delivery. Indeed, both the surface density of the targeting moiety on ICAM-1-targeted NCs and NC bulk concentration injected in circulation can be varied to regulate the total amount of a surface-loaded cargo (such as the case of therapeutic lysosomal enzyme pro-drugs) that can reach target organs in the body, without negatively impacting targeting specificity and biodistribution. The presence on the nanoparticle surface of a cargo that has affinity toward cell-surface markers seems to somehow compensate for the potential decay in avidity associated with the reduced surface-density of the (antibody) targeting moiety. Hence, this strategy can be used to enhance tissue delivery of lower lysosomal enzyme doses, which, along with fast removal from the circulation, may help improve the efficacy of lysosomal ERT and, likely, similar therapeutic approaches.

Section 5. Overall conclusions

5.1. Summary

Treatment availability for LSDs in the past couple of decades has greatly improved the life expectancy and quality of life of patients. Currently, available treatments options include ERT, bone marrow transplant and substrate reduction therapy, and chaperone therapy [4, 10]. Research into gene therapy shows promise and is under clinical trial [4]. However, of available therapies, ERT is one of the most promising judging by demonstrated effects. At the moment, six LSDs are treatable by ERT, including FD and PD [4]. Yet, outcomes of ERT are still suboptimal: accumulation to clearance tissues with limited to no delivery to many diseased tissues, poor transport across the BBB, inadequate uptake due to impaired cellular internalization pathways, etc. [95-99, 101]. With concurrent advances in nanotechnology and drug delivery, improvements to ERT could be tangible, such as use of fusion proteins or targeted drug delivery vehicles [11, 41, 42, 62, 128, 129]. Yet, majority of these alternative approaches still rely on clathrin-mediated uptake, which seems to be disrupted in several LSDs [27-29]. This dissertation focuses on expanding an alternative model previously proposed by our laboratory, which rapidly delivers enzyme therapeutic to tissue, selectively bind to diseased cells, and allows for internalization and trafficking to lysosomes of cells via ICAM-1-targeting.

Previous work with ICAM-1-targeting nanocarriers delivering ASM has shown favorable results with enhanced enzyme targeting to tissue *in vivo*, as well as binding, internalization, and lysosomal trafficking where the delivered enzyme can degrade accumulated substrate in cell culture [41, 42]. While this was observed for the delivery of ASM for treatment of type A and B NPD, in this dissertation, we have (1) extended similar

observations for other lysosomal enzymes, (2) demonstrated ability of ICAM-1-targeting system to traverse across BBB models, (3) shown enhancement of enzyme accumulation in the brain in vivo, and (4) expanded means to manipulate the dose of enzyme delivered.

We first examined the stability of these formulations and determined that both anti-ICAM/ α Gal NCs and anti-ICAM/GAA NCs were indeed stable with minimal enzyme release from nanocarriers in storage and physiologically neutral pH conditions, but conditional release of enzyme was observed when anti-ICAM/enzyme NCs were exposed to lysosomal acidic conditions or lysosomal storage conditions (Section 4.1.2.). Since the two anti-ICAM/enzyme NCs showed similar formulation stability and enzyme release characteristics, we then focused on expanding this application to two other LSDs, specifically delivering α Gal and GAA to FD- or PD-models, respectively. As discussed in section 4.1., more enzyme was targeted diseased cells compared to healthy cells, and efficiently internalized and trafficked to lysosomes via CAM-mediated endocytosis, independent of classical pathways known to be impaired in most LSDs. Moreover, delivered enzymes into lysosomes effectively degrade excessively accumulated lysosomal substrate. Even though different patterns of efficiencies did arise amongst historical and tested anti-ICAM/enzyme NCs, such as specific binding, percent uptake, endocytic pathways involved, percent trafficked to lysosomes, alleviation of accumulated lysosomal substrate, etc., the collected results were positive to suggest that ICAM-1-targeting systems can be used to enhance lysosomal enzymes to treat LSDs in general. Yet, as indicated, each application must be thoroughly assessed.

To address neurological effects that manifests in several LSDs, application of anti-ICAM NCs to target cells of the BBB, which regulates transport between the circulation and the brain parenchyma, and cells of the brain were specifically examined in Section 4.2. Cells of the BBB, mainly brain ECs, ACs, and PCs, exhibited differential ICAM-1-expression,

especially notable between diseased versus healthy cells for all three cell types, with diseased ECs expressing the most total and most dense ICAM-1 amongst the three cell types. Yet anti-ICAM NCs target, internalize, and trafficked to lysosomes via mainly CAM-mediation pathway in all three cell types, although more anti-ICAM NCs tended to bind, internalize, and traffic to lysosomes in ECs than compared to subendothelial cells. Additionally, transport of anti-ICAM NCs across EC monolayer was selective to diseased cells and ICAM-1-targeting, occurring also mainly via CAM-mediation. In fact, transcytosis across ECs resulted in significant accumulation to the subendothelial layer in a bi-layer co-cultured BBB model. However, despite the noted lysosomal trafficking observed in cultures of individual cells, in a bi-layer co-cultured BBB model, a portion of bound anti-ICAM NCs continued to transport across the subendothelial layer as well, achieving transport across bi-layered BBB models. With anti-ICAM NCs confirmed to be able to traverse the BBB, we then examined the capability of targeting neurons. Indeed, anti-ICAM NCs can bind, internalize, and traffic to lysosomes of NLCs mainly via CAM-mediation, interestingly, in both cell body and cell processes regions.

In Section 4.3., we discussed that the biodistribution of ICAM-1-targeted enzyme *in vivo* showed enhanced delivery over non-targeted enzyme to all major organs investigated (heart, kidneys, liver, lungs, spleen), which represents targets for intervention in these diseases, e.g. heart and kidneys for FD, and the heart and skeletal muscles for PD, apart from RES organs also involved. Additionally, for the first time, we examined brain targeting *in vivo*. In accord with other organs, anti-ICAM NCs enhanced enzyme delivery to the brain over non-targeted enzyme, preferentially accumulating in the cerebellum, a site responsible for motor control and balance, and known to be affected in NPD and several other LSDs.

The above work emphasized the implementation of ICAM-1-targeting drug delivery systems to enhance enzyme delivery to treat several LSDs. We note that our proof-of-concept

model is in fact a pro-drug model with both the targeting moiety (anti-ICAM) and cargo (enzyme) coated onto the surface a polystyrene latex nanoparticle. Since this pro-drug model is deemed stable, in Section 4.4. we discussed efforts to optimize the formulation to increase bulk enzyme delivery to the six major organs studied. Total enzyme delivery to an individual organ could be enhanced by 12 to 29-folds by increasing the surface density of the enzyme on the NC by 10 folds, displacing 50% of the targeting moiety, and by increasing the bulk-nanoparticle concentration administered by 1.5-folds, without adversely affecting targeting specificity and biodistribution pattern.

All in all, targeting ICAM-1 does enhance enzyme delivery to tissue, and targets diseased cells, triggering uptake and lysosomal trafficking mainly via CAM-mediated pathway in both endothelial and non-endothelial cells, and lastly, delivered enzyme can alleviate lysosomal storage. Hence, through results from this dissertation, ICAM-1-targeting strategy can potentially be applied to improve ERT for LSDs.

5.2. Future directions

Through this dissertation, advances toward improving ERT for LSDs using ICAM-1-targeting drug delivery system were achieved. However, the work presented here is a proof-of-concept model and significantly more work still needs to be done to answer relevant questions and to expand this project. Firstly, future studies could focus on translatability of this work. One example would be to use PLGA particles as oppose to the model polystyrene latex particles. We note that the anti-ICAM/enzyme NC formulations tested in this thesis are of a “pro-drug” prototype with both the anti-ICAM targeting moiety and lysosomal enzyme cargo coated onto the surface of latex nanocarriers, previously confirmed to have similar binding, internalization, intracellular trafficking characteristics as PLGA nanoparticles [41], a

biodegradable material that is already in several FDA-approved devices [108]. Future work will include confirming brain delivery achieved by anti-ICAM NCs presented in this thesis with PLGA particles. Additionally, we are currently working towards encapsulating the enzyme cargo into PLGA particles for added protection and controlled release upon degradation in the lysosome. Another way to expand this work into a translatable project is to improve the pro-drug formulation, specifically altering the targeting moiety without negatively impairing its binding efficiency. The work described utilizes whole antibodies from another species as the targeting moiety molecule, which can potentially lead to adverse immune recognition. Truncating the targeting antibody to only include the targeting aspect of the antibody, e.g. binding sequence of the antibody variable region, may minimize potential toxicity and immune recognition of antibody Fc regions humanized antibody. To address this, current work involving a 17-mer linear peptide ($\gamma 3$) has been published [125]; future works will incorporate enzyme delivery, similar to previous studies.

In addition to potential future work involving formulation optimization, we also suggest further cell culture work, particularly in studying transport across cell barriers, such as the case of the BBB. In this dissertation we show that anti-ICAM NCs can cross BBB models. The next step may be to incorporate enzyme cargo and see if transport across cell barriers may affect the integrity of the anti-ICAM/enzyme NC and enzyme activity. We also note from our work that anti-ICAM NCs transported across the BBB are actually transcytosed through cells of the endothelial BBB layer. It is possible that some NCs are transported paracellularly, especially between cells of the subendothelial BBB layer that are not as tightly bound. Since the method of transport through the extracellular matrix has not been elucidated (although is currently being studied), perhaps studies involving transport pathway can give insight into how anti-ICAM NCs can be better formulated to traffic to the brain parenchyma with minimal damage to the tissue, minimal leakage, if any, across tissue, and minimal effect

to the cargo the NC bears. Tissue damage can be elucidated by examining the BBB model integrity, specifically endothelial and subendothelial layer morphology, through histology or TEM. Leakage across the BBB model can be studied with radioisotope tracing of molecules, such as BSA, co-incubated along-side anti-ICAM NCs with cells. Presence of the molecule in the basolateral chamber with transported nanocarriers can then be assessed. Additionally, future studies could evaluate the post-transport binding capacity of anti-ICAM NCs by incubating anti-ICAM NCs with BBB transwell model that also include neurons cultured in the basolateral chamber. As a result, using radio-isotope labeled NCs and/or immunohistochemistry, a detailed study differentiating percentage of targeting can be analyzed, which could help with optimizing the design of the anti-ICAM/enzyme NC formulation. This work can be paired with in vivo studies with detailed histological stains of tissue and/or TEM to visualize delivered anti-ICAM NCs, which has begun to be addressed. Lastly, anti-ICAM NC binding and internalization into diseased NLCs varied between cell body and processes regions. Therefore, to better understand targeting, endocytosis, and lysosomal trafficking to study CNS treatment potential, LSD-model neurons could also be studied to confirm delivery and substrate attenuation by anti-ICAM/enzyme NCs. Immunohistochemistry similar to the described work with HUVEC models can be implemented.

Additionally, in vivo work pertaining to this project could be extended. Since current ERT for LSD is a life-long treatment requiring bi-weekly doses, long term studies testing the efficacy of anti-ICAM/enzyme NCs to mice models bearing LSDs should be performed. We suggest future work to include focusing on improving ERT that are currently available, working with an existing LSD model mice, e.g. α Gal A-deficient mice for FD [219] can be treated with anti-ICAM NCs bearing the recombinant enzyme currently used for ERT. Long-term studies in the NPD model could examine animal behavior for phenotypic response (e.g. examination of ataxia prevention or motor-skill deterioration through comparative rotarod

testings) and longevity, as well as compare cell morphological changes as a response to treatment by examining brain tissue morphology using histology and/or transmission electron microscopy (TEM). Since current ERT do not relieve symptoms and can trigger immune response, resulting in suboptimal treatment, by observing anti-ICAM/enzyme NC long-term effects on mice behavior and tissue, immune response and symptoms in intractable tissue can be monitored (through periodic blood samples and histology examination after euthanization) and compared to current ERT to evaluate whether this method can in fact improve delivery while minimizing immune response. Moreover, we note that targeting ICAM-1 to deliver enzyme was systemic, which is beneficial for LSDs since all tissue are affected. More comprehensive studies examining the depth of attenuation of lysosomal storage in tissue would be useful. This could be performed by examining tissue samples from mice studies (long-term or short-term) with histology and TEM to examine morphological changes and levels of lysosomal substrate present.

In addition to *in vivo* work focused on treatment efficiency of enhanced enzyme delivery in LSD-model mice, *in vivo* work studying optimization of formulation could also be extended to adjust anti-ICAM/enzyme NC treatment efficacy. In Section 4.4. we discussed the potential of optimizing anti-ICAM/enzyme NC formulations by modulating the formulation itself to increase enzyme delivery. Interestingly, decreasing the targeting moiety density by half did not diminish specificity and distribution. Further studies with a smaller targeting moiety (such as $\gamma 3$) may prove to also conserve targeting specificity and biodistribution pattern. Additional bulk-concentration studies (e.g. increasing administered dose to 4-folds) can also be performed to delineate the potential saturation point of binding or tissue delivery. Another method that was not examined here but was previously studied is administering multiple doses [157]. This can be performed by injecting mice with multiple doses sequentially, e.g. injection of a 2nd dose 15 or 30 minutes after the first dose. Since anti-

ICAM NCs leave the circulation within ~1 minute of injection to rapidly target tissue, this first dose can be used to saturate certain binding sites, i.e. the highly targeted lungs and liver, such that subsequent dose(s) can reach to more intractable tissue, potentially resulting in a broader tissue biodistribution. This experiment could be performed using non-radioisotope labeled anti-ICAM/enzyme NCs for the first dose, while using radioisotope labeled anti-ICAM/enzyme NCs for 2nd dose to trace and delineate broadened tissue targeting.

All in all, this dissertation has shown the potential of using ICAM-1-targeted drug delivery to enhance enzyme delivery for possibly several LSD treatments, a method that can be optimized to potentially be expanded to other treatments as well. As mentioned, a likely synergistic and/or additive effect of having both the anti-ICAM and enzyme on the NC has shown to provide unique patterns of distribution. Hence, it is likely that other unique combinations could elicit unforeseeable delivery outcomes. In addition to capitalizing the unique combinations, there are several other methods that can be exploited to control the distribution pattern, the rate of delivery, and/or bulk of cargo delivery. By targeting a combination of receptors (within the same family or not) or epitopes (on the same receptor or not) [160], or modulating the size and shape of the NC [158], or route of administration [152], can yield a variety of targeting patterns, and therefore can be exploited depending on the purpose of the delivery. Therefore, much still needs to be answered to complete the project, but much more can be studied to find the unique combination to greatly enhance specific ERT for LSD or for any therapy.

References

1. Applegarth, DA, Toone, JR, and Lowry, RB (2000). Incidence of inborn errors of metabolism in British Columbia, 1969-1996. *Pediatrics* **105**: e10.
2. Deodato, F, *et al.* (2004). Inborn errors of metabolism: an update on epidemiology and on neonatal-onset hyperammonemia. *Acta Paediatr Suppl* **93**: 18-21.
3. Fuller, M, Meikle, PJ, and Hopwood, JJ (2006). Epidemiology of lysosomal storage diseases: an overview. In: Mehta, A, M Beck and G Sunder-Plassmann eds). *Fabry Disease: Perspectives from 5 Years of FOS*. Oxford PharmaGenesis: Oxford
4. Ohashi, T (2012). Enzyme replacement therapy for lysosomal storage diseases. *Pediatr Endocrinol Rev* **10 Suppl 1**: 26-34.
5. Pinto, R, *et al.* (2004). Prevalence of lysosomal storage diseases in Portugal. *Eur J Hum Genet* **12**: 87-92.
6. Poorthuis, BJ, *et al.* (1999). The frequency of lysosomal storage diseases in The Netherlands. *Hum Genet* **105**: 151-156.
7. Poupetova, H, Ledvinova, J, Berna, L, Dvorakova, L, Kozich, V, and Elleder, M (2010). The birth prevalence of lysosomal storage disorders in the Czech Republic: comparison with data in different populations. *J Inherit Metab Dis* **33**: 387-396.
8. Urbanelli, L, Sagini, K, Polidoro, M, Brozzi, A, Magini, A, and Emiliani, C (2013). Therapeutic approaches for lysosomal storage diseases: a patent update. *Recent Pat CNS Drug Discov* **8**: 91-109.
9. Mechtler, TP, *et al.* (2012). Neonatal screening for lysosomal storage disorders: feasibility and incidence from a nationwide study in Austria. *Lancet* **379**: 335-341.
10. Desnick, RJ, and Schuchman, EH (2012). Enzyme replacement therapy for lysosomal diseases: lessons from 20 years of experience and remaining challenges. *Annu Rev Genomics Hum Genet* **13**: 307-335.
11. LeBowitz, JH, Grubb, JH, Maga, JA, Schmiel, DH, Vogler, C, and Sly, WS (2004). Glycosylation-independent targeting enhances enzyme delivery to lysosomes and decreases storage in mucopolysaccharidosis type VII mice. *Proc Natl Acad Sci U S A* **101**: 3083-3088.
12. Prince, WS, *et al.* (2004). Lipoprotein receptor binding, cellular uptake, and lysosomal delivery of fusions between the receptor-associated protein (RAP) and alpha-L-iduronidase or acid alpha-glucosidase. *J Biol Chem* **279**: 35037-35046.
13. Rohrbach, M, and Clarke, JT (2007). Treatment of lysosomal storage disorders : progress with enzyme replacement therapy. *Drugs* **67**: 2697-2716.
14. Moore, DF, Ries, M, Forget, EL, and Schiffmann, R (2007). Enzyme replacement therapy in orphan and ultra-orphan diseases: the limitations of standard economic metrics as exemplified by Fabry-Anderson disease. *Pharmacoeconomics* **25**: 201-208.
15. Rombach, SM, Hollak, CE, Linthorst, GE, and Dijkgraaf, MG (2013). Cost-effectiveness of enzyme replacement therapy for Fabry disease. *Orphanet J Rare Dis* **8**: 29.

16. Muro, S (2012). Strategies for delivery of therapeutics into the central nervous system for treatment of lysosomal storage disorders. *Drug Delivery and Translational Research* **2**: 169-186.
17. Tracey, KJ, and Metz, CN (2007). Brain endothelial cells bridge neural and immune networks. In: Aird, WC (ed). *Endothelial Biomedicine*. Cambridge University Press. pp 1140-1153.
18. Weidenfeller, C, and Shusta, EV (2007). Blood-brain barrier. In: Aird, WC (ed). *Endothelial Biomedicine*. Cambridge University Press. pp 1124-1139.
19. Abbott, NJ (2013). Blood-brain barrier structure and function and the challenges for CNS drug delivery. *J Inherit Metab Dis* **36**: 437-449.
20. Jin, HK, Carter, JE, Huntley, GW, and Schuchman, EH (2002). Intracerebral transplantation of mesenchymal stem cells into acid sphingomyelinase-deficient mice delays the onset of neurological abnormalities and extends their life span. *J Clin Invest* **109**: 1183-1191.
21. Bonney, DK, *et al.* (2010). Successful allogeneic bone marrow transplant for Niemann-Pick disease type C2 is likely to be associated with a severe 'graft versus substrate' effect. *J Inherit Metab Dis*.
22. Schuchman, EH (2007). The pathogenesis and treatment of acid sphingomyelinase-deficient Niemann-Pick disease. *J Inherit Metab Dis* **30**: 654-663.
23. Allen, TM, and Cullis, PR (2004). Drug delivery systems: entering the mainstream. *Science* **303**: 1818-1822.
24. Muro, S (2012). Challenges in design and characterization of ligand-targeted drug delivery systems. *J Control Release* **164**: 125-137.
25. Singh, R, and Lillard, JW, Jr. (2009). Nanoparticle-based targeted drug delivery. *Exp Mol Pathol* **86**: 215-223.
26. Hilgenbrink, AR, and Low, PS (2005). Folate receptor-mediated drug targeting: from therapeutics to diagnostics. *J Pharm Sci* **94**: 2135-2146.
27. Cardone, M, *et al.* (2008). Abnormal mannose-6-phosphate receptor trafficking impairs recombinant alpha-glucosidase uptake in Pompe disease fibroblasts. *Pathogenetics* **1**: 6.
28. Dhimi, R, and Schuchman, EH (2004). Mannose 6-phosphate receptor-mediated uptake is defective in acid sphingomyelinase-deficient macrophages: implications for Niemann-Pick disease enzyme replacement therapy. *J Biol Chem* **279**: 1526-1532.
29. Fukuda, T, *et al.* (2006). Dysfunction of endocytic and autophagic pathways in a lysosomal storage disease. *Ann Neurol* **59**: 700-708.
30. Lee, KO, Luu, N, Kaneshi, CR, Schiffmann, R, Brady, RO, and Murray, GJ (2005). Improved intracellular delivery of glucocerebrosidase mediated by the HIV-1 TAT protein transduction domain. *Biochem Biophys Res Commun* **337**: 701-707.
31. Orii, KO, *et al.* (2005). Defining the pathway for Tat-mediated delivery of beta-glucuronidase in cultured cells and MPS VII mice. *Mol Ther* **12**: 345-352.
32. Dekiwadia, CD, Lawrie, AC, and Fecondo, JV (2012). Peptide-mediated cell penetration and targeted delivery of gold nanoparticles into lysosomes. *J Pept Sci* **18**: 527-534.

33. Zhang, XY, Dinh, A, Cronin, J, Li, SC, and Reiser, J (2008). Cellular uptake and lysosomal delivery of galactocerebrosidase tagged with the HIV Tat protein transduction domain. *J Neurochem* **104**: 1055-1064.
34. Murray, GJ, Anver, MR, Kennedy, MA, Quirk, JM, and Schiffmann, R (2007). Cellular and tissue distribution of intravenously administered agalsidase alfa. *Mol Genet Metab* **90**: 307-312.
35. Beck, M (2009). Agalsidase alfa for the treatment of Fabry disease: new data on clinical efficacy and safety. *Expert Opin Biol Ther* **9**: 255-261.
36. Ley, K, and Kansas, GS (2004). Selectins in T-cell recruitment to non-lymphoid tissues and sites of inflammation. *Nat Rev Immunol* **4**: 325-335.
37. Millán, J, Hewlett, L, Glyn, M, Toomre, D, Clark, P, and Ridley, AJ (2006). Lymphocyte transcellular migration occurs through recruitment of endothelial ICAM-1 to caveola- and F-actin-rich domains. *Nat Cell Biol* **8**: 113-123.
38. Rothlein, R, Dustin, ML, Marlin, SD, and Springer, TA (1986). A human intercellular adhesion molecule (ICAM-1) distinct from LFA-1. *J Immunol* **137**: 1270-1274.
39. Muro, S (2007). Intercellular Adhesion Molecule-1 and Vascular Cell Adhesion Molecule-1. In: Aird, WC (ed). *Endothelial biomedicine*, 1 ed. Cambridge University Press: New York. pp 1058-1070.
40. Muro, S, *et al.* (2003). A novel endocytic pathway induced by clustering endothelial ICAM-1 or PECAM-1. *J Cell Sci* **116**: 1599-1609.
41. Garnacho, C, *et al.* (2008). Delivery of acid sphingomyelinase in normal and niemann-pick disease mice using intercellular adhesion molecule-1-targeted polymer nanocarriers. *J Pharmacol Exp Ther* **325**: 400-408.
42. Muro, S, Schuchman, EH, and Muzykantov, VR (2006). Lysosomal enzyme delivery by ICAM-1-targeted nanocarriers bypassing glycosylation- and clathrin-dependent endocytosis. *Mol Ther* **13**: 135-141.
43. Ghaffarian, R, Bhowmick, T, and Muro, S (2012). Transport of nanocarriers across gastrointestinal epithelial cells by a new transcellular route induced by targeting ICAM-1. *J Control Release* **163**: 25-33.
44. Calderon, AJ, *et al.* (2011). Optimizing endothelial targeting by modulating the antibody density and particle concentration of anti-ICAM coated carriers. *J Control Release* **150**: 37-44.
45. Desnick, RJ, Ioannou, Y.A., Eng, C.M. (2001). α -Galactosidase A Deficiency: Fabry Disease. In: Scriver, C, *et al.* eds). *The Metabolic and Molecular Bases of Inherited Disease*, 8th ed., vol. 3. McGraw-Hill. p 3733.
46. Hirschhorn, R, and Reuser, AJJ (2001). Glycogen storage Disease Type II: Acid α -Glucosidase (Acid Maltase) Deficiency. In: Scriver, C, *et al.* eds). *The Metabolic and Molecular Bases of Inherited Disease*, 8th ed., vol. 3. McGraw-Hill. p 3389.
47. Hsu, J, Northrup, L, Bhowmick, T, and Muro, S (2012). Enhanced delivery of alpha-glucosidase for Pompe disease by ICAM-1-targeted nanocarriers: comparative performance of a strategy for three distinct lysosomal storage disorders. *Nanomedicine* **8**: 731-739.

48. Hsu, J, *et al.* (2011). Enhanced endothelial delivery and biochemical effects of alpha-galactosidase by ICAM-1-targeted nanocarriers for Fabry disease. *J Control Release* **149**: 323-331.
49. Hsu, J, Rappaport, J, and Muro, S (2014). Specific binding, uptake, and transport of ICAM-1-targeted nanocarriers across endothelial and subendothelial cell components of the blood-brain barrier. *Pharm Res.*
50. Hsu, J, Bhowmick, T, Burks, SR, Kao, JPY, and Muro, S (2014). Enhancing biodistribution of therapeutic enzymes in vivo by modulating surface coating and concentration of ICAM-1-targeted nanocarriers. *J Biomed Nanotechnol* **10**: 345-354.
51. Reaves, BJ, Row, PE, Bright, NA, Luzio, JP, and Davidson, HW (2000). Loss of cation-independent mannose 6-phosphate receptor expression promotes the accumulation of lysobisphosphatidic acid in multilamellar bodies. *J Cell Sci* **113 (Pt 22)**: 4099-4108.
52. van Gelder, CM, Vollebregt, AA, Plug, I, van der Ploeg, AT, and Reuser, AJ (2012). Treatment options for lysosomal storage disorders: developing insights. *Expert Opin Pharmacother* **13**: 2281-2299.
53. Luzio, JP, Pryor, PR, and Bright, NA (2007). Lysosomes: fusion and function. *Nat Rev Mol Cell Biol* **8**: 622-632.
54. Manthe, RL, and Muro, S (2014). Lysosomes and Nanotherapeutics: Diseases, Treatments, and Side Effects. In: Torchilin, V (ed). *Handbook of Nanobiomedical Research: Fundamentals, Applications, and Recent Developments*, vol. 2 (Applications in Therapy). World Scientific Publishing.
55. Futerman, AH, and van Meer, G (2004). The cell biology of lysosomal storage disorders. *Nat Rev Mol Cell Biol* **5**: 554-565.
56. Holtzman, E (1989). Historical fragments; methods; some terminology. In: Siekevitz, P (ed). *Lysosomes*, vol. XVI. Plenum Press: New York. pp 1-24.
57. Sabatini, DD, and Adesnick, MB (2001). The biogenesis of membranes and organelles. In: Scriver, C, *et al.* eds). *The metabolic and molecular bases of inherited disease*. McGraw-Hill: New York. pp 433-520.
58. Andrews, NW (2000). Regulated secretion of conventional lysosomes. *Trends Cell Biol* **10**: 316-321.
59. McNeil, PL, and Kirchhausen, T (2005). An emergency response team for membrane repair. *Nat Rev Mol Cell Biol* **6**: 499-505.
60. Mellman, I, Fuchs, R, and Helenius, A (1986). Acidification of the endocytic and exocytic pathways. *Annu Rev Biochem* **55**: 663-700.
61. Cooper, GM, and Hausman, RE (2013). Protein sorting and transport. *The cell: a molecular approach*, 6 ed. Sinauer Associates: Sunderland, MA. pp 373-419.
62. Muro, S (2010). New biotechnological and nanomedicine strategies for treatment of lysosomal storage disorders. *Wiley Interdiscip Rev Nanomed Nanobiotechnol* **2**: 189-204.
63. Schuchman, EH, and Desnick, RJ (2001). Niemann-Pick Disease Types A and B: Acid Sphingomyelinase Deficiencies. In: Scriver, C, *et al.* eds). *The Metabolic and Molecular Bases of Inherited Disease*, 8th ed., vol. 3. McGraw-Hill: New York. pp 3589-3610.

64. Bekri, S, Lidove, O, Jaussaud, R, Knebelmann, B, and Barbey, F (2006). The role of ceramide trihexoside (globotriaosylceramide) in the diagnosis and follow-up of the efficacy of treatment of Fabry disease: a review of the literature. *Cardiovasc Hematol Agents Med Chem* **4**: 289-297.
65. Parenti, G, Pignata, C, Vajro, P, and Salerno, M (2013). New strategies for the treatment of lysosomal storage diseases (review). *Int J Mol Med* **31**: 11-20.
66. Butters, TD (2007). Pharmacotherapeutic strategies using small molecules for the treatment of glycolipid lysosomal storage disorders. *Expert Opin Pharmacother* **8**: 427-435.
67. Boyd, RE, *et al.* (2013). Pharmacological chaperones as therapeutics for lysosomal storage diseases. *J Med Chem* **56**: 2705-2725.
68. Aymami, J, Barril, X, Rodriguez-Pascau, L, and Martinell, M (2013). Pharmacological chaperones for enzyme enhancement therapy in genetic diseases. *Pharm Pat Anal* **2**: 109-124.
69. Bruni, S, Loschi, L, Incerti, C, Gabrielli, O, and Coppa, GV (2007). Update on treatment of lysosomal storage diseases. *Acta Myol* **26**: 87-92.
70. Ruiz de Garibay, AP, Solinis, MA, and Rodriguez-Gascon, A (2013). Gene therapy for fabry disease: a review of the literature. *BioDrugs* **27**: 237-246.
71. Schneiderman, J, Thormann, K, Charrow, J, and Kletzel, M (2007). Correction of enzyme levels with allogeneic hematopoietic progenitor cell transplantation in Niemann-Pick type B. *Pediatr Blood Cancer* **49**: 987-989.
72. Krivit, W, Peters, C, and Shapiro, EG (1999). Bone marrow transplantation as effective treatment of central nervous system disease in globoid cell leukodystrophy, metachromatic leukodystrophy, adrenoleukodystrophy, mannosidosis, fucosidosis, aspartylglucosaminuria, Hurler, Maroteaux-Lamy, and Sly syndromes, and Gaucher disease type III. *Curr Opin Neurol* **12**: 167-176.
73. Peters, C, and Steward, CG (2003). Hematopoietic cell transplantation for inherited metabolic diseases: an overview of outcomes and practice guidelines. *Bone Marrow Transplant* **31**: 229-239.
74. Bae, JS, *et al.* (2007). Bone marrow-derived mesenchymal stem cells promote neuronal networks with functional synaptic transmission after transplantation into mice with neurodegeneration. *Stem Cells* **25**: 1307-1316.
75. Asheuer, M, *et al.* (2004). Human CD34+ cells differentiate into microglia and express recombinant therapeutic protein. *Proc Natl Acad Sci U S A* **101**: 3557-3562.
76. Patil, SA, and Maegawa, GH (2013). Developing therapeutic approaches for metachromatic leukodystrophy. *Drug Des Devel Ther* **7**: 729-745.
77. Baudhuin, P, Hers, HG, and Loeb, H (1964). An Electron Microscopic and Biochemical Study of Type Ii Glycogenosis. *Lab Invest* **13**: 1139-1152.
78. Hug, G, and Schubert, WK (1967). Lysosomes in type II glycogenosis. Changes during administration of extract from *Aspergillus niger*. *J Cell Biol* **35**: C1-6.
79. Kornfeld, S, Reitman, ML, Varki, A, Goldberg, D, and Gabel, CA (1982). Steps in the phosphorylation of the high mannose oligosaccharides of lysosomal enzymes. *Ciba Found Symp*: 138-156.

80. Le Borgne, R, and Hoflack, B (1998). Protein transport from the secretory to the endocytic pathway in mammalian cells. *Biochim Biophys Acta* **1404**: 195-209.
81. Braulke, T, and Bonifacino, JS (2009). Sorting of lysosomal proteins. *Biochim Biophys Acta* **1793**: 605-614.
82. Lee, K, *et al.* (2003). A biochemical and pharmacological comparison of enzyme replacement therapies for the glycolipid storage disorder Fabry disease. *Glycobiology* **13**: 305-313.
83. Sly, WS (2002). Enzyme replacement therapy: from concept to clinical practice. *Acta Paediatr Suppl* **91**: 71-78.
84. Desnick, RJ (2004). Enzyme replacement therapy for Fabry disease: lessons from two alpha-galactosidase A orphan products and one FDA approval. *Expert Opin Biol Ther* **4**: 1167-1176.
85. Mehta, A, *et al.* (2008). Enzyme replacement therapy in Fabry disease: comparison of agalsidase alfa and agalsidase beta. *Mol Genet Metab* **95**: 114-115.
86. Koeberl, DD, *et al.* (2011). Enhanced efficacy of enzyme replacement therapy in Pompe disease through mannose-6-phosphate receptor expression in skeletal muscle. *Mol Genet Metab* **103**: 107-112.
87. Weidemann, F, Linhart, A, Monserrat, L, and Strotmann, J (2010). Cardiac challenges in patients with Fabry disease. *Int J Cardiol* **141**: 3-10.
88. Weidemann, F, *et al.* (2009). Long-term effects of enzyme replacement therapy on Fabry cardiomyopathy: evidence for a better outcome with early treatment. *Circulation* **119**: 524-529.
89. Warnock, DG, *et al.* (2012). Renal outcomes of agalsidase beta treatment for Fabry disease: role of proteinuria and timing of treatment initiation. *Nephrol Dial Transplant* **27**: 1042-1049.
90. von Figura, K (1991). Molecular recognition and targeting of lysosomal proteins. *Curr Opin Cell Biol* **3**: 642-646.
91. Jofre, GF, Balmaceda, V, Sartor, T, Carvelli, L, Barrera, P, and Sosa, MA (2009). Organ-specific changes in the expression of mannose-6-phosphate receptors during postnatal development in rats. *Cells Tissues Organs* **190**: 27-33.
92. Romano, PS, Lopez, AC, Mariani, ML, Sartor, T, Belmonte, SA, and Sosa, MA (2002). Expression and binding properties of the two mannose-6-phosphate receptors differ during perinatal development in rat liver. *Biochem Biophys Res Commun* **295**: 1000-1006.
93. Koskenvuo, JW, *et al.* (2008). Twenty-four-month alpha-galactosidase A replacement therapy in Fabry disease has only minimal effects on symptoms and cardiovascular parameters. *J Inherit Metab Dis* **31**: 432-441.
94. Schiffmann, R, and Ries, M (2005). Fabry's disease--an important risk factor for stroke. *Lancet* **366**: 1754-1756.
95. Wilcox, WR, *et al.* (2012). Anti-alpha-galactosidase A antibody response to agalsidase beta treatment: data from the Fabry Registry. *Mol Genet Metab* **105**: 443-449.

96. Kishnani, PS, *et al.* (2010). Cross-reactive immunologic material status affects treatment outcomes in Pompe disease infants. *Mol Genet Metab* **99**: 26-33.
97. Sun, B, *et al.* (2010). Antibody formation and mannose-6-phosphate receptor expression impact the efficacy of muscle-specific transgene expression in murine Pompe disease. *J Gene Med* **12**: 881-891.
98. Linthorst, GE, Hollak, CE, Donker-Koopman, WE, Strijland, A, and Aerts, JM (2004). Enzyme therapy for Fabry disease: neutralizing antibodies toward agalsidase alpha and beta. *Kidney Int* **66**: 1589-1595.
99. Ohashi, T, Iizuka, S, Ida, H, and Eto, Y (2008). Reduced alpha-Gal A enzyme activity in Fabry fibroblast cells and Fabry mice tissues induced by serum from antibody positive patients with Fabry disease. *Mol Genet Metab* **94**: 313-318.
100. Bennett, LL, and Mohan, D (2013). Gaucher disease and its treatment options. *Ann Pharmacother* **47**: 1182-1193.
101. de Vries, JM, *et al.* (2010). High antibody titer in an adult with Pompe disease affects treatment with alglucosidase alfa. *Mol Genet Metab* **101**: 338-345.
102. Hsu, J, Muro, S. (2011). Nanomedicine and drug delivery strategies for treatment of genetic diseases. In: Plaseska-Karanfilska, D (ed). *Human genetic diseases*. InTech.: Rijeka, Croatia. pp 241-266.
103. Pacurari, M, *et al.* (2012). Cell permeability, migration, and reactive oxygen species induced by multiwalled carbon nanotubes in human microvascular endothelial cells. *J Toxicol Environ Health A* **75**: 112-128.
104. Torchilin, VP (2005). Recent advances with liposomes as pharmaceutical carriers. *Nat Rev Drug Discov* **4**: 145-160.
105. Musacchio, T, and Torchilin, VP (2011). Recent developments in lipid-based pharmaceutical nanocarriers. *Front Biosci* **16**: 1388-1412.
106. Elzoghby, AO, Samy, WM, and Elgindy, NA (2012). Protein-based nanocarriers as promising drug and gene delivery systems. *J Control Release* **161**: 38-49.
107. Seow, Y, and Wood, MJ (2009). Biological gene delivery vehicles: beyond viral vectors. *Mol Ther* **17**: 767-777.
108. Mundargi, RC, Babu, VR, Rangaswamy, V, Patel, P, and Aminabhavi, TM (2008). Nano/micro technologies for delivering macromolecular therapeutics using poly(D,L-lactide-co-glycolide) and its derivatives. *J Control Release* **125**: 193-209.
109. Panyam, J, and Labhasetwar, V (2003). Biodegradable nanoparticles for drug and gene delivery to cells and tissue. *Adv Drug Deliv Rev* **55**: 329-347.
110. Lu, JM, *et al.* (2009). Current advances in research and clinical applications of PLGA-based nanotechnology. *Expert Rev Mol Diagn* **9**: 325-341.
111. Danhier, F, Ansorena, E, Silva, JM, Coco, R, Le Breton, A, and Preat, V (2012). PLGA-based nanoparticles: an overview of biomedical applications. *J Control Release* **161**: 505-522.
112. Moghimi, SM, Hunter, AC, and Murray, JC (2001). Long-circulating and target-specific nanoparticles: theory to practice. *Pharmacol Rev* **53**: 283-318.

113. Moghimi, SM, and Szebeni, J (2003). Stealth liposomes and long circulating nanoparticles: critical issues in pharmacokinetics, opsonization and protein-binding properties. *Prog Lipid Res* **42**: 463-478.
114. Dziubla, TD, Karim, A, and Muzykantov, VR (2005). Polymer nanocarriers protecting active enzyme cargo against proteolysis. *J Control Release* **102**: 427-439.
115. Finkelstein, M, and Weissmann, G (1978). The introduction of enzymes into cells by means of liposomes. *J Lipid Res* **19**: 289-303.
116. Steger, LD, and Desnick, RJ (1977). Enzyme therapy. VI: Comparative in vivo fates and effects on lysosomal integrity of enzyme entrapped in negatively and positively charged liposomes. *Biochim Biophys Acta* **464**: 530-546.
117. Mumtaz, S, and Bachhawat, BK (1994). Enhanced intracellular stability and efficacy of PEG modified dextranase in the treatment of a model storage disorder. *Biochim Biophys Acta* **1199**: 175-182.
118. Amoozgar, Z, and Yeo, Y. Recent advances in stealth coating of nanoparticle drug delivery systems. *Wiley Interdiscip Rev Nanomed Nanobiotechnol* **4**: 219-233.
119. Alexis, F, Pridgen, E, Molnar, LK, and Farokhzad, OC (2008). Factors affecting the clearance and biodistribution of polymeric nanoparticles. *Mol Pharm* **5**: 505-515.
120. Barrias, CC, Lamghari, M, Granja, PL, Sa Miranda, MC, and Barbosa, MA (2005). Biological evaluation of calcium alginate microspheres as a vehicle for the localized delivery of a therapeutic enzyme. *J Biomed Mater Res A* **74**: 545-552.
121. Ruiz de Garibay, AP, Delgado, D, Del Pozo-Rodriguez, A, Solinis, MA, and Gascon, AR (2012). Multicomponent nanoparticles as nonviral vectors for the treatment of Fabry disease by gene therapy. *Drug Des Devel Ther* **6**: 303-310.
122. Zhang, XS, Brondyk, W, Lydon, JT, Thurberg, BL, and Piepenhagen, PA (2011). Biotherapeutic target or sink: analysis of the macrophage mannose receptor tissue distribution in murine models of lysosomal storage diseases. *J Inherit Metab Dis* **34**: 795-809.
123. Foster, AC, and Fagg, GE (1984). Acidic amino acid binding sites in mammalian neuronal membranes: their characteristics and relationship to synaptic receptors. *Brain Res* **319**: 103-164.
124. Coffin, JM (2013). Virions at the gates: receptors and the host-virus arms race. *PLoS Biol* **11**: e1001574.
125. Garnacho, C, Serrano, D, and Muro, S (2012). A fibrinogen-derived peptide provides intercellular adhesion molecule-1-specific targeting and intraendothelial transport of polymer nanocarriers in human cell cultures and mice. *J Pharmacol Exp Ther* **340**: 638-647.
126. Baiu, DC, *et al.* (1999). Modulation of the humoral immune response by antibody-mediated antigen targeting to complement receptors and Fc receptors. *J Immunol* **162**: 3125-3130.
127. Dempsey, PW, Allison, ME, Akkaraju, S, Goodnow, CC, and Fearon, DT (1996). C3d of complement as a molecular adjuvant: bridging innate and acquired immunity. *Science* **271**: 348-350.
128. Grubb, JH, Vogler, C, and Sly, WS (2010). New strategies for enzyme replacement therapy for lysosomal storage diseases. *Rejuvenation Res* **13**: 229-236.

129. Maga, JA, *et al.* (2013). Glycosylation-independent lysosomal targeting of acid alpha-glucosidase enhances muscle glycogen clearance in pompe mice. *J Biol Chem* **288**: 1428-1438.
130. Meng, Y, *et al.* (2014). Effective intravenous therapy for neurodegenerative disease with a therapeutic enzyme and a Peptide that mediates delivery to the brain. *Mol Ther* **22**: 547-553.
131. Kitchens, KM, El-Sayed, ME, and Ghandehari, H (2005). Transepithelial and endothelial transport of poly (amidoamine) dendrimers. *Adv Drug Deliv Rev* **57**: 2163-2176.
132. Pardridge, WM (2010). Biopharmaceutical drug targeting to the brain. *J Drug Target* **18**: 157-167.
133. Park, K, Kwon, IC, and Park, K (2011). Oral protein delivery: Current status and future prospect *Reactive and Functional Polymers* **71**: 280-287.
134. Li, S, and Huang, L (2000). Nonviral gene therapy: promises and challenges. *Gene Ther* **7**: 31-34.
135. Muratovska, A, Lightowlers, RN, Taylor, RW, Wilce, JA, and Murphy, MP (2001). Targeting large molecules to mitochondria. *Adv Drug Deliv Rev* **49**: 189-198.
136. Boado, RJ, Hui, EK, Lu, JZ, Zhou, QH, and Pardridge, WM (2011). Reversal of lysosomal storage in brain of adult MPS-I mice with intravenous Trojan horse-iduronidase fusion protein. *Mol Pharm* **8**: 1342-1350.
137. Boado, RJ, Zhang, Y, Xia, CF, Wang, Y, and Pardridge, WM (2008). Genetic engineering of a lysosomal enzyme fusion protein for targeted delivery across the human blood-brain barrier. *Biotechnol Bioeng* **99**: 475-484.
138. Wang, D, *et al.* (2013). Engineering a lysosomal enzyme with a derivative of receptor-binding domain of apoE enables delivery across the blood-brain barrier. *Proc Natl Acad Sci U S A* **110**: 2999-3004.
139. Marlin, SD, and Springer, TA (1987). Purified intercellular adhesion molecule-1 (ICAM-1) is a ligand for lymphocyte function-associated antigen 1 (LFA-1). *Cell* **51**: 813-819.
140. Lu, Z, and Xu, S (2006). ERK1/2 MAP kinases in cell survival and apoptosis. *IUBMB Life* **58**: 621-631.
141. Chen, YC, Lu, PH, Hsu, JL, Yu, CC, and Guh, JH (2011). ICAM-1 and AMPK regulate cell detachment and apoptosis by N-methyl-N'-nitro-N-nitrosoguanidine, a widely spread environmental chemical, in human hormone-refractory prostate cancers. *Toxicol Appl Pharmacol* **257**: 412-419.
142. Paulis, LE, *et al.* (2012). Targeting of ICAM-1 on vascular endothelium under static and shear stress conditions using a liposomal Gd-based MRI contrast agent. *J Nanobiotechnology* **10**: 25.
143. Liu, J, *et al.* (2012). Endothelial adhesion of targeted microbubbles in both small and great vessels using ultrasound radiation force. *Mol Imaging* **11**: 58-66.
144. Hua, S (2013). Targeting sites of inflammation: intercellular adhesion molecule-1 as a target for novel inflammatory therapies. *Front Pharmacol* **4**: 127.

145. Hua, S, and Cabot, PJ (2013). Targeted nanoparticles that mimic immune cells in pain control inducing analgesic and anti-inflammatory actions: a potential novel treatment of acute and chronic pain condition. *Pain Physician* **16**: E199-216.
146. Sakhalkar, HS, *et al.* (2003). Leukocyte-inspired biodegradable particles that selectively and avidly adhere to inflamed endothelium in vitro and in vivo. *Proc Natl Acad Sci U S A* **100**: 15895-15900.
147. Villanueva, FS, *et al.* (1998). Microbubbles targeted to intercellular adhesion molecule-1 bind to activated coronary artery endothelial cells. *Circulation* **98**: 1-5.
148. Kiessling, F, Fokong, S, Koczera, P, Lederle, W, and Lammers, T (2012). Ultrasound microbubbles for molecular diagnosis, therapy, and theranostics. *J Nucl Med* **53**: 345-348.
149. Haverslag, R, Pasterkamp, G, and Hoefer, IE (2008). Targeting adhesion molecules in cardiovascular disorders. *Cardiovasc Hematol Disord Drug Targets* **8**: 252-260.
150. Park, S, *et al.* (2013). Tumor suppression via paclitaxel-loaded drug carriers that target inflammation marker upregulated in tumor vasculature and macrophages. *Biomaterials* **34**: 598-605.
151. Morral-Ruiz, G, Melgar-Lesmes, P, Solans, C, and Garcia-Celma, MJ (2013). Multifunctional polyurethane-urea nanoparticles to target and arrest inflamed vascular environment: a potential tool for cancer therapy and diagnosis. *J Control Release* **171**: 163-171.
152. Mane, V, and Muro, S (2012). Biodistribution and endocytosis of ICAM-1-targeting antibodies versus nanocarriers in the gastrointestinal tract in mice. *Int J Nanomedicine* **7**: 4223-4237.
153. Kaser, A, and Tilg, H (2008). Novel therapeutic targets in the treatment of IBD. *Expert Opin Ther Targets* **12**: 553-563.
154. Anselmo, AC, *et al.* (2013). Delivering nanoparticles to lungs while avoiding liver and spleen through adsorption on red blood cells. *ACS Nano* **7**: 11129-11137.
155. Muzykantov, VR (2001). Delivery of antioxidant enzyme proteins to the lung. *Antioxid Redox Signal* **3**: 39-62.
156. Lavigne, P, Benderdour, M, Shi, Q, Lajeunesse, D, and Fernandes, JC (2005). Involvement of ICAM-1 in bone metabolism: a potential target in the treatment of bone diseases? *Expert Opin Biol Ther* **5**: 313-320.
157. Muro, S, Gajewski, C, Koval, M, and Muzykantov, VR (2005). ICAM-1 recycling in endothelial cells: a novel pathway for sustained intracellular delivery and prolonged effects of drugs. *Blood* **105**: 650-658.
158. Muro, S, *et al.* (2008). Control of endothelial targeting and intracellular delivery of therapeutic enzymes by modulating the size and shape of ICAM-1-targeted carriers. *Mol Ther* **16**: 1450-1458.
159. Charoenphol, P, Mocherla, S, Bouis, D, Namdee, K, Pinsky, DJ, and Eniola-Adefeso, O (2011). Targeting therapeutics to the vascular wall in atherosclerosis--carrier size matters. *Atherosclerosis* **217**: 364-370.
160. Papademetriou, IT, Garnacho, C, Schuchman, EH, and Muro, S (2013). In vivo performance of polymer nanocarriers dually-targeted to epitopes of the same or different receptors. *Biomaterials* **34**: 3459-3466.

161. Ansar, M, Serrano, D, Papademetriou, I, Bhowmick, TK, and Muro, S (2013). Biological functionalization of drug delivery carriers to bypass size restrictions of receptor-mediated endocytosis independently from receptor targeting. *ACS Nano* **7**: 10597-10611.
162. Papademetriou, J, Garnacho, C, Serrano, D, Bhowmick, T, Schuchman, EH, and Muro, S (2013). Comparative binding, endocytosis, and biodistribution of antibodies and antibody-coated carriers for targeted delivery of lysosomal enzymes to ICAM-1 versus transferrin receptor. *J Inherit Metab Dis* **36**: 467-477.
163. Jevnikar, AM, *et al.* (1990). Differing regulation and function of ICAM-1 and class II antigens on renal tubular cells. *Kidney Int* **38**: 417-425.
164. Gimenez-Cassina, A, Lim, F, and Diaz-Nido, J (2006). Differentiation of a human neuroblastoma into neuron-like cells increases their susceptibility to transduction by herpesviral vectors. *J Neurosci Res* **84**: 755-767.
165. Palomo, GM, Cerrato, T, Gargini, R, and Diaz-Nido, J (2011). Silencing of frataxin gene expression triggers p53-dependent apoptosis in human neuron-like cells. *Hum Mol Genet* **20**: 2807-2822.
166. Muro, S, Cui, X, Gajewski, C, Murciano, J-C, Muzykantov, VR, and Koval, M (2003). Slow intracellular trafficking of catalase nanoparticles targeted to ICAM-1 protects endothelial cells from oxidative stress. *Am J Physiol, Cell Physiol* **285**: C1339-1347.
167. Hatherell, K, Couraud, PO, Romero, IA, Weksler, B, and Pilkington, GJ (2011). Development of a three-dimensional, all-human in vitro model of the blood-brain barrier using mono-, co-, and tri-cultivation Transwell models. *J Neurosci Methods* **199**: 223-229.
168. Tretiach, M, van Driel, D, and Gillies, MC (2003). Transendothelial electrical resistance of bovine retinal capillary endothelial cells is influenced by cell growth patterns: an ultrastructural study. *Clin Experiment Ophthalmol* **31**: 348-353.
169. Hagemans, ML, *et al.* (2010). PAS-positive lymphocyte vacuoles can be used as diagnostic screening test for Pompe disease. *J Inherit Metab Dis* **33**: 133-139.
170. Tabas, I (1999). Secretory sphingomyelinase. *Chem Phys Lipids* **102**: 123-130.
171. Bollinger, CR, Teichgräber, V, and Gulbins, E (2005). Ceramide-enriched membrane domains. *Biochim Biophys Acta* **1746**: 284-294.
172. Holopainen, JM, Angelova, MI, and Kinnunen, PK (2000). Vectorial budding of vesicles by asymmetrical enzymatic formation of ceramide in giant liposomes. *Biophys J* **78**: 830-838.
173. Holopainen, JM, Subramanian, M, and Kinnunen, PK (1998). Sphingomyelinase induces lipid microdomain formation in a fluid phosphatidylcholine/sphingomyelin membrane. *Biochemistry* **37**: 17562-17570.
174. Serrano, D, Bhowmick, T, Chadha, R, Garnacho, C, and Muro, S (2012). Intercellular adhesion molecule 1 engagement modulates sphingomyelinase and ceramide, supporting uptake of drug carriers by the vascular endothelium. *Arterioscler Thromb Vasc Biol* **32**: 1178-1185.

175. Gartner, S, Conzelmann, E, and Sandhoff, K (1983). Activator protein for the degradation of globotriaosylceramide by human alpha-galactosidase. *J Biol Chem* **258**: 12378-12385.
176. Conner, SD, and Schmid, SL (2003). Regulated portals of entry into the cell. *Nature* **422**: 37-44.
177. Muro, S, Koval, M, and Muzykantov, V (2004). Endothelial endocytic pathways: gates for vascular drug delivery. *Curr Vasc Pharmacol* **2**: 281-299.
178. Stevens, T, Garcia, JG, Shasby, DM, Bhattacharya, J, and Malik, AB (2000). Mechanisms regulating endothelial cell barrier function. *Am J Physiol Lung Cell Mol Physiol* **279**: L419-422.
179. Abbott, NJ, Ronnback, L, and Hansson, E (2006). Astrocyte-endothelial interactions at the blood-brain barrier. *Nat Rev Neurosci* **7**: 41-53.
180. Brambilla, R, Morton, PD, Ashbaugh, JJ, Karmally, S, Lambertsen, KL, and Bethea, JR (2014). Astrocytes play a key role in EAE pathophysiology by orchestrating in the CNS the inflammatory response of resident and peripheral immune cells and by suppressing remyelination. *Glia* **62**: 452-467.
181. Liu, S, Agalliu, D, Yu, C, and Fisher, M (2012). The role of pericytes in blood-brain barrier function and stroke. *Curr Pharm Des* **18**: 3653-3662.
182. Yang, WW, *et al.* (2007). Intraparenchymal injections of acid sphingomyelinase results in regional correction of lysosomal storage pathology in the Niemann-Pick A mouse. *Exp Neurol* **207**: 258-266.
183. Dodge, JC, *et al.* (2009). Intracerebroventricular infusion of acid sphingomyelinase corrects CNS manifestations in a mouse model of Niemann-Pick A disease. *Exp Neurol* **215**: 349-357.
184. Bae, JS, Carter, JE, and Jin, HK (2010). Adipose tissue-derived stem cells rescue Purkinje neurons and alleviate inflammatory responses in Niemann-Pick disease type C mice. *Cell Tissue Res* **340**: 357-369.
185. Lee, JM, Bae, JS, and Jin, HK (2010). Intracerebellar transplantation of neural stem cells into mice with neurodegeneration improves neuronal networks with functional synaptic transmission. *J Vet Med Sci* **72**: 999-1009.
186. de Lange, EC (2012). The physiological characteristics and transcytosis mechanisms of the blood-brain barrier (BBB). *Curr Pharm Biotechnol* **13**: 2319-2327.
187. Pardridge, WM (2007). Blood-brain barrier delivery. *Drug Discov Today* **12**: 54-61.
188. Fabry, Z, *et al.* (1992). Adhesion molecules on murine brain microvascular endothelial cells: expression and regulation of ICAM-1 and Lgp 55. *J Neuroimmunol* **36**: 1-11.
189. Dietrich, J, *et al.* (2002). Ligand-induced TCR down-regulation is not dependent on constitutive TCR cycling. *J Immunol* **168**: 5434-5440.
190. Shrikant, P, Chung, IY, Ballestas, ME, and Benveniste, EN (1994). Regulation of intercellular adhesion molecule-1 gene expression by tumor necrosis factor-alpha, interleukin-1 beta, and interferon-gamma in astrocytes. *J Neuroimmunol* **51**: 209-220.
191. Hurtado-Alvarado, G, Cabanas-Morales, AM, and Gomez-Gonzalez, B (2014). Pericytes: brain-immune interface modulators. *Front Integr Neurosci* **7**: 80.

192. Stan, RV (2006). Endocytosis pathways in endothelium: how many? *Am J Physiol Lung Cell Mol Physiol* **290**: L806-808.
193. Banks, WA (2009). Blood-brain barrier as a regulatory interface. *Forum Nutr* **63**: 102-110.
194. Megias, L, *et al.* (2000). Endocytosis and transcytosis in growing astrocytes in primary culture. Possible implications in neural development. *Int J Dev Biol* **44**: 209-221.
195. Sokolowski, JD, and Mandell, JW (2011). Phagocytic clearance in neurodegeneration. *Am J Pathol* **178**: 1416-1428.
196. Birdsall, HH (1991). Induction of ICAM-1 on human neural cells and mechanisms of neutrophil-mediated injury. *Am J Pathol* **139**: 1341-1350.
197. Miklossy, J, Doudet, DD, Schwab, C, Yu, S, McGeer, EG, and McGeer, PL (2006). Role of ICAM-1 in persisting inflammation in Parkinson disease and MPTP monkeys. *Exp Neurol* **197**: 275-283.
198. Nie, Z, Nelson, CS, Jacoby, DB, and Fryer, AD (2007). Expression and regulation of intercellular adhesion molecule-1 on airway parasympathetic nerves. *J Allergy Clin Immunol* **119**: 1415-1422.
199. Blanpied, TA, Scott, DB, and Ehlers, MD (2002). Dynamics and regulation of clathrin coats at specialized endocytic zones of dendrites and spines. *Neuron* **36**: 435-449.
200. Royle, SJ, and Lagnado, L (2003). Endocytosis at the synaptic terminal. *J Physiol* **553**: 345-355.
201. Oliveira, H, Pires, LR, Fernandez, R, Martins, MC, Simoes, S, and Pego, AP (2010). Chitosan-based gene delivery vectors targeted to the peripheral nervous system. *J Biomed Mater Res A* **95**: 801-810.
202. Schuchman, EH, Desnick R.J. (2000). Niemann-Pick Disease Types A and B: Acid Sphingomyelinase Deficiencies. In: Scriver, C, Beaudet, A., Sly, W., Valle, D., Childs, B., Kinzler, K., Vogelstein, B. (ed). *XVI Chapter, Lysosomal Disorders The Metabolic and Molecular Bases of Inherited Disease*. McGraw-Hill: 8th edition.
203. Muro, S, *et al.* (2006). Endothelial targeting of high-affinity multivalent polymer nanocarriers directed to intercellular adhesion molecule 1. *J Pharmacol Exp Ther* **317**: 1161-1169.
204. Matsumura, Y, and Maeda, H (1986). A new concept for macromolecular therapeutics in cancer chemotherapy: mechanism of tumoritropic accumulation of proteins and the antitumor agent smancs. *Cancer Res* **46**: 6387-6392.
205. Brooks, DA (1999). Immune response to enzyme replacement therapy in lysosomal storage disorder patients and animal models. *Mol Genet Metab* **68**: 268-275.
206. Gehr, P, Bachofen, M, and Weibel, ER (1978). The normal human lung: ultrastructure and morphometric estimation of diffusion capacity. *Respir Physiol* **32**: 121-140.
207. Higenbottam, TW, and Laude, EA (1998). Endothelial dysfunction providing the basis for the treatment of pulmonary hypertension: Giles F. Filley lecture. *Chest* **114**: 72S-79S.

208. Jaffe, EA (1987). Cell biology of endothelial cells. *Hum Pathol* **18**: 234-239.
209. Lacan, G, *et al.* (2008). Cyclosporine, a P-glycoprotein modulator, increases [18F]MPPF uptake in rat brain and peripheral tissues: microPET and ex vivo studies. *Eur J Nucl Med Mol Imaging* **35**: 2256-2266.
210. Zhao, R, and Pollack, GM (2009). Regional differences in capillary density, perfusion rate, and P-glycoprotein activity: a quantitative analysis of regional drug exposure in the brain. *Biochem Pharmacol* **78**: 1052-1059.
211. Walterfang, M, Abel, LA, Desmond, P, Fahey, MC, Bowman, EA, and Velakoulis, D (2013). Cerebellar volume correlates with saccadic gain and ataxia in adult Niemann-Pick type C. *Mol Genet Metab* **108**: 85-89.
212. Di Rocco, M, Buzzi, D, and Taro, M (2007). Glycogen storage disease type II: clinical overview. *Acta Myol* **26**: 42-44.
213. Martin, JJ, Philippart, M, Van Hauwaert, J, Callahan, JW, and Deberdt, R (1972). Niemann-Pick disease (Crocker's group A). Late onset and pigmentary degeneration resembling Hallervorden-Spatz syndrome. *Arch Neurol* **27**: 45-51.
214. Filosto, M, *et al.* (2014). Non-muscle involvement in late-onset glycogenosis II. *Acta Myol* **32**: 91-94.
215. Rossin, R, Muro, S, Welch, MJ, Muzykantov, VR, and Schuster, DP (2008). In vivo imaging of ⁶⁴Cu-labeled polymer nanoparticles targeted to the lung endothelium. *J Nucl Med* **49**: 103-111.
216. Gary-Bobo, M, Nirde, P, Jeanjean, A, Morere, A, and Garcia, M (2007). Mannose 6-phosphate receptor targeting and its applications in human diseases. *Curr Med Chem* **14**: 2945-2953.
217. Neufeld, EF (1980). The uptake of enzymes into lysosomes: an overview. *Birth Defects Orig Artic Ser* **16**: 77-84.
218. Saul, JM, Annapragada, AV, and Bellamkonda, RV (2006). A dual-ligand approach for enhancing targeting selectivity of therapeutic nanocarriers. *J Control Release* **114**: 277-287.
219. Ohshima, T, *et al.* (1997). alpha-Galactosidase A deficient mice: a model of Fabry disease. *Proc Natl Acad Sci U S A* **94**: 2540-2544.

Publications

As a result of this dissertation, the following works were published or are in preparation for publication.

Peer-Reviewed Articles

1. **Hsu J**, Muro S. (2014) Targeting, endocytosis and lysosomal delivery of active enzymes to the cell body and processes of model human neurons by ICAM-1-targeted nanocarriers. (In preparation)
2. Papademetrou IT, Tsinas Z, **Hsu J**, Muro S. (2014) Combination-targeting to multiple endothelial cell adhesion molecules modulates binding, endocytosis, and in vivo biodistribution of drug nanocarriers and their therapeutic cargoes. (Submitted, under review by JCR)
3. **Hsu J**, Rappaport J, Muro S. (2014) Interaction of ICAM-1-targeted polymer nanocarriers with cells of the BBB. Pharm Res. Epub date: 2014 Feb 21. PMID: 24558007. (In Press)
4. **Hsu J**, Bhowmick T, Burks SR, Kao JPY, Muro S. (2014) Enhancing Biodistribution of Therapeutic Enzymes In Vivo by Modulating Surface Coating and Concentration of ICAM-1-Targeted Nanocarriers. J Biomed Nanotechnol. 2014 Feb 1;10(2):345-54. PMID: 24738342.

5. **Hsu J**, Northrup L, Bhowmick T, Muro S. (2012) Enhanced delivery of α -glucosidase for Pompe disease by ICAM-1-targeted nanocarriers: comparative performance of a strategy for three distinct lysosomal storage disorders. *Nanomedicine*. 2012 Jul;8(5):731-9. PMID: 21906578. PMCID: PMC3279604.
6. **Hsu J**, Serrano D, Bhowmick T, Kumar K, Shen Y, Kuo YC, Garnacho C, Muro S. (2011) Enhanced endothelial delivery and biochemical effects of α -galactosidase by ICAM-1-targeted Nanocarriers for Fabry Disease. *J Control Release*. 2011 Feb 10;149(3):323-31. PMID: 21047542. PMCID: PMC3073729.

Book Chapter

7. **Hsu J**, Muro S. (2011) Nanomedicine and drug delivery strategies for treatment of genetic diseases. In: Plaseska-Karanfilska D, ed. *Genetic Disease*. InTech, Chapter 14 and pages 240-66. 2011 Sep 30.